Characterizing the Behavior of Magnetorheological Fluids at High Velocities and High Shear Rates

by

Fernando D. Goncalves

Dissertation submitted to the Faculty of the

Virginia Polytechnic Institute and State University

in partial fulfillment of the requirements for the degree of

Doctor of Philosophy

in

Mechanical Engineering

Approved:

Dr. Mehdi Ahmadian	Dr. Donald Baird
Dr. David Carlson	Dr. Daniel Inman
Dr. Mary Kasarda	Dr. Donald Leo

January 2005

Blacksburg, Virginia

Keywords: Magnetorheological, MR Fluid, MR Effect, Yield Stress, Bingham, Response Time, Dwell Time, Shear Rate, High Velocity

Characterizing the Behavior of Magnetorheological Fluids at High Velocities and High Shear Rates

by

Fernando D. Goncalves

Abstract

Magnetorheological (MR) fluids offer solutions to many engineering challenges. The success of MR fluid is apparent in many disciplines, ranging from the automotive and civil engineering communities to the biomedical engineering community. This well documented success of MR fluids continues to motivate current and future applications of MR fluid.

One such application that has been considered recently is MR fluid devices for use in impact and other high velocity applications. In such applications, the fluid environment within the device may be well beyond the scope of our understanding for these fluids. To date, little has been done to explore the suitability of MR fluids in such high velocity and high shear applications.

While future applications may expose the fluid to adverse flow conditions, we must also consider current and existing applications which expose the fluid to extreme flow environments. Consider, for example, an MR damper intended for automotive primary suspensions, in which shear rates may exceed 10^5 s^{-1}. Flow conditions within these dampers far exceed existing fluid behavior characterization.

The aim of the current study is to identify the behavior of the fluid under these extreme operating conditions. Specifically, this study intends to identify the behavior of MR fluid subject to high rates of shear and high flow velocities. A high shear rheometer is built which allows for the high velocity testing of MR fluids. The rheometer is capable of fluid velocities ranging from 1 m/s to 37 m/s, with corresponding shear rates ranging from 0.14×10^5 s^{-1} to 2.5×10^5 s^{-1}. Fluid behavior is characterized in both the off-state and the on-state.

The off-state testing was conducted in order to identify the high shear viscosity of the fluid. Because the high shear behavior of MR fluid is largely governed by the behavior of the carrier fluid, the carrier fluid behavior was also identified at high shear. Experiments were conducted using the high shear rheometer and the MR fluid was shown to exhibit nearly Newtonian post-yield behavior. A slight thickening was observed for growing shear rates. This slight thickening can be attributed to the behavior of the carrier fluid, which exhibited considerable thickening at high shear.

The purpose of the on-state testing was to characterize the MR effect at high flow velocities. As such, the MR fluid was run through the rheometer at various flow velocities and a number of magnetic field strengths. The term “dwell time” is introduced and defined as the amount of time the fluid spends in the presence of a magnetic field. Two active valve lengths were considered, which when coupled to the fluid velocities,

generated dwell times ranging from 12 ms to 0.18 ms. The yield stress was found from the experimental measurements and the results indicate that the magnitude of the yield stress is sensitive to fluid dwell time. As fluid dwell times decrease, the yield stress developed in the fluid decreases. The results from the on-state testing clearly demonstrate a need to consider fluid dwell times in high velocity applications. Should the dwell time fall below the response time of the fluid, the yield stress developed in the fluid may only achieve a fraction of the expected value. These results imply that high velocity applications may be subject to diminished controllability for falling dwell times.

Results from this study may serve to aid in the design of MR fluid devices intended for high velocity applications. Furthermore, the identified behavior may lead to further developments in MR fluid technology. In particular, the identified behavior may be used to develop or identify an MR fluid well suited for high velocity and high shear applications.

“I can do all things through Christ who strengthens me.”

Philippians 4:13

Acknowledgements

I wish to thank my advisor Dr. Mehdi Ahmadian, who, over the course of my time at Virginia Tech, has been a great source of encouragement. Dr. Ahmadian has served as advisor and friend, and his support is truly appreciated. I also wish to thank the members of my Ph.D. committee for their guidance and support throughout this particular effort and, more generally, for their council during my time at Virginia Tech. Specifically, I would like to offer thanks to Dr. Daniel Inman, Dr. Donald Leo, Dr. Mary Kasarda, Dr. Donald Baird, and Dr. David Carlson. Special thanks are due to Dr. David Carlson, from Lord Corporation for agreeing to serve on my committee. Dr. Carlson has been a great resource and his involvement in my research is greatly appreciated. I would also like to thank Dr. Lynn Yanyo at Lord Corporation for her valuable feedback. Thanks are also due to Lord Corporation for their generous contribution to the Advanced Vehicle Dynamics Laboratory. For financial support during my time at Virginia Tech I am grateful to the Department of Mechanical Engineering.

I would also like to thank Dr. Baird in the Chemical Engineering Department for allowing the use of the equipment in the Polymer Processing Lab. Special thanks are due to his students, Matt Wilding and Chris Seay, for their assistance in making measurements on the fluid. This work has also been aided by the hard work of a number of individuals in the machine shop in the Department of Mechanical Engineering. Specifically, I would like to thank Billy Songer, James Dowdy, Timmy Kessinger, and Johnny Cox for their hard work and patience. Their guidance and effort has been a great contribution to this work and does not go unnoticed. I would also like to recognize the efforts of Bob Simonds in the Engineering Science and Mechanics Department. I am grateful to Mr. Simonds for helping me with all things related to MTS.

I would like to thank Dr. Jeong-Hoi Koo, colleague and great friend, for his constant support and encouragement. I am indebted to Jeong-Hoi for his valuable assistance on a countless number of occasions. I would also like to thank Dr. Nathan Siegel who provided valuable insight into my work for which I am truly grateful. I would also like to thank all the members of AVDL, past and present, for their companionship and memories. I also wish to list a group of friends whose companionship has meant a lot to me during my time at Virginia Tech. This list includes Jeong-Hoi Koo, Nathan Siegel, Michael Seigler, Emmanuel Blanchard, Mohammad Elahinia, and others. Thank you!

I would like to express my deepest gratitude to my parents, Manuel and Joana Goncalves, who've given more than I could ever hope to repay. For their love, support, and sacrifice I am forever grateful. To my brother Manny, I would like to express thanks for always looking after me. True to the big brother role, Manny has always been concerned with my well being, and for this I am grateful.

In words it would be difficult for me to express my gratitude to my fiancée, Courtney Mulligan. Her support, encouragement, and understand over the years is overwhelming. I look forward to expressing my gratitude in our coming future.

Finally, I would like to thank the Lord for being by my side always. I earn strength through my faith in God and his faith in me.

Contents

List of Tables

List of Figures

1 Introduction

The purpose of this chapter is to express the motivation for this work and to introduce the objectives. With the objectives identified, the means by which the objectives will be met are discussed. Finally, a discussion of the contributions of this work and an outline of this document conclude the chapter.

1.1 Motivation

Magnetorheological (MR) fluids offer solutions to many engineering challenges. The success of MR fluid is apparent in many disciplines, ranging from the automotive and civil engineering communities to the biomedical engineering community. There have been a countless number of studies which identify the benefits of using MR devices in these and other fields. This well documented success of MR fluids continues to motivate current and future applications of MR fluid.

Much of the success of MR fluid devices is largely due to advancements in fluid technology. Today's MR fluids are capable of achieving yield stresses in excess of 80 kPa which indicates an impressive range of fluid controllability and dynamic range. The fluids have also exhibited improved stability behavior. Moreover, the durability and life of the fluid have developed such that the fluid can be considered for commercial implementation. The performance of today's MR fluids is the result of a great number of studies which identify the properties and behavior of MR fluids. The literature is well populated with works related to the behavior of MR fluid or the performance of specific MR fluid devices. In many cases, knowledge of the performance of the MR device precedes a thorough understanding of the behavior of the fluid operating in such a device. This is the case for many MR fluid devices. An MR device intended for one application often finds use in an alternate application in which the operating conditions of the fluid differ greatly from the original application. An example of this "borrowed" technology is the many applications of Lord Corporation's MotionMaster™ damper. This damper, originally intended for seat suspensions in trucks and buses, has also been considered for service in civil engineering applications and in prosthetic limbs. In each of these applications, the operating conditions of the fluid vary considerably. Perhaps a more

extreme example would be the use of MR automotive dampers (intended for vehicle primary suspensions) in impact or shock loading applications. Here again, the conditions inside the damper vary considerably.

While fluid behavior may be well understood under certain operating conditions, there is a great need to understand fluid behavior in all regimes of operation. Fluid behavior is often characterized in a laboratory in which fluid conditions are moderate, at best, and are not representative of the conditions within many existing MR fluid devices. In many current applications of MR fluids, fluid conditions within the device are far beyond any published behavior characterization. In order to support existing applications, and encourage emerging applications, there is a need to identify MR fluid behavior under conditions that are representative of those observed in current and future devices. Specifically, there is a need to understand the behavior of MR fluids at high shear rates and high flow velocities.

1.2 Objectives

This research intends to address the lack of awareness regarding MR fluid behavior under adverse flow conditions. The hope here is to provide a thorough investigation of the behavior of MR fluid operating in conditions that are in the range of those observed in current devices.

The primary objectives of this research can be summarized as follows:

1. Better understand the rheological behavior of MR fluids at high shear rates and high velocities
2. Improve existing models for MR fluids such that they can accurately represent the fluid behavior at high shear rates
3. Verify, to the extent possible, the accuracy of the proposed models through comparison with experimental results
4. Potentially provide engineering guides that can be used for designing MR fluids for high shear rate applications

1.3 Approach

With the primary objective of this work identified as characterizing the behavior of MR fluids at high shear rates and high velocities, a means for testing the fluid under such conditions was necessary. To this end, a slit-flow rheometer was designed and built which allowed for the high velocity testing of MR fluid. Similar to a conventional capillary rheometer, the slit-flow rheometer is capable of generating fluid velocities many times greater than the piston velocity. A series of experiments were conducted with the fluid in an unenergized state and at various magnetic field strengths. Results of these experiments are used to identify fluid behavior at high shear rates and high flow velocities. Specifically, for the zero-field tests, the fluid viscosity is found at high rates of shear. For the magnetic field testing, the yield stress developed in the fluid is found to quantify the MR effect at high flow velocities.

The behavior observed in the experiments is compared to the behavior predicted by existing models. Departures between the model and the experiment are identified. Improvements to existing models are proposed which account for the behavior observed at high velocities.

1.4 Contributions

This research has identified the behavior of MR fluid in, as yet, uncharacterized flow conditions. The high shear behavior of the fluid was identified in both the off-state and the on-state. Under such conditions, the behavior of the fluid has been shown to depart from commonly accepted behavior of the fluid. The current study may serve as a platform for future studies in the high velocity behavior of MR fluid, and has identified practical considerations for MR devices intended for high velocity and high shear applications.

Specific contributions can be summarized as follows:

- The off-state behavior of the MR fluid has been identified at shear rates as high as $2.5 \times 10^5\ s^{-1}$. Fluid viscosity was identified at these shear rates.
- The behavior of the carrier fluid has been identified at high shear.

- The high velocity behavior of MR fluid in the on-state was evaluated. The MR effect was characterized as a function of fluid dwell time.
- Practical limitations of MR fluids at high velocities have been identified. High velocity applications of MR fluids may be subject to diminished controllability for falling dwell times.
- The outcome of the current study may serve as a foundation for future studies in the high shear and high velocity applications of MR fluid and MR fluid devices.

1.5 Outline

The next chapter, Chapter 2, provides background on MR fluids and MR fluid devices. A general discussion of the fundamental behavior of MR fluids is presented. Chapter 2 also discusses a number of MR fluid devices and their applications. The chapter concludes with an introduction of emerging applications of MR fluids and reiterates the motivation for this work. Chapter 3 reviews common visco-plastic models, often used to describe the field dependent yield stress of MR fluids. A model of quasi-steady parallel flow of MR fluid is developed. Chapter 3 also discusses a model which is used to predict the yield stress for any MR fluid as a function of magnetic field strength. In Chapter 4, the high shear rheometer used in this study is discussed in detail. Furthermore, the experimental approach is introduced. Results for the high shear behavior of the unenergized fluid are presented in Chapter 5. This chapter discusses, in detail, the composition and properties of the MR fluid used in this study. The high shear viscosity is found from experimental measurements. In Chapter 6, the high flow velocity behavior is discussed. In Chapter 6, the MR effect is introduced and experimental results for the fluid under various magnetic field strengths are presented. Chapter 6 also provides a discussion on proposed improvements to existing models. Finally, Chapter 7 provides a summary of the work and highlights the significant results. Recommendations for future work are also presented in Chapter 7.

2 MR Fluids and Devices

Magnetorheological (MR) fluids belong to a class of fluids that exhibit variable yield stress. Discovered by Jacob Rabinow at the US National Bureau of Standards in 1948 [1], MR fluid has the ability to change from a fluid state to a semi-solid or plastic state instantaneously upon the application of a magnetic field. In this semi-solid state, the fluid exhibits viscoplastic behavior that is characterized by the field-dependent yield stress. It is this field-dependent yield stress, and their fast response time, that make MR fluids an attractive technology for many applications.

MR fluid's success has been apparent in many fields of engineering and new applications continue to emerge. While much of the fluid's success has been realized in devices intended for automotive or civil engineering applications, recent studies have investigated the fluid's promise in impact or shock related applications. These emerging applications, and many current applications, subject the fluid to extreme flow conditions. Specifically, these flow environments or conditions include high shear and high velocity flow. The challenge in such devices becomes the lack of information regarding the behavior of MR fluid under these adverse operating conditions.

This chapter will review the fundamental behavior of MR fluids and present some of the existing MR fluid devices. An introduction of some of the emerging applications of MR fluids then follows. The chapter concludes with a discussion of some of the challenges associated with the current and future use of MR fluids in, as yet, uncharacterized flow conditions.

2.1 Magnetorheological fluids

In the absence of a magnetic field, MR fluid is free flowing with a consistency similar to motor oil. The value of these fluids is realized when a magnetic field is applied; micron-sized ferrous particles suspended in the fluid align parallel to the flux path, creating particle chains. Figure 2-1 illustrates this process. Initially, the ferrous particles are in an amorphous state as shown in Figure 2-1a. When a magnetic field is applied, the ferrous particles begin to align along the flux path as shown in Figure 2-1b. Figure 2-1c shows

the ferrous particles aligned along the flux path creating particle chains in the fluid. These particle chains resist and restrict fluid movement. As a result, a yield stress is developed in the fluid. The degree of change is related to the magnetic field strength and may occur in a matter of milliseconds [2, 3].

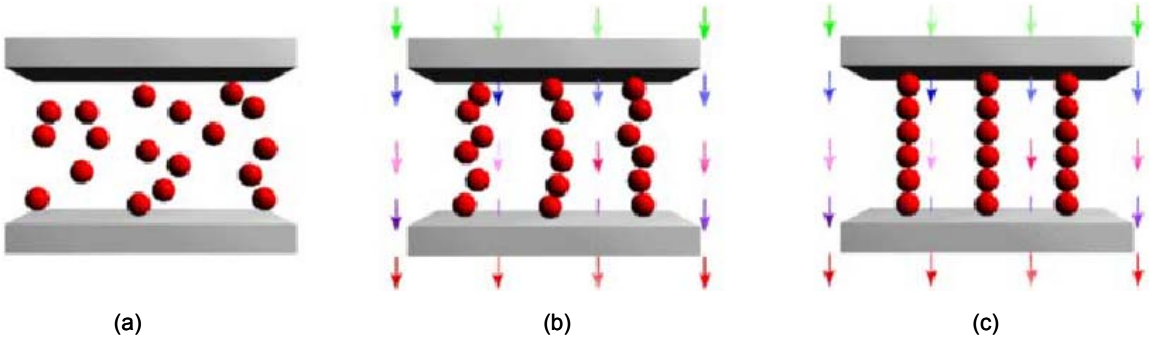

Figure 2-1. Activation of MR fluid: (a) no magnetic field applied; (b) magnetic field applied; (c) ferrous particle chains have formed (© 2005 Lord Corporation [4]. All rights reserved)

2.2 MR fluid devices

The benefit of the controllable yield stress in MR fluids has been realized in many devices for various applications. The range of applications is impressive and indicates the potential for future developments. In many such applications the fluid is employed in one of three common modes (valve mode, shear mode, or squeeze mode). The three modes are shown in Figure 2-2. Both valve and shear mode are commonly used in MR dampers. Other applications of shear mode appear in MR brakes and clutches. In valve mode, the fluid flows between fixed parallel plates. This pressure driven flow is commonly referred to as Poiseuille flow. In shear mode, the fluid flows between parallel plates sliding relative to each other with speed v_o. This type of flow combines Poiseuille flow with shear flow or Couette flow. Squeeze mode, less common than the other two modes, has been considered for small amplitude vibration mitigation [5, 6]. In squeeze mode, it is often assumed that the lateral flow of the fluid has Poiseuille-like behavior.

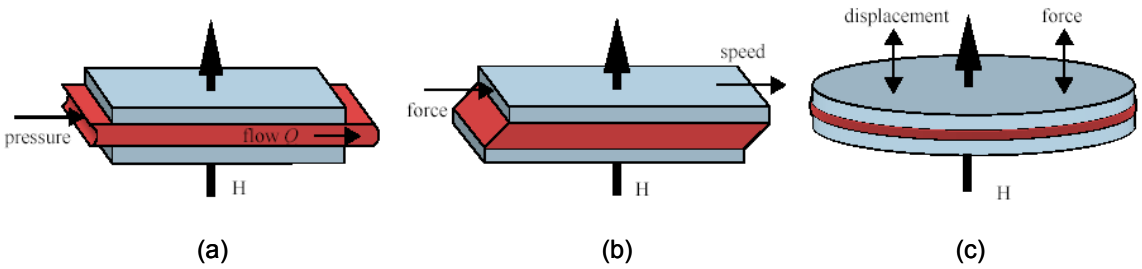

Figure 2-2. MR fluid modes: (a) valve mode; (b) shear mode; (c) squeeze mode (image adapted from [7])

The benefit of the controllable yield stress in MR fluids is often realized in devices such as MR dampers. In both the automotive industry and the civil engineering community, applications of MR dampers have been actively studied because of their ability to respond quickly while providing large dynamic forces. Consider the section view of an MR damper shown in Figure 2-3. Unlike hydraulic dampers, MR dampers do not require mechanical valves to restrict flow. Instead, an electromagnetic coil is incorporated into the piston and the reservoir is filled with MR fluid. With the application of current through the wire leads, a magnetic field is developed in the annular orifice. This magnetic field causes a yield stress to develop in the fluid as it passes the through the flux path, thus increasing the apparent viscosity of the fluid. Because of their ability to offer controllable damping force with minimal power requirements, MR fluid dampers are considered semi-active damping elements. It is in this form that they have served as solutions to many engineering challenges.

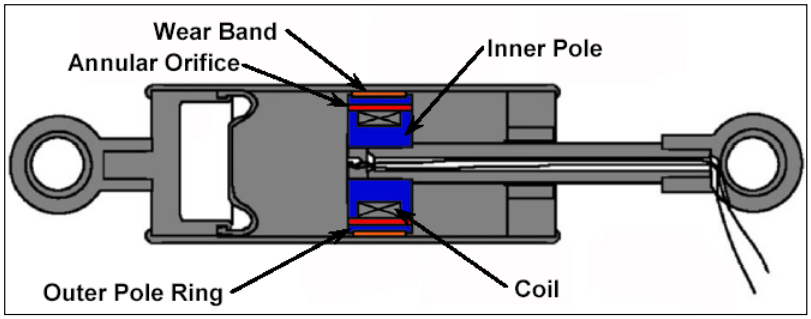

Figure 2-3. Section view of commercial MR fluid damper (image adapted from [8])

The benefit of using an MR fluid damper over a conventional passive damper becomes apparent if we consider the force generated by the damper. Consider the force-velocity illustration in Figure 2-4a. For a simple linear viscous damper, at a given velocity, the damper will generate a force proportional to that velocity. An MR damper is capable of generating a continuously variable force in the range of the off-state to on-state damping force. Figure 2-4b shows an experimentally obtained force-velocity curve for an MR damper designed and built for passenger vehicles. The wide range of controllable forces lends favorably to many real-time control applications.

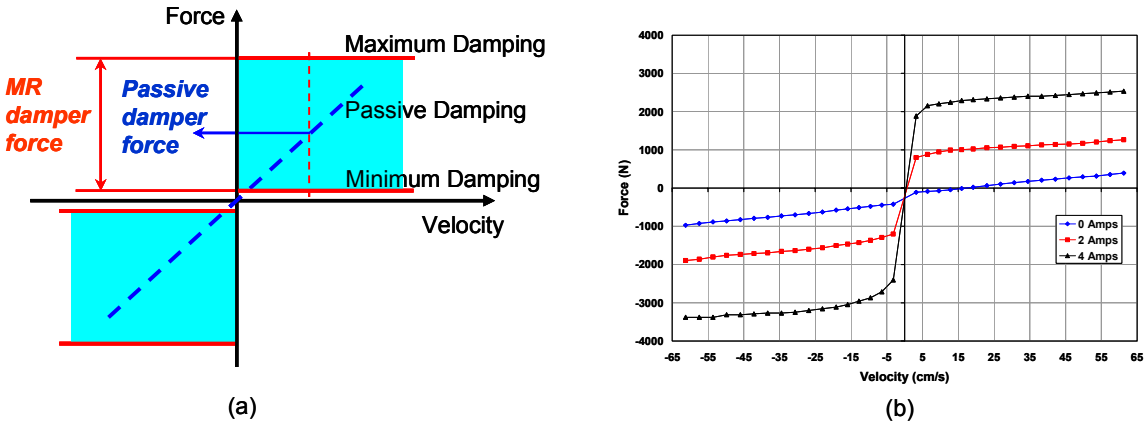

Figure 2-4. (a) Force-velocity illustration (image adapted from [9]); (b) experimentally obtained force-velocity curve

2.2.1 MR devices in automotive applications

The automotive industry in particular has taken advantage of MR fluid dampers as real-time semi-active damping elements. First introduced by Crosby and Karnopp [10, 11], semi-active systems have since been considered for vehicle primary suspensions. Semi-active suspensions have been shown to offer valuable benefits for vehicle primary suspensions [12-14]. Moreover, semi-active suspension systems which use MR fluid dampers have developed into a technology that is currently being implemented. As early as 2002, Cadillac has offered an MR semi-active suspension in its premium vehicles,

such as the Seville STS and Escalade EXT [15, 16]. Currently, Cadillac offers a Magnetic Ride Control suspension on the 2004 STS and the 2004 SRX. Other GM brands are offering similar advanced suspensions. With the release of the 50th anniversary Corvette, Chevrolet offered a Magnetic Selective Ride Control system. The same suspension has carried over into the sixth generation Corvette. Advantages of this suspension include real-time control and the ability of the suspension to adapt to changing road and driving conditions. Figure 2-5 illustrates the performance benefits of the Magnetic Selective Ride Control system. A 60 mph pass over the Ride and Handling Loop at the Milford Proving Grounds demonstrates the superior control of the MR suspension [17].

Figure 2-5. Base C5 Corvette and 50th anniversary Corvette with Magnetic Selective Ride Control suspension (image adapted from [17])

Vehicle secondary suspensions are also good candidates for MR dampers. One of the most commercially successful MR devices to date is the Rheonetic RD-1005-3 MR damper that is manufactured by Lord Corporation [18]. Much of the success attributed to the Rheonetic RD-1005-3 MR damper is its use in semi-active seat suspension systems for large on and off road vehicles [19]. This particular damper is used in a seat suspension system available from Lord Corporation called the MotionMaster™ Ride Management System, which consists of the damper and a control unit as shown in Figure 2-6. This system, which is intended as a retrofit to existing hydraulic truck seat dampers, as well as for use by the original equipment manufacturer, has been very well received by the industry. There have been a number of studies which demonstrate the advantages of a

semi-active damper over conventional passive dampers in secondary or seat suspensions [20-23]. Agricultural off-highway vehicles also stand to benefit from the superior vibration isolation available with the MotionMaster™ system. Sears Seating has partnered with Lord Corporation to develop a MotionMaster™ system tailored for agricultural and off-highway equipment [24]. School transportation officials have also taken advantage of the MotionMaster™ system. In fact, in an effort to reduce worker compensation claims, school transportation officials in many states have adopted the MotionMaster™ Ride Management System for use in buses. When retrofitted with the MotionMaster™ Ride Management System drivers report less fatigue and reduced back and leg discomfort [25].

Figure 2-6. Lord MotionMaster™ Ride Management System (© 2005 Lord Corporation [4]. All rights reserved)

2.2.2 MR devices in structural control applications

MR dampers have also gained considerable attention in structural control applications. Seismic response reduction using MR dampers is an area of research that has received considerable attention recently [26, 27]. Recently, large-scale MR fluid dampers have been considered for structural vibration mitigation. A full-scale MR fluid damper has been designed and built in order to test the suitability of such devices in civil engineering applications [28, 29]. The double-ended design, shown in Figure 2-7, eliminates the need for an accumulator to compensate for piston rod volume. Designed for a maximum force of 200,000 N, the damper is approximately 1 m long with a mass of 250 kg.

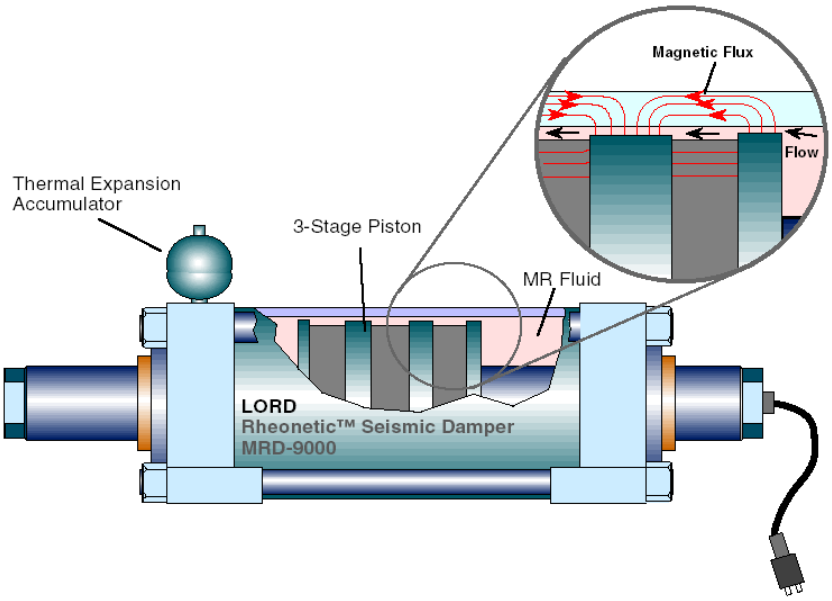

Figure 2-7. Schematic of Lord Corporation's 180 kN seismic damper (© 2005 Lord Corporation [4]. All rights reserved)

Other structures that have benefited from MR damper technology are cable-stayed bridges. The Dongting Bridge is a cable-stayed bridge which crosses Dongting Lake where it meets the Yangtze River in south central China. In June of 2002 the Dongting Bridge became the first cable-stayed bridge to use MR dampers to suppress wind and rain induced vibrations [30-32]. Results indicate significant vibration control effectiveness in the cables that were damped with MR dampers.

MR dampers have also been considered for use in structural tuned vibration absorbers. In such an application, the damper must be able to provide sufficient damping force while still maintaining a low off-state force. The MR sponge damper, shown in Figure 2-8, was a worthy candidate. Koo [9] showed that an MR sponge damper coupled to a tuned vibration absorber (TVA) can provide benefits for controlling unwanted vibrations in structures. The inherent difficulty with TVAs in structures is the inevitable off-tuning of the TVA due to changes in the system's operating conditions, i.e., mass or stiffness changes over time. This off-tuning can lead to degradation in the performance of the TVA. Koo showed that with the addition of an MR damper, the sensitivity of the TVA system to changes in system operating conditions is reduced. In other words, the

MR TVA is more robust to changes in mass or stiffness. Because of its low off-state damping, the MR sponge damper was a good candidate for such an application.

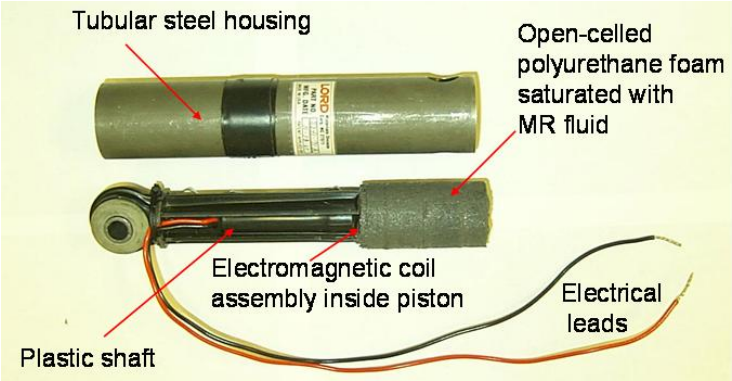

Figure 2-8. Lord Corporation MR sponge damper (© 2005 Lord Corporation [4]. All rights reserved)

The MR sponge damper contains MR fluid in an absorbent matrix such as sponge, open-celled foam, or fabric. The sponge keeps the MR fluid located in the active region of the device where the magnetic field is applied. The device is operated in a direct shear mode with a minimum volume of MR fluid (~3 mL). Moreover, the MR sponge device does not require high-cost components, such as seals, rod surface finish, and the precision mechanical tolerances that are normally associated with conventional fluid-filled MR devices. Cost sensitive applications, such as domestic washing machines, stand to benefit from the MR sponge damper [33]. Figure 2-8 shows the internal components of the MR sponge damper. This MR sponge device is appropriate for many applications in which low off-state damping is desired while still maintaining controllability in the on-state force.

2.2.3 Other MR fluid applications

A rather innovative application of the Lord MotionMaster™ damper is its use in a prosthetic leg that is being developed by Biedermann Motech GmbH [34]. The device, shown in Figure 2-9, dramatically improves the mobility of leg amputees by mimicking a natural gait. Coupled with a combination of sensors and controllers, the device can adapt

to varying movements, ranging from uphill and downhill motion to stairs, and even bicycling [35].

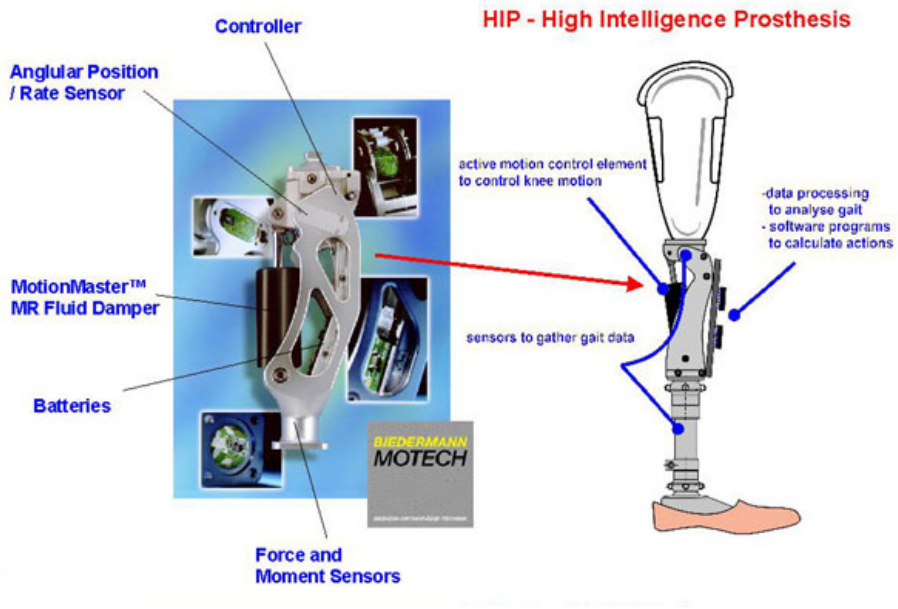

Figure 2-9. Biedermann Motech prosthetic leg (© 2005 Lord Corporation [4]. All rights reserved)

Another commercial use for MR fluids is rotary brakes. Lord Corporation currently manufactures an MR rotary brake, shown in Figure 2-10, which can be used for exercise equipment, pneumatic actuators, steer-by-wire systems, and other similar applications [36]. This device offers high controllability, fast response time (10 to 30 milliseconds), high torque at low speed, and requires very low power. Other benefits of this device include ease of integration, programmable functionality, rugged construction, and long service life [19].

Figure 2-10. Lord Corporation MR rotary brake (© 2005 Lord Corporation [4]. All rights reserved)

One of the most innovative commercial applications for MR fluids is in the polishing of optical lenses. QED Technologies is currently producing a multiple axis CNC polishing machine (Figure 2-11a) that uses a slurry made of MR fluid and an abrasive. The process is illustrated in Figure 2-11b. When the fluid is delivered to the wheel, it is pulled against the wheel by the magnetic field. A yield stress is developed in the fluid and it becomes a subaperture polishing tool. The shape and stiffness of the fluid can be manipulated by real-time control of the magnetic field [37, 38]. This same technology has also been applied to the manufacturing of continuous phase plates for use in laser applications requiring precise manipulation and control of beam-shape, energy distribution, and wavefront profile [39]. The MR finishing techniques make it possible to imprint complex topography onto optical surfaces.

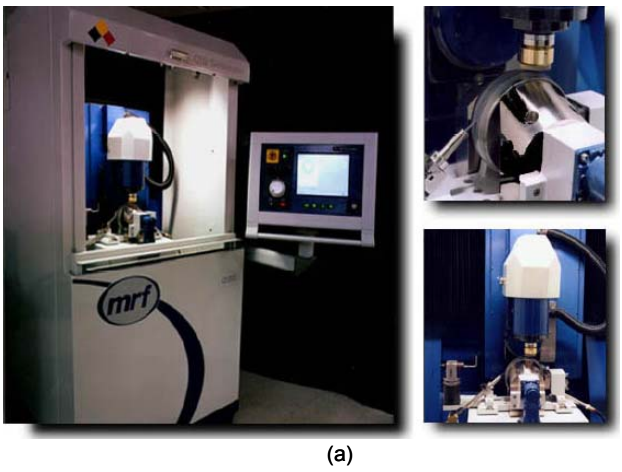

Figure 2-11. (a) QED Technologies' Q22 magnetorheological finishing machine; (b) diagram of polishing process (images adapted from [37])

2.3 MR fluids in high velocity applications

The great success of MR fluids continues to develop into new and emerging applications. Recently, a number of studies have considered the use of MR fluid dampers in impact or shock loading applications. Researchers have taken note of the success of MR dampers in conventional vibration suppression applications and are attempting to extend this success to impact or shock applications.

One such application is the use of MR dampers for active recoil of medium or large caliber gun systems. Consider the work by Ahmadian et al. [40] in which an MR damper was used to control the recoil dynamics of a 50-caliber rifle. An MR damper was mounted on the recoil carriage of the rifle. The authors demonstrate that the MR damper is capable of providing controllability in recoil carriage displacement and velocity. The force transmitted was shown to be highly dependent on magnetic field strength. Several other studies have considered similar applications of MR dampers. Engineers at General Dynamics Armament Systems are investigating the benefits of active recoil control using MR fluid. Such benefits include reduced weight, reduced recoil force, and enhanced accuracy and system stability [41]. The use of MR dampers in recoil systems has been considered elsewhere as well. Many such studies are still under strict publication restrictions and can not be discussed here. However, the results from these studies are promising and have led to the design and development of an MR recoil damper intended for high-speed applications [42, 43].

El Wahed et al. [44, 45] have studied the dynamic performance of MR and ER fluids when subjected to impulsive loads. The ER device used in this study operated in squeeze flow mode. A commercially available MR damper was also tested. A drop tower was used to simulate the impulsive loads. Several drop heights were considered ranging from 6.5 cm to 16.5 cm. For both devices, the force transmitted was shown to increase for increasing field strength. The authors claim that both devices are capable of controlling forces in structural components.

Norris [46] studied the behavior of MR dampers subject to impact and shock loading. Two types of MR dampers (mono-tube, double-ended) were tested in a drop tower with drop heights ranging from 0.305 m (12") to 2.43 m (96"), with corresponding

impact velocities of 2.18 m/s (86 in/s) and 6.60 m/s (260 in/s). Norris claims that the results were dominated by fluid inertia and that the damper performance can be separated into two regions, controllable and uncontrollable. The results for varying field strength were indistinguishable until the piston velocity dropped below a certain value. Once the piston velocity dropped below a certain threshold value, the fluid became controllable.

A recent study by Browne et al. [47] has investigated the promise of MR fluid dampers in another form of impact – vehicular crashes. General Motors R&D Center is currently investigating the suitability of MR fluid based devices for impact energy management systems. The study by Browne et al. focuses on the response of such devices at stroking velocities representative of vehicular crashes. Experiments were performed using a "free-flight" drop tower at impact velocities ranging from 1 m/s to 10 m/s. The results presented by Browne et al. indicate that the response of the MR damper remains tunable over the range of impact velocities considered. However, the authors identify a diminished ability to tune the level of peak force as impact velocities increase.

Choi and Wereley [48] studied the effectiveness of an electrorheological (ER) or MR fluid-based landing gear system for aircraft. Specifically, the authors used an ER damper to investigate the feasibility of such a device to attenuate dynamic loading and vibration due to the landing impact. In characterizing the ER damper, the authors identified a reduction in controllability for growing piston velocities. For the particular ER damper used in the study, the authors state that for piston velocities in excess of 0.2 m/s, the increment of the damping force in response to applied field decreases. The authors speculate that the reduced controllability is due to the fact that the particle chains are easier to break at high flow velocities. Though this paper considered an ER fluid damper for proof of concept, because ER and MR fluids are governed by the same constitutive relation, the results in this study further demonstrate the need to understand fluid behavior at high velocities.

The operating conditions in an MR damper used in impact or shock applications are not exclusive to only impact or shock applications. Consider the conditions found inside a MotionMaster™ damper in normal use where piston velocities are in the range of 5 cm/s – 20 cm/s. Corresponding shear rates range from $1x10^4$ s^{-1} – $4x10^4$ s^{-1}. In extreme

conditions, this damper may experience speeds in excess of 1 m/s generating shear rates as high as $2x10^5$ s^{-1}. Similar conditions are observed for MR dampers used in automotive primary suspensions where shear rates may even reach 10^6 s^{-1} [49]. Recently, the U.S. Army has considered an MR-based suspension for the Army's HMMWV Hummer [50]. With increased mobility over harsh terrain, shear rates can approach even higher levels than those observed in passenger vehicles. Another consideration is in MR rotary brake applications. Under normal operating speeds of 100 – 1000 RPM shear rates range from 10^3 s^{-1} – 10^4 s^{-1} [49].

2.4 Summary

The literature indicates the promise of MR dampers in high velocity applications. In this capacity, however, the performance of the MR fluid itself is widely unknown. Much of this uncertainty stems from the lack of knowledge concerning the behavior of the fluid under high shear and high velocity conditions. Few studies exist in which an accurate identification of fluid behavior at high shear and high velocities is presented.

The abundant success of MR fluid devices has led to wealth of knowledge pertaining to the fluid performance and behavior under certain operating conditions. However, as applications continue to develop, there is a need to better understand MR fluid behavior in regimes that have yet to be quantified. The high shear and high velocity behavior has yet to be explored and yet it has been shown that current and future applications of MR fluids do indeed operate in this regime. As such, a thorough investigation of the performance of the fluid under such conditions is needed.

3 MR Fluid Models

MR fluid models play an important role in the development of MR fluid devices. Moreover, accurate models that can predict the performance of these MR fluid devices are an important part of implementation of such devices. Beginning with the work by Phillips in 1969 [51], ER fluid and MR fluid modeling has received significant attention, and as such, the degree of accuracy available with existing models is quite good.

This chapter will review two behavioral models of MR fluids. The first behavioral model represents the flow behavior of the fluid. Two existing models describing the visco-plastic flow behavior of MR fluids are reviewed. After introducing these models, a quasi-steady model of MR fluid flow through fixed parallel plates will be developed based on the Navier-Stokes equation. The development of this model is used to interpret the experimental results presented in Chapter 5 and Chapter 6. The second behavioral model provides a relationship between the MR fluid yield stress and the strength of the applied magnetic field. This particular model is valuable for estimating the yield stress developed in the fluid at a certain magnetic field strength.

3.1 Visco-plastic models

One model that is often used to describe the field-dependent behavior of MR fluids is the Bingham plastic model. The Bingham constitutive relation can be written as

$$\tau = \pm\tau_o + \mu\dot{\gamma} \quad |\tau| > |\tau_o| \tag{3-1}$$

where τ_o is the yield stress, μ is the viscosity, and $\dot{\gamma}$ is the shear rate. The onset of flow does not occur until the shear stress exceeds the yield stress (i.e., for $\tau < \tau_o \Rightarrow \dot{\gamma} = 0$). Figure 3-1 shows the Bingham plastic model, which is effective in representing the field-dependent behavior of the yield stress.

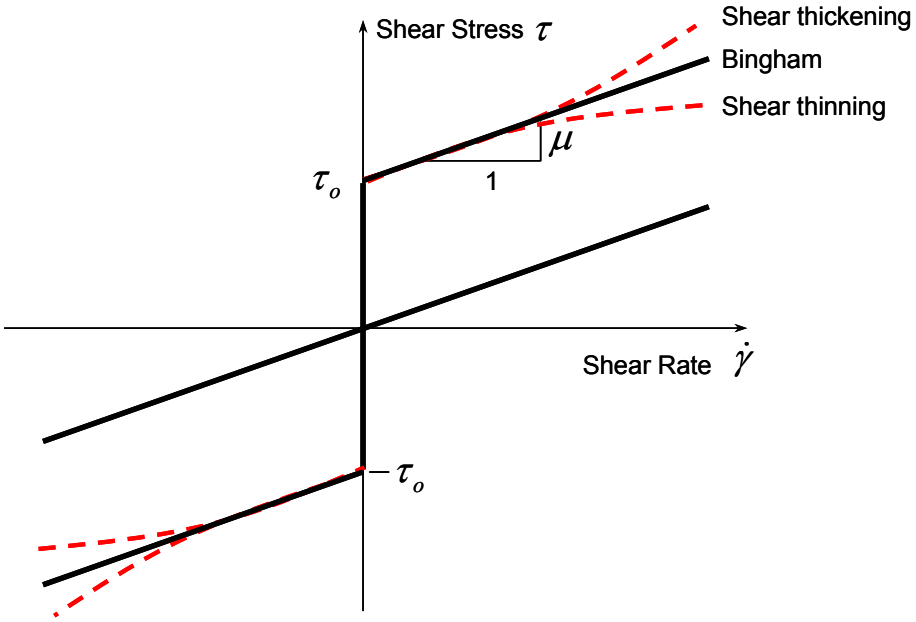

Figure 3-1. Visco-plastic models often used to describe MR fluids

An alternative to the Bingham model is the Herschel-Bulkley model which accounts for the post-yield shear thinning behavior of MR fluids. The Herschel-Bulkley model can be expressed as

$$\tau = \pm\tau_o + K\left|\dot{\gamma}\right|^{\frac{1}{m}} \tag{3-2}$$

where K and m are fluid parameters. For $m > 1$ equation (3-2) represents a shear thinning fluid while shear thickening fluids are described by $m < 1$. Note that for $m = 1$ the Herschel-Bulkley model reduces to the Bingham plastic model.

The Bingham and Herschel-Bulkley models have been employed in a number of models used to describe the behavior of specific MR fluid devices. Many such models are derived from the work done by Phillips. Several studies have extended Phillips' work to axisymmetric damper models [52, 53]. In most cases, however, because the gap size is very small in comparison to the annulus diameter, the axisymmetric model is reduced to the parallel plate approximation [52, 54]. It has been shown that the maximum error between the axisymmetric model and the parallel plate approximation is less than 5% [52]. The simplicity of the parallel plate model and the small error justifies its use in

most damper models. Furthermore, parallel flow of MR fluid forms the basis for modeling of MR fluid devices operating in valve or shear mode.

3.2 Quasi-steady parallel flow of MR fluid

In the absence of a magnetic field MR fluid behaves as a Newtonian fluid. However, when the fluid is exposed to a magnetic field a yield stress develops and the fluid behaves as a Bingham fluid with constitutive relation given by

$$\tau = \pm\tau_o + \mu\frac{du}{dy} \tag{3-3}$$

where τ_o is the field dependent yield stress, μ is the viscosity, and du/dy is the shear rate. Figure 3-2 shows the quasi-steady flow of MR fluid through fixed parallel plates. It is important to note that this flow behavior is often used to characterize the fluid flow through an MR valve. The flow behavior depicted in Figure 3-2 can be separated into three distinct regions. Recall that the onset of flow does not occur until the yield stress has been exceeded. Therefore, the flow through the channel can be separated into three distinct regions. In regions I and II, where the shear rate is large, the fluid flows much like the Newtonian case. In region III, however, the fluid is moving as a solid or plug through the channel. In this region, the yield stress, τ_o, has not been exceeded and thus the fluid is not being sheared.

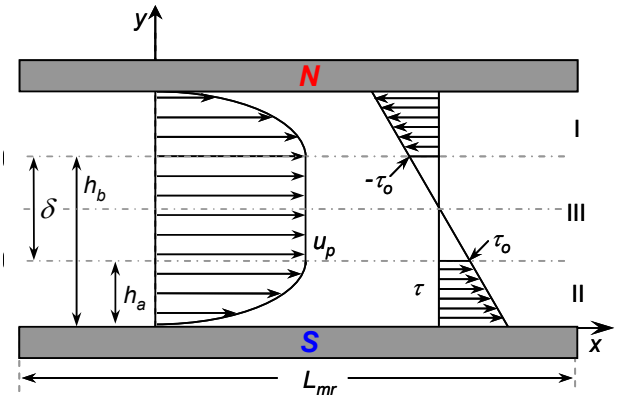

Figure 3-2. MR fluid flow through fixed parallel plates

Our goal is to determine an expression for the pressure drop caused by the flow behavior shown in Figure 3-2. The procedure outlined below begins with a reduced form of the Navier-Stokes equation. By enforcing boundary conditions on both the velocity and the shear rate, the velocity profile is found in terms of the channel geometry shown in Figure 3-2. A momentum balance on the fluid yields the plug geometry and allows for further reduction of the velocity profile. Finally, a cubic expression for the pressure gradient is found from the flow rate and mean velocity. The solution of this cubic equation is found in closed form.

3.2.1 Velocity profile

In order to determine the velocity profile, we begin with a reduced form of the Navier-Stokes equation for one-dimensional flow given by [55]

$$\rho\left(\frac{\partial u}{\partial t}+u\frac{\partial u}{\partial x}\right)=\rho g_x-\frac{\partial p}{\partial x}+\mu\frac{\partial^2 u}{\partial y^2} \tag{3-4}$$

Assuming fully developed and horizontal flow, the momentum equation can be further reduced to

$$\frac{d^2u}{dy^2}=\frac{1}{\mu}\frac{dp}{dx} \tag{3-5}$$

Integration of the momentum equation and enforcing the boundary conditions on shear rate in each region

$$\frac{du}{dy}(h_a)=0 \qquad 0\le y\le h_a \tag{3-6}$$

$$\frac{du}{dy}=0 \qquad h_a\le y\le h_b \tag{3-7}$$

$$\frac{du}{dy}(h_b)=0 \qquad h_b\le y\le h \tag{3-8}$$

we obtain expressions for the shear rate. Shear rates for regions I and II are found from equation (3-6) and equation (3-8) as

$$\frac{du}{dy} = \frac{1}{\mu}\frac{dp}{dx}\left(y - h_a\right) \qquad 0 \le y \le h_a \tag{3-9}$$

$$\frac{du}{dy} = \frac{1}{\mu}\frac{dp}{dx}\left(y - h_b\right) \qquad h_b \le y \le h \tag{3-10}$$

From the shear rates, the velocity in each region can be found by integrating once more with respect to y and enforcing the following boundary conditions:

$$u(0) = 0 \qquad 0 \le y \le h_a \tag{3-11}$$

$$u = u_p \qquad h_a \le y \le h_b \tag{3-12}$$

$$u(h) = 0 \qquad h_b \le y \le h \tag{3-13}$$

From equation (3-11) and equation (3-13), the velocity profiles in regions I and II are found in terms of the plug geometry as

$$u = \frac{1}{2\mu}\frac{dp}{dx}y\left(y - 2h_a\right) \qquad 0 \le y \le h_a \tag{3-14}$$

$$u = \frac{1}{2\mu}\frac{dp}{dx}\left[\left(y^2 - h^2\right) - 2h_b\left(y - h\right)\right] \qquad h_b \le y \le h \tag{3-15}$$

3.2.2 Plug geometry

In order to fully define the velocity profile, the three unknowns, h_a, h_b, and u_p, must be found. From either equation (3-14) or equation (3-15), the plug velocity can be found from the condition $u_I(h_a) = u_p$ or $u_{II}(h_b) = u_p$. Evaluating the velocity in region I at $y = h_a$, we find an expression for the plug velocity

$$u_p = -\frac{h_a^2}{2\mu}\frac{dp}{dx} \tag{3-16}$$

An expression for the plug thickness, $\delta = h_b - h_a$, can be found by enforcing equilibrium on the plug. Consider the fluid element shown in Figure 3-3. The only forces acting on the element are due to the pressure gradient and the shear forces acting on the element.

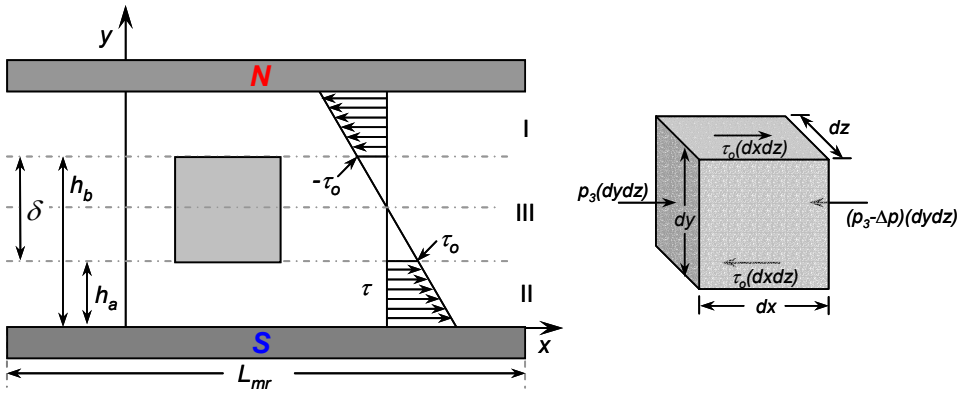

Figure 3-3. Balance of forces on a fluid element in the plug region

A balance of forces on the fluid element shown in Figure 3-3 yields

$$\Delta p dy dz = -2\tau_o dx dz \tag{3-17}$$

where the clockwise rotation of the element due to the shear stress is denoted as positive [51]. In terms of the plug geometry, equation (3-17) can be written as

$$\frac{dp}{dx}\delta = -2\tau_o \tag{3-18}$$

The plug thickness is then

$$\delta = h_b - h_a = -\frac{2\tau_o}{dp/dx} \tag{3-19}$$

Due to the symmetry of the velocity profile we know $h_b = h - h_a$ and thus from equation (3-19) we can determine the geometry of the plug as

$$h_a = \frac{h}{2} + \frac{\tau_o}{dp/dx} \tag{3-20}$$

$$h_b = \frac{h}{2} - \frac{\tau_o}{dp/dx} \tag{3-21}$$

The velocity profiles can now be written in terms of the known quantities, τ_o and h, as

$$u = \frac{1}{2\mu}\frac{dp}{dx}y(y-h) - \frac{\tau_o}{\mu}y \qquad 0 \le y \le h_a \tag{3-22}$$

$$u = \frac{1}{2\mu}\frac{dp}{dx}y(y-h) + \frac{\tau_o}{\mu}(y-h) \qquad h_b \le y \le h \tag{3-23}$$

Likewise, the plug velocity can be written as

$$u_p = -\frac{1}{8\mu}\frac{dp}{dx}h^2 - \frac{\tau_o}{2\mu}\left(h + \frac{\tau_o}{(dp/dx)}\right) \tag{3-24}$$

The mean velocity through the channel is obtained by integrating the velocity profile over the thickness of the channel.

$$u_m = \frac{1}{h}\int_0^h u dy = \frac{1}{h}\left[\int_0^{h_a} u dy + \int_{h_a}^{h_b} u dy + \int_{h_b}^{h} u dy\right] \tag{3-25}$$

Recalling that $h_b = h - h_a$, we have

$$u_m = \frac{1}{h}\left[\frac{1}{3\mu}\frac{dp}{dx}\left(4h_a^3 - 3h_a^2 h\right) - \frac{\tau_o}{\mu}h_a^2\right] \tag{3-26}$$

Substituting the expression for h_a from equation (3-20), an alternative expression for the mean velocity is found.

$$u_m = -\frac{1}{12\mu}\frac{dp}{dx}h^2 - \frac{1}{4\mu}h\tau_o + \frac{1}{3\mu h}\frac{\tau_o^3}{(dp/dx)^2} \tag{3-27}$$

Note that for $\tau_o = 0$, equation (3-27) reduces to the mean velocity for the Newtonian case. Furthermore, should u_m and τ_o be known, equation (3-27) results in a third order equation for the pressure gradient.

$$\left(\frac{dp}{dx}\right)^3 + \left(\frac{12u_m\mu}{h^2} + \frac{3\tau_o}{h}\right)\left(\frac{dp}{dx}\right)^2 - \frac{4\tau_o^3}{h^3} = 0 \tag{3-28}$$

With $\tau_o = 0$, equation (3-28) reduces to the Newtonian case

$$\left(\frac{dp}{dx}\right)_N = -\frac{12u_m\mu}{h^2} \tag{3-29}$$

We also consider the opposite extreme in which flow does not occur due to the formation of a plug of width *h*. When $\delta = h$, from equation (3-19) we can write an expression for the critical pressure drop

$$\left(\frac{dp}{dx}\right)_C = -\frac{2\tau_o}{h} \tag{3-30}$$

which is the lowest pressure gradient that would still generate flow between the parallel plates. Thus, in order to have flow the following condition must be satisfied:

$$\frac{dp}{dx} \geq \left(\frac{dp}{dx}\right)_C \tag{3-31}$$

3.2.3 Closed form solution for pressure gradient

In order to solve equation (3-34) for the pressure gradient, we first normalize with respect to the Newtonian case

$$\left(\frac{dp}{dx}\Big/\frac{dp}{dx}_N\right)^3 - \left(1+\frac{3\tau_o h}{12u_m\mu}\right)\left(\frac{dp}{dx}\Big/\frac{dp}{dx}_N\right)^2 + 4\left(\frac{\tau_o h}{12u_m\mu}\right)^3 = 0 \tag{3-32}$$

With the introduction of the following two non-dimensional parameters [51]

$$\mathcal{P} = -\frac{dp}{dx}\frac{h^2}{12u_m\mu} \tag{3-33}$$

$$\mathcal{T} = \frac{\tau_o h}{12u_m\mu} \tag{3-34}$$

equation (3-32) can be written in the familiar form first presented by Phillips [51].

$$\mathcal{P}^3 - (1+3\mathcal{T})\mathcal{P}^2 + 4\mathcal{T}^3 = 0 \tag{3-35}$$

The procedure for determining the closed form solution of equation (3-35) is well documented by Gavin [56], but for completeness, the solution is summarized here. The solution begins with a transformation of the form

$$\mathcal{P} = x - \lambda \tag{3-36}$$

where λ is chosen to be

$$\lambda = -\frac{1+3\mathcal{T}}{3} \tag{3-37}$$

such that the second order term vanishes. The resulting polynomial in x is then

$$x^3 - \frac{1}{3}\left(1+3\mathcal{T}\right)^2 x + 4\mathcal{T}^3 - \frac{2}{27}\left(1+3\mathcal{T}\right)^3 = 0 \tag{3-38}$$

With the definition of the polynomial coefficients

$$a = -\frac{1}{3}\left(1+3\mathcal{T}\right)^2 \tag{3-39}$$

$$b = 4\mathcal{T}^3 - \frac{2}{27}\left(1+3\mathcal{T}\right)^3 \tag{3-40}$$

equation (3-38) can be written in the standard form

$$x^3 + ax + b = 0 \tag{3-41}$$

In this form, a solution can always be obtained by transforming to the trigonometric identity [57]

$$4\cos^3\theta - 3\cos\theta - \cos(3\theta) \equiv 0 \tag{3-42}$$

Let $x = m\cos\theta$, then

$$m^3\cos^3\theta + am\cos\theta + b \equiv 4\cos^3\theta - 3\cos\theta - \cos(3\theta) \equiv 0 \tag{3-43}$$

Equation (3-43) is always satisfied for

$$\frac{4}{m^3} = -\frac{3}{am} = \frac{-\cos(3\theta)}{b} \tag{3-44}$$

It follows then that

$$m = 2\sqrt{-\frac{a}{3}} \tag{3-45}$$

and

$$\cos(3\theta) = \frac{3b}{am} \tag{3-46}$$

From equations (3-39) and (3-40), alternative expressions for m and θ can be found as

$$m = \frac{2}{3}(1 + 3T) \tag{3-47}$$

$$\theta = \frac{1}{3}\cos^{-1}\left(1 - \frac{54T^3}{(1+3T)^3}\right) \tag{3-48}$$

from which it follows that

$$\mathrm{x} = \frac{2}{3}(1+3\mathcal{T})\cos\left[\frac{1}{3}\mathrm{acos}\left(1 - \frac{54\mathcal{T}^3}{(1+3\mathcal{T})^3}\right)\right] \tag{3-49}$$

From the transformation in equation (3-36) we find the solution for $\mathcal{P}$

$$\mathcal{P}(\mathcal{T}) = \frac{2}{3}(1+3\mathcal{T})\left[\cos\left(\frac{1}{3}\mathrm{acos}\left(1 - \frac{54\mathcal{T}^3}{(1+3\mathcal{T})^3}\right)\right) + \frac{1}{2}\right] \tag{3-50}$$

Equation (3-50) provides the solution for the non-dimensional pressure gradient, $\mathcal{P}$, in terms of the non-dimensional yield stress, $\mathcal{T}$. From this solution, an expression for the pressure drop in the flow channel can be written in terms of the channel geometry as

$$\Delta P_\tau = \frac{12\mathcal{P}u_m\mu}{h^2}L_{mr} \tag{3-51}$$

Equation (3-51) represents the pressure drop developed in the MR valve. This pressure drop is responsible for the controllability of the MR device.

3.3 Modeling the yield stress

Another important relationship regarding MR fluid behavior is the yield stress as a function of applied field strength. It is well known that the yield stress developed in the fluid increases monotonically with growing magnetic field strength. The yield stress continues to increase until the fluid reaches magnetic saturation. This is well illustrated in Figure 3-4. The magnetic induction curve, or B-H curve, shown in Figure 3-4a indicates that as field strengths increase, the induction, B, approaches saturation. The saturation observed in magnetic induction is accompanied by a saturation in yield stress

as shown in Figure 3-4b. A thorough discussion of the magnetic behavior of MR fluids can be found in the work by Jolly et al. [58].

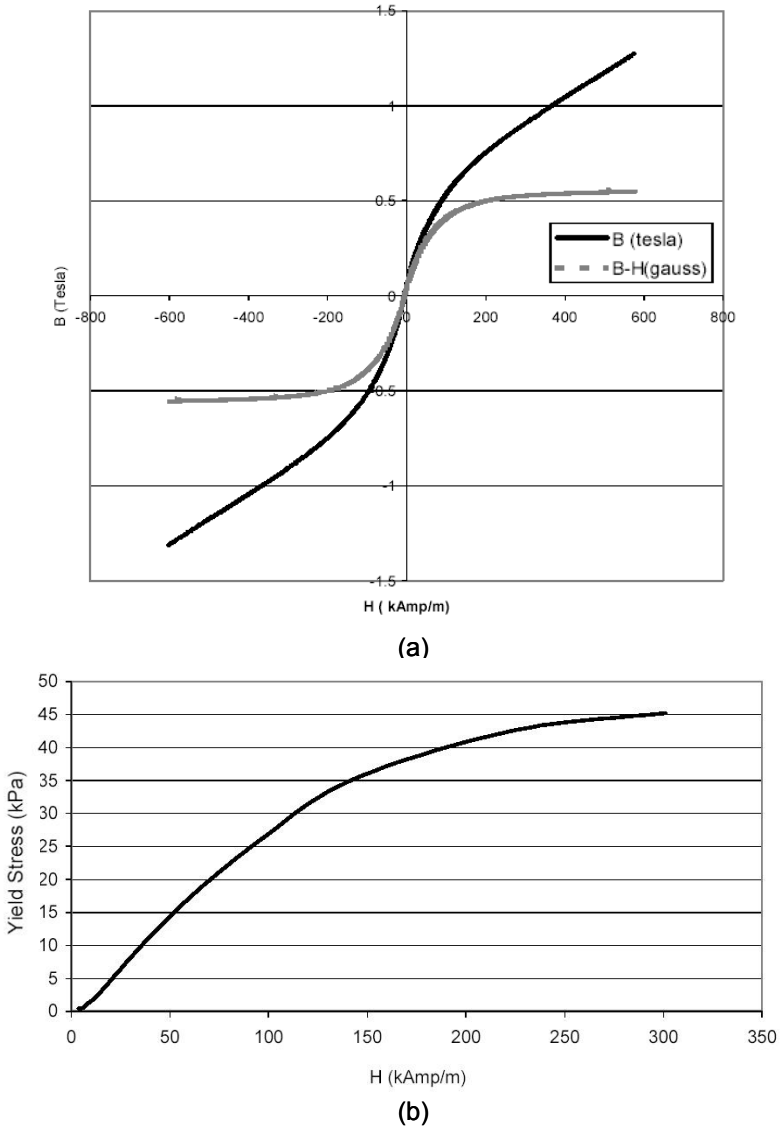

Figure 3-4. Magnetic properties of MRF-132LD (© 2005 Lord Corporation [59]. All rights reserved): (a) magnetic induction curves; (b) yield stress as a function of applied field

A model of the behavior shown in Figure 3-4 is presented in the work by Carlson [60]. Though the magnetic properties shown in Figure 3-4 are specific to MRF-132LD,

the model proposed by Carlson is general and works for any MR fluid. The proposed model relates the yield stress to the magnetic field strength as

$$\tau_o = C \cdot 271700 \cdot \Phi^{1.5239} \cdot \tanh\left(6.33 \cdot H\right) \tag{3-52}$$

where Φ is the particle loading, and H is the field strength in A/m. The constant C depends on the carrier fluid and is given as

$C = 0.95$ silicone oil
$C = 1$ hydrocarbon oil
$C = 1.16$ water

Figure 3-5 shows the predicted yield stress as a function of applied field for several MR fluids available from Lord Corporation. The expression in equation (3-52) accurately represents the yield stress for each of these fluids.

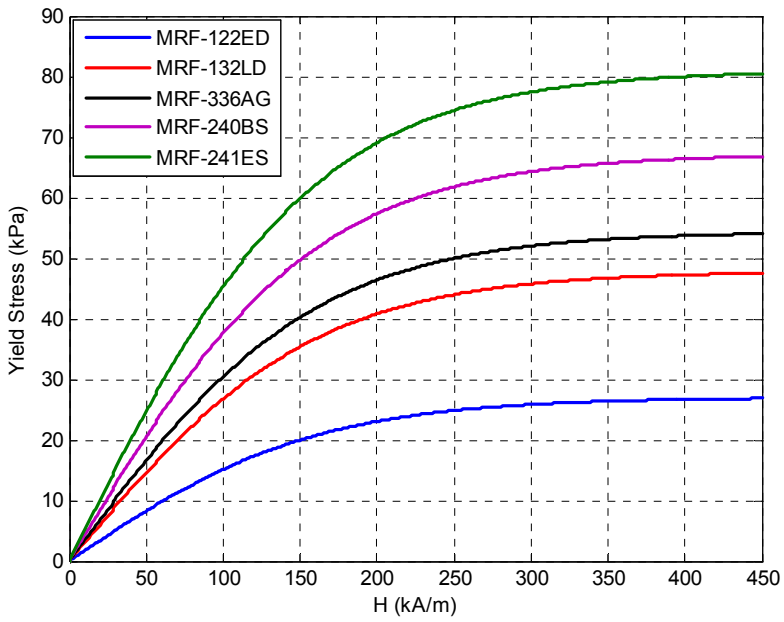

Figure 3-5. Predicted yield stress as a function of applied field

Clearly the model proposed in equation (3-52) is a function of the magnetic field strength and certain fluid properties. However, the model does not account for the condition in which the fluid is being used. This model assumes that the yield stress will

be developed, regardless of the operating conditions of the fluid. As will be shown in Chapter 6, this assumption is not valid under certain operating conditions.

3.4 Summary of MR fluid models

With the great number of MR fluid devices and applications, fluid models that offer accurate representations of the fluid are of great importance. Existing fluid models can provide insight into the performance of a particular device long before implementation. However, we must consider the suitability of such models in describing fluid behavior under adverse operating conditions. Though these extreme operating conditions are rarely considered, the fluid is often exposed to these conditions in everyday operation of many MR devices. Existing models, however, may be unsuitable for describing the fluid behavior under adverse conditions. Both the behavior under adverse operating conditions, and the model's ability to represent the fluid under these conditions, will be addressed in the coming chapters.

4 Experimental Approach

The principal objective has been identified as investigating the high velocity and high shear behavior of MR fluid. Of key importance is the behavior of the fluid itself, not the behavior of the fluid operating in a particular device. The results must be general such that they are not specific to a particular device geometry. The simple geometry of the rheometer allows for the results to be extrapolated to any MR device geometry. To this end, a rheometer was designed and built which allowed for the high flow testing of MR fluid. Fluid behavior was to be investigated in the off-state as well as the on-state. As such, the rheometer had to be designed such that a magnetic field could be applied to the fluid.

This chapter discusses the design of the slit-flow rheometer. A detailed description of the design and geometry of the rheometer are provided. Furthermore, a brief description of the sensors and data acquisition system is also provided. This chapter concludes by documenting the experimental procedure used in testing.

4.1 Design of slit-flow rheometer

With one of the primary objectives targeted at characterizing MR fluid behavior at high shear rates, the rheometer needed to be designed in a way that would allow for high velocity testing. To this end, a Venturi concept was adopted. Exploiting conservation of mass we are able to use relatively low piston velocities to generate high fluid velocity in the slit. Consider the schematic shown in Figure 4-1. Conservation requires that flow rate be maintained. Thus, the velocity exiting the Venturi is proportional to v_1 as

$$v_2 = \frac{A_1}{A_2} v_1 \tag{4-1}$$

As the area ratio increases, the velocity at the exit increases. This simple property is exploited in the design of the rheometer.

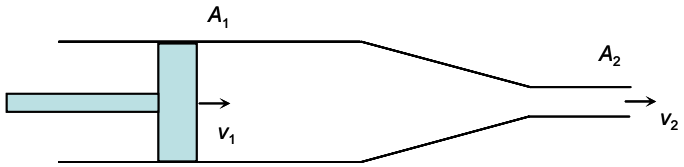

Figure 4-1. Venturi schematic

The overall assembly of the slit-flow rheometer is shown in Figure 4-2. Several primary components are identified: the main bore, the reducer, the flow channel, the electromagnet, the actuator, and the fill reservoir. Figure 4-2b also shows the thermocouple used to measure fluid temperature and the Hall probe used to measure the field strength. Each of these components will be discussed in detail in the following sections.

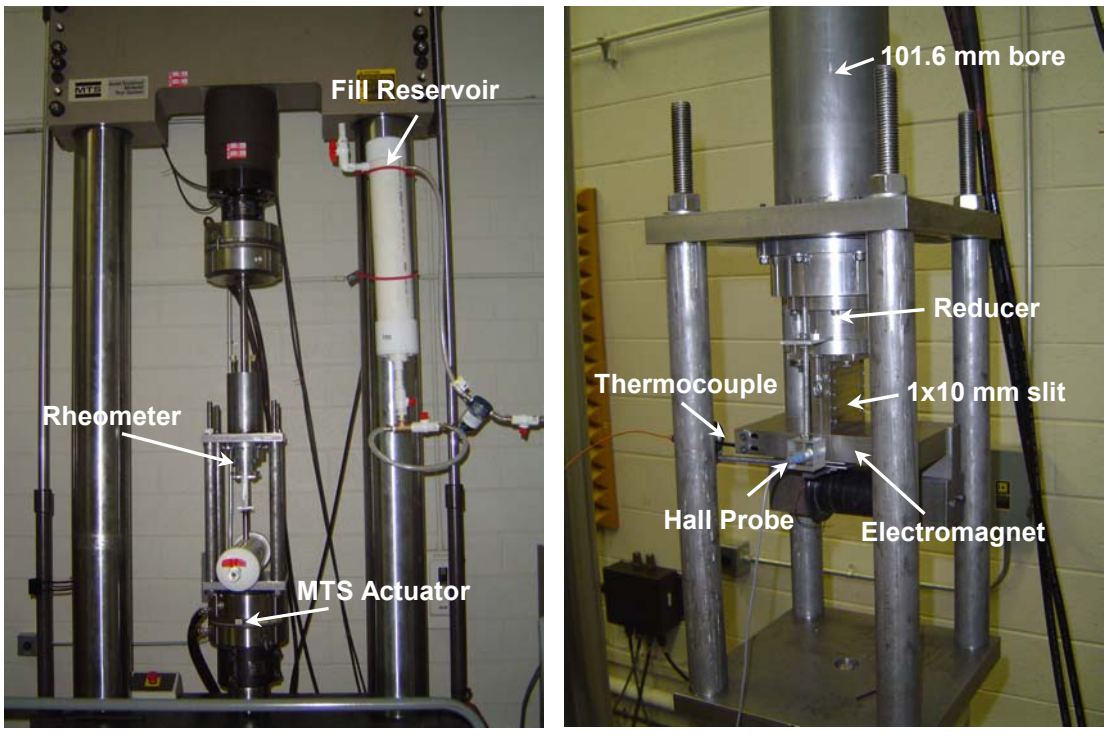

Figure 4-2. (a) MR rheometer mounted in MTS load frame; (b) Close-up of MR rheometer

The hydraulic actuator used in this study is an MTS axial/torsion actuator with a force capacity of 490 kN (110 kips). Because the actuator is bottom actuated, the rheometer was designed to allow for bottom actuation. The framing shown in Figure 4-2b allows the actuation to occur from the bottom. In other words, the entire capillary rheometer moves while the piston is held in place. The actuator force is transmitted through the 25.4 mm thick steel base plate, then through the four steel pipes, into the main tube flange which reacts against the piston, driving the fluid through the flow channel.

In order to achieve a large area ratio, the main tube was chosen to have a 101.6 mm (4 inch) bore. The main tube (Figure 4-3) is 4.5" OD by 4.0" ID honed DOM steel, supplied by Scot Industries Inc. When assembled, the area ratio of the rheometer is greater than 1000. A 25.4 mm (1 inch) thick steel flange is welded to the end of the tube so that it can be bolted to the reducing section. A fiber gasket rated at 5000 psi is used to seal the connection between the main tube and the reducing section. The tube length is 222.25 mm (8.75"). This length is limited by the stroke of the hydraulic actuator being used in this study. A longer tube is desirable because it allows for multiple tests in a single stroke. It should be noted that the main tube is free of holes along its length. Holes along the length of the tube are undesirable as they can damage piston seals.

Figure 4-3. Main tube

The piston that was used to drive the fluid through the rheometer was made from 7075-T6 aluminum. Figure 4-4 shows the piston along with the nylon bushing. The

nylon bushing serves merely as a second point of contact to support any lateral loading. A polyurethane or Viton® o-ring serves as the dynamic seal in the rheometer. The two holes in the piston were designed to allow for top filling of the capillary rheometer. Top filling the rheometer prolonged the life of the seals because the main bore was free of holes or other obstructions. The piston rod was a 22.23 mm (7/8") OD hardened precision steel shaft.

Figure 4-4. Piston with Viton® o-ring and nylon bushing

The reducer was designed to reduce the diameter from the 101.6 mm bore of the main tube to the 10 mm width of the flow channel. For ease of machining, the reducer was made from 7075-T6 aluminum. The length of the reducer was chosen such that the included angle was less than 50 degrees. An included angle of 50 degrees along with an area ratio (A_2/A_1) of ~0.01 results is a head loss coefficient less than 0.1 [61]. The reducer is shown in Figure 4-5. It should be noted that the reducer was made from two independent parts. Again, to simplify the machining, two reducers were made, one reducing the diameter from 101.6 mm to 50.8 mm, and the other reducing the diameter from 50.8 mm to 10 mm. Here again, a fiber gasket is used to seal the connection.

Figure 4-5. Reducer - used to reduce diameter from 101.6 mm to 10 mm

One rather important design detail is the geometry of the flow channel. The rheometer was designed such that the parallel plate assumption could be made. If the aspect ratio is greater than or equal to 10, then there is no side wall effect [62]. As such, the dimensions of the rectangular channel were chosen such that the width of the channel is at least 10 times the height of the channel. Figure 4-6 shows the flow channel with the 1 mm x 10 mm channel. The ratio of the length of the flow channel to the height of the slit is large enough that end effects can be neglected [63]. The MR valve is incorporated into the last 25.4 mm of the 101.6 mm channel. While two MR valve lengths were considered, 25.4 mm and 6.35 mm, the overall length of the flow channel remained at 101.6 mm. When testing with the 6.35 mm valve, a stainless steel blank was installed to make up the remainder of the length. It was important to maintain the overall length so that the results could be compared directly for both MR valve lengths. The best performance for an MR valve results from a rectangular geometry in which the fluid is in direct contact with the magnetic poles [64]. As such, the flow channel was made in a modular fashion; two stainless steel plates were sandwiched together, separated by a 1 mm stainless steel spacer. The valve portion of the rheometer is made from low carbon steel. Through this design we are able to modify the effective pole length of the valve by simply changing the length of the low carbon steel portion. Furthermore, the slit dimensions can be changed simply by replacing the stainless steel spacers.

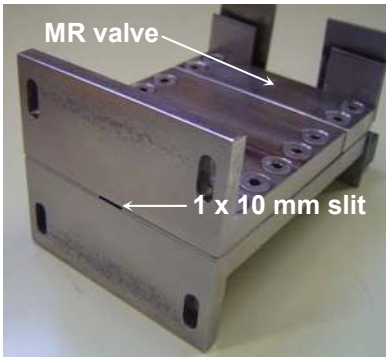

Figure 4-6. 1x10 mm flow channel and MR valve

Because the geometry of the flow channel has a significant effect on the fluid velocity and the shear rate, care had to be taken when assembling the flow channel. Before the two halves of the flow channel were assembled they were skimmed on a mill using a fly-cutter. This eliminated any imperfections in the assembly alignment of the MR valve and the stainless steel plate. The two halves were then smoothed using 100C silicon carbide abrasive paper. The resulting surface finish was such that the flow channel could be assembled without the use of a seal between the 1 mm spacer and the channel halves. The care taken in assembling the flow channel ensured that the flow channel gap was uniform throughout the flow channel. Furthermore, an accurate measurement of the gap height is easily achieved by simply measuring the thickness of the stainless steel spacer.

The electromagnet used in this study was made from 12L14 steel and is capable of generating field strengths in excess of 700 kA/m in the flow channel. The magnet, shown in Figure 4-7a, has 6 layers of 20 AWG magnet wire, resulting in approximately 600 turns. The magnet is installed on the rheometer such that the magnet poles are in direct contact with the pole areas of the flow channel, as shown in Figure 4-7b. A flux probe mounted between the two MR valve plates, adjacent to the flow path, is used to measure the strength of the magnetic field. In order to confirm uniformity of magnetic field strength through the flow channel, several tests were performed to calibrate the measurements. The difference in field strength measured in the flow path and in the adjacent location was found to be less than 3%.

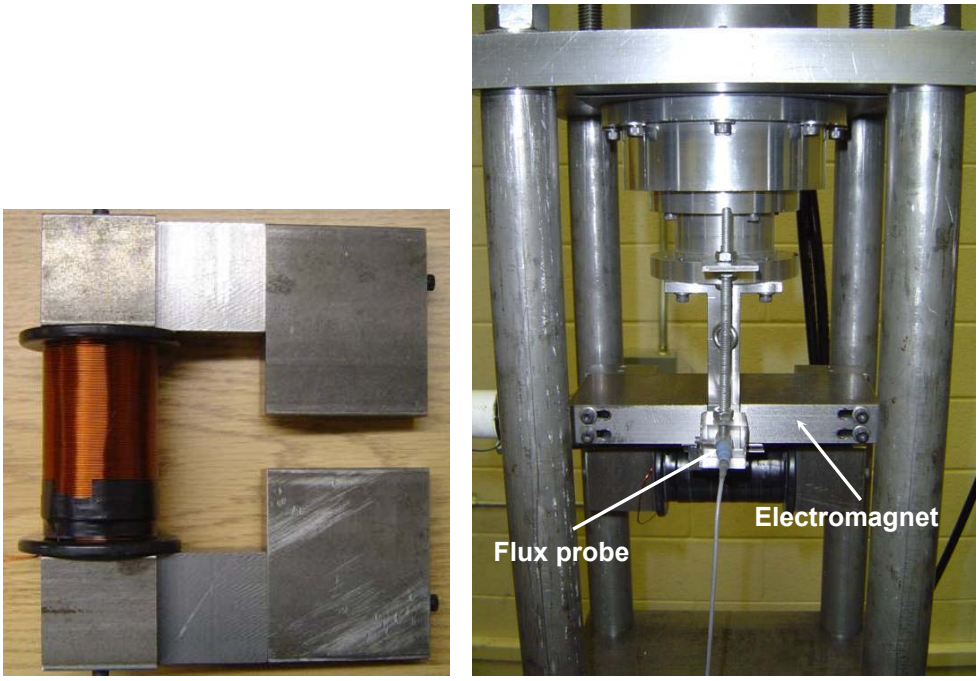

Figure 4-7. Electromagnet used to activate MR fluid

4.2 Data acquisition system

This section describes the data acquisition system used in the experiments. Both the hardware and software components are discussed. Hardware components include various sensors, controllers, and power supplies. The software components include the MTS TestStar II software and dSPACE Control Desk.

4.2.1 Hardware components

As mentioned earlier, a Hall probe was used to measure magnetic field strength. The probe itself was an "ultra-thin" (0.2 mm x 1.5 mm) transverse probe from F. W. Bell. This probe was connected to an F. W. Bell 5080 Gauss-meter. The probe and meter are shown in Figure 4-8. The 5080 model provides an analog output for recording the field strength. With a ±3 V full-scale output, the field strength could be recorded for each

experiment. Because the full-scale of the data acquisition system was ±10 V, the output of the Gauss-meter was gained in order to achieve better resolution.

Figure 4-8. Gauss-meter and "ultra-thin" transverse probe

The temperature of the fluid can contribute significantly to the behavior of the fluid. As such, a thermocouple was used to monitor the temperature of the fluid at the exit of the rheometer. Figure 4-9a shows the placement of the thermocouple probe at the exit of the rheometer. The probe used in this study was an Omega type J. The probe was encased in a stainless steel sheath with a diameter of 0.02" (~ 0.5 mm). A Fluke-52 thermocouple reader was used to monitor the temperature. The probe was used to read an initial temperature before the test began and also to record the rise in temperature due to shear heating of the fluid as it flows through the slit. The time response of the fluid was also of particular interest. For this reason, the voltage output of the probe was recorded by the data acquisition system. A series of digital filters were used to gain the voltage signal to a level that could be recorded by the data acquisition system. Figure 4-8b shows the Fluke-52 along with the digital filters used to condition the voltage output of the probe. The voltage was assumed to vary linearly with temperature over the range of temperatures observed in the experiment. This relationship was confirmed experimentally and the sensitivity of the probe, after conditioning, was found to be 1.84 °C/V.

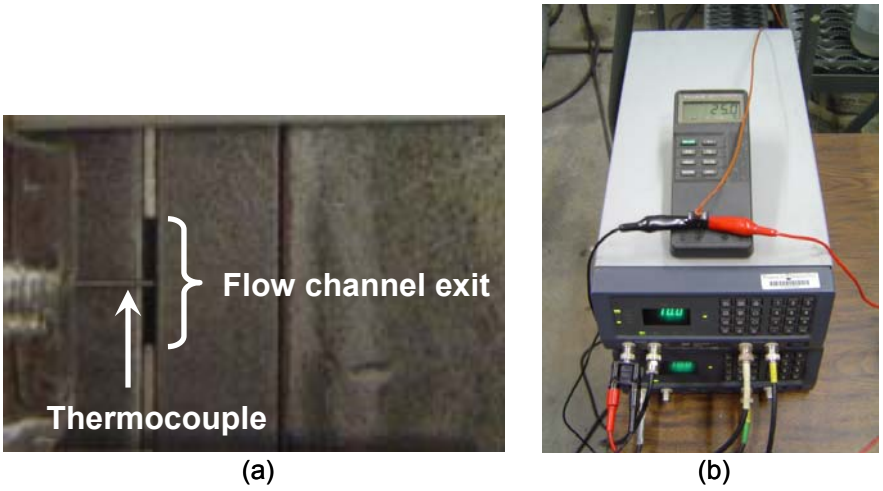

Figure 4-9. Fluid temperature measurements: (a) thermocouple probe mounted at exit of rheometer; (b) Fluke-52 and digital filters used to monitor fluid temperature

The magnet was controlled from within Control Desk. The circuit box and power supplies shown in Figure 4-10 were used to amplify the signal from Control Desk. The circuit box is a current driver circuit which receives input from Control Desk and drives a proportional current through the magnet. The ±15 V power supply is used to power the circuit. The 12 V power supply is used to amplify the output of the circuit to power the magnet.

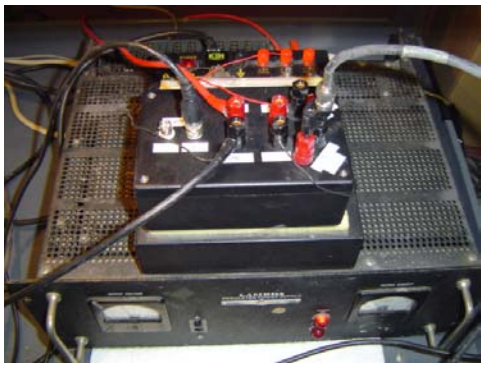

Figure 4-10. Circuit box and power supplies used to power the electromagnet

4.2.2 Software components

The software components of the data acquisition system include MatLab/Simulink and dSPACE ControlDesk. Actuator control and data acquisition were also performed by MTS TestWare SX. The Simulink block diagram used in this study is shown in Figure 4-11. The measured signals were imported through the DS1102ADC (analog to digital converter). The DS1102 is a 4 input, 4 output, PC mounted digital signal processor. Within Simulink, feedback can be provided for control of the electromagnet. Furthermore, real-time manual control of the magnet was also capable through the user interface, dSPACE ControlDesk. The DS1102DAC (digital to analog converter) allowed for real-time control of the electromagnet.

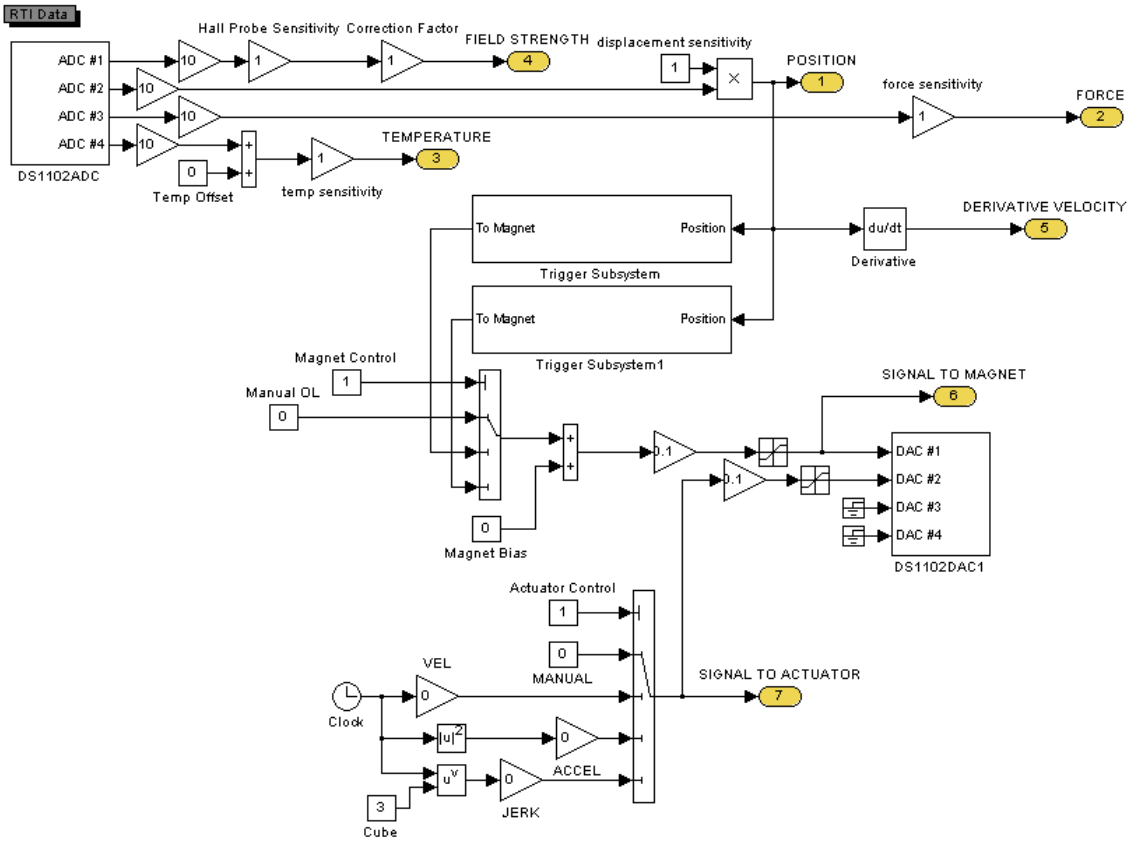

Figure 4-11. Data acquisition and control block diagram

One user interface in this study was dSPACE ControlDesk. ControlDesk allowed for real-time control of various parameters. The primary purpose of ControlDesk was to record the temperature response of the fluid and to control the electromagnet. The force and position were also recorded and displayed on the monitor. Figure 4-12 shows an example of one experiment captured with ControlDesk.

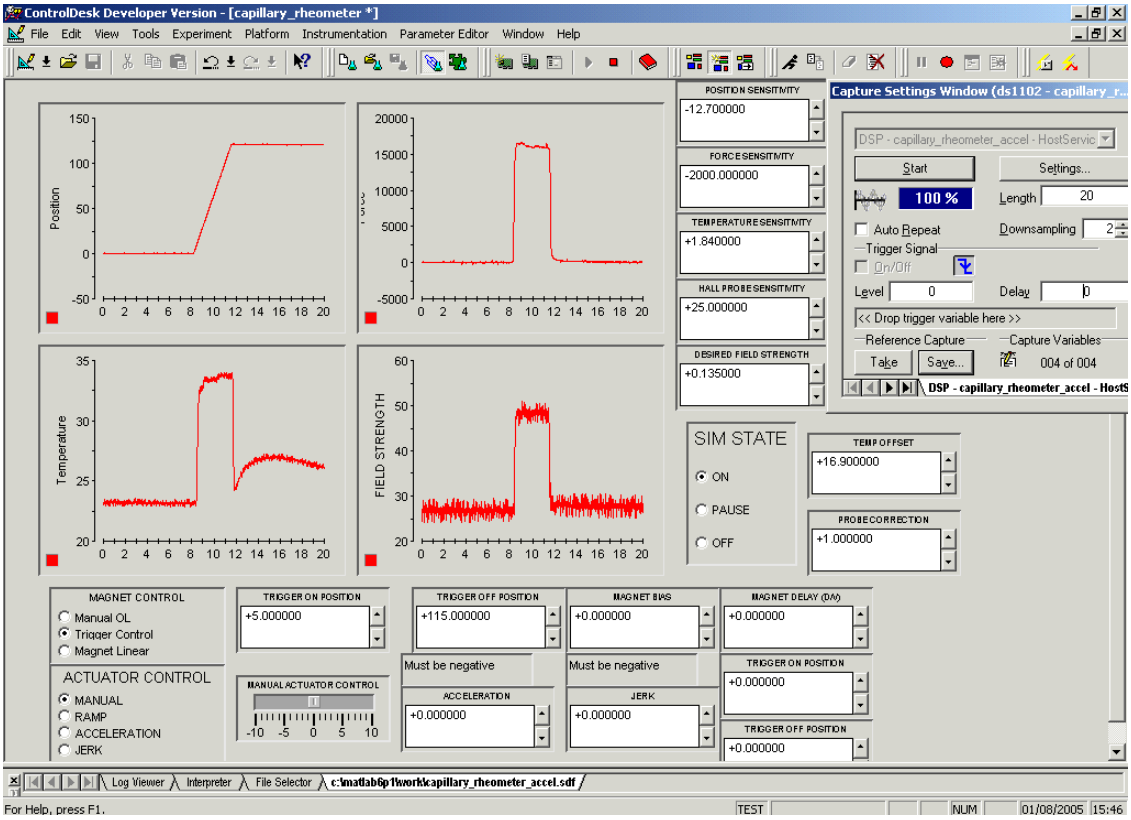

Figure 4-12. dSPACE ControlDesk used to monitor various signals and to control the electromagnet

The other user interface used in this study was MTS TestWare SX. This software was used to define the input to the hydraulic actuator. Figure 4-13 shows the user interface for the TestWare SX software. Within this software, the user can build the desired input signal using a number of built in functions and signal types. Furthermore, the user can define any stroke or force limitations. Once the desired input signal has been built, the user can also define specific parameters such as the rate of stroke (piston velocity), and maximum stroke according to each experiment.

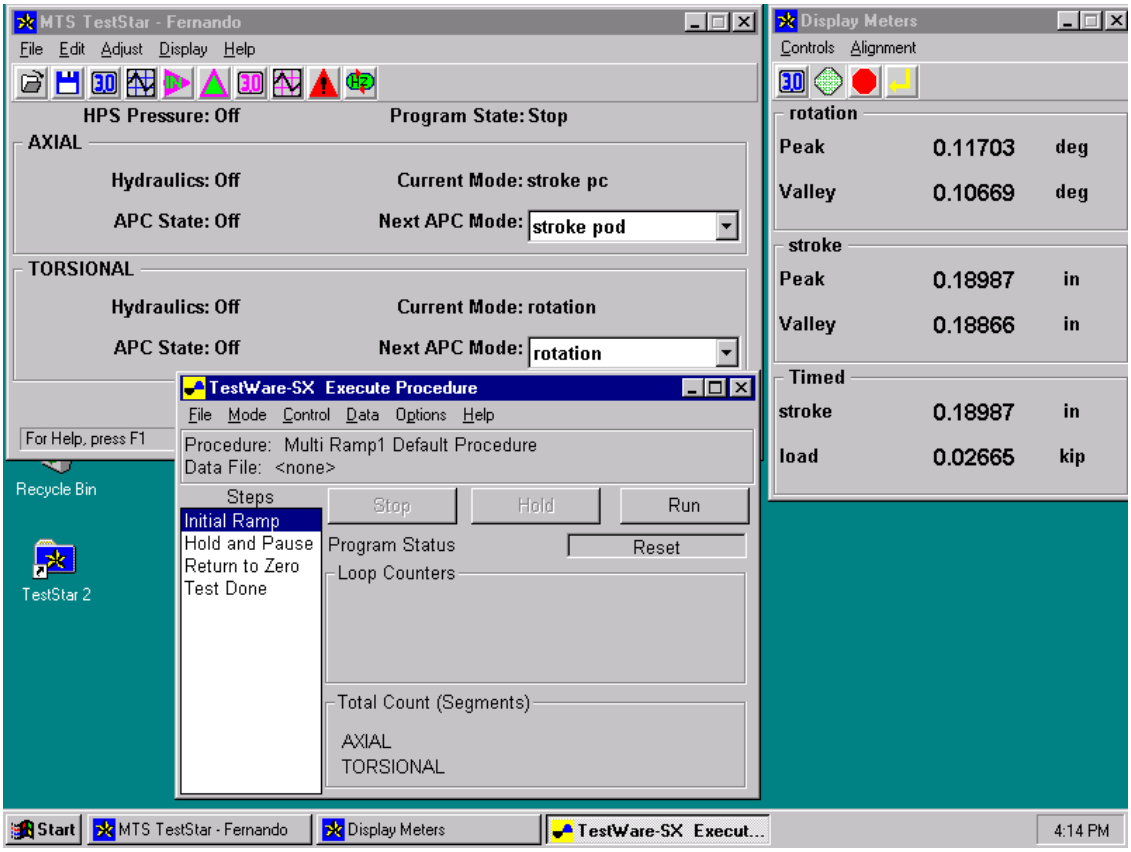

Figure 4-13. MTS TestWare SX software used to control hydraulic actuator

4.3 Experiment procedures

Through the experiment we hope to identify the performance of MR fluid at high velocities. Velocity and magnetic field strength are the only variables. Defining the piston velocity, a corresponding fluid velocity in the flow channel can be calculated from the area ratio. A ramp signal is used as the input to the system. This constant velocity input ensures that the force reaches steady-state, and that the flow is steady flow. In order to avoid any transient loading associated with the MR fluid yield stress, a trigger is used to turn on the electromagnet, only after the fluid has begun to flow. It is relatively important that the fluid be in an amorphous state before testing begins. Otherwise, large transient forces can occur.

Figure 4-14 shows the input used during testing. The piston velocity, v_p, and the stroke are defined in the TestWare SX software. Once the actuator position reaches a predetermined value, normally 5 mm, the electromagnet is turned on. At 5 mm from the end of the stroke, the electromagnet is turned off to prevent the fluid particles from being in an energized state when the fluid is not flowing. Once the actuator reaches the maximum stroke, the program is paused. The program waits for the user to resume testing. The pause is used to open a breather valve so when the actuator is lowered to its initial position, air is not drawn in through the bottom of the rheometer. The test is repeated for each velocity and magnetic field strength. With a large stroke and low piston velocities, it is possible to run several velocities before reaching the stroke limit. This is the advantage of having a large stroke.

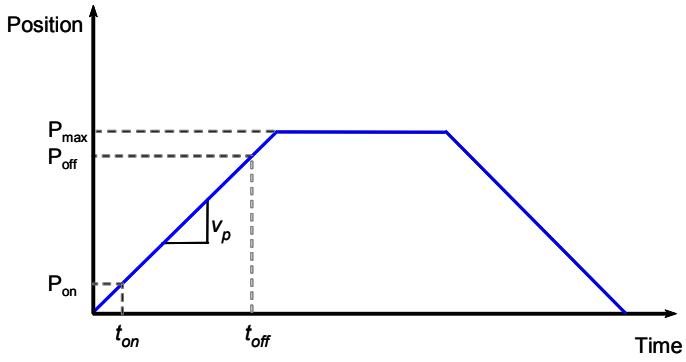

Figure 4-14. Ramp input used in steady flow experiments

Piston velocities considered in this study ranged from 2 mm/s to 36 mm/s (~ 0.1 in/s – 1.4 in/s). With the 1x10 mm flow channel geometry, these piston velocities correspond to fluid velocities ranging from 2 m/s to 37 m/s (~ 6.7 ft/s – 121 ft/s). The maximum shear rate achieved is 2.5×10^5 s^{-1}. For each velocity several magnetic field strengths were considered, ranging from 100 kA/m to 200 kA/m. For all velocities the fluid was also characterized in the absence of a magnetic field.

4.4 Friction force

Before the fluid was run through the rheometer, it was necessary to determine the friction force inherent in the system. This force must be accounted for when calculating the shear stress and the viscosity of the fluid. Sources of friction include the contact between the piston rod and the nylon bushing as well as the dynamic seal between the o-ring and the cylinder wall. To characterize these sources of friction, the rheometer was run without fluid. The slit-flow portion of the rheometer was removed to eliminate any air pressure that may be generated at high velocities. Several piston velocities were run and the force was measured at each velocity. It should be noted that though the rheometer was empty, the cylinder walls were lubricated. This was done in order to avoid dry friction between the Viton® o-ring and the cylinder walls.

Figure 4-15 shows the friction force as a function of piston velocity. The results indicate that friction is a function of piston velocity. In order to eliminate friction from the analysis of the fluid results, an accurate model for the friction as a function of piston velocity was required. An expression well suited to describe the velocity dependent friction was found to be

$$F_{fr} = 0.3565 \cdot v_p^{-0.2464} \tag{4-2}$$

and is shown along with the experimental data in Figure 4-15.

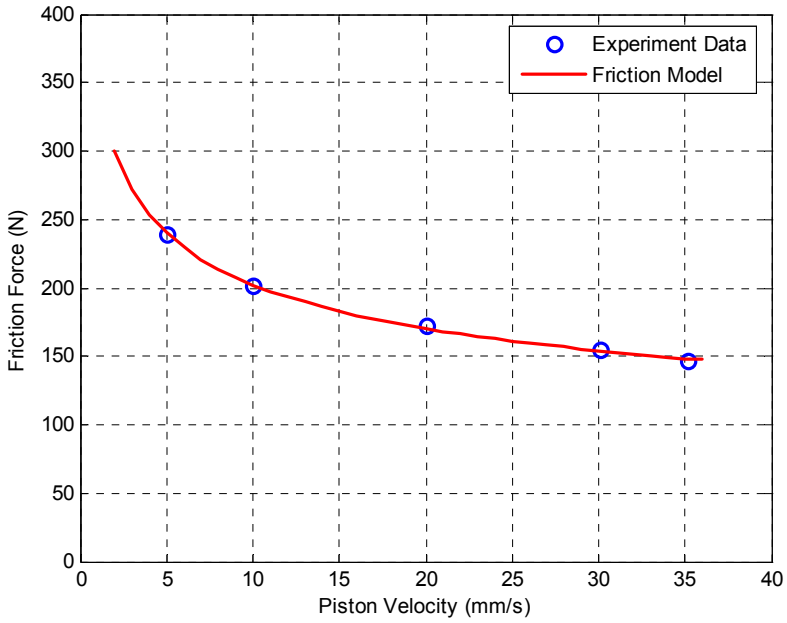

Figure 4-15. Friction model of rheometer

5 Off-State Behavior of MR Fluid at High Shear Rates

Though much of the success of MR fluids can be attributed to the controllable or on-state behavior of the fluid, the off-state behavior of the fluid cannot be overlooked. Much of the literature tends to focus on the behavior of the fluid when exposed to a magnetic field. However, the success of many MR fluid applications is highly dependent on the off-state behavior of the fluid. Furthermore, much of the published data for MR fluids is limited to shear rates and flow velocities that do not completely encompass the environment to which an MR fluid is exposed in an MR device. As such, this chapter examines the behavior of MR fluid in the absence of a magnetic field when subjected to extreme flow conditions, i.e., high shear rates.

The chapter begins with a discussion of the composition of MR fluids. Several factors contribute to the rheological properties of MR fluids. Such factors include concentration and density of particles, particle size and shape distribution, properties of the carrier fluid, additional additives, applied field, temperature, and others. The specific physical properties of MRF-132LD are discussed. Because the behavior of the fluid is highly dependent on the carrier, or host fluid, a characterization of the host fluid is presented. High shear behavior is identified first for the carrier fluid and then for the MR fluid. The high shear viscosity is found for each fluid and, based on the shear stress versus shear rate relationship, a model is proposed for each fluid. The chapter concludes with a discussion of temperature response of the fluid during the high flow experiments.

5.1 Magnetorheological fluid composition

Magnetorheological fluids are non-colloidal suspensions of micron-sized, magnetically polarizable particles. Typical particle diameter is 3-5 μm. As such, MR fluids should not be confused with colloidal ferrofluids in which the particles are 1000 times smaller. In contrast, MR fluids with larger particles have also been considered. Lord Corporation's 180 kN seismic damper employs an MR fluid with particles ranging in size from 0.1 μm to 500 μm, with a preferred size between 1 μm and 100 μm [65]. As particle size increases, however, suspension within the fluid becomes a challenge. This challenge is

amplified in applications where the device is expected to lie dormant for much of its life, as in a seismic damper. Special care was taken to promote particle dispersion and discourage settling in this fluid [8].

MR fluids normally consist of 20-40% by volume of carbonyl iron powder. These soft iron particles are formed from the thermal decomposition of iron pentacarbonyl and are remarkably spherical in shape, as shown in Figure 5-1. These particles are suspended in some form of medium, normally chosen based upon their rheological properties and temperature stability. Common carrier liquids include petroleum based oils, silicone, mineral oils, synthetic hydrocarbon oils, and others [7]. The suspension of the carbonyl iron powder in the host solution is achieved through the use of additives which inhibit settling and agglomeration. Each component of the fluid (the carrier fluid, the iron particles, and the suspension agents) greatly influences the off-state behavior of the fluid. Fluid rheology in the absence of a magnetic field is most notably characterized by its shear thinning viscosity at low shear rates.

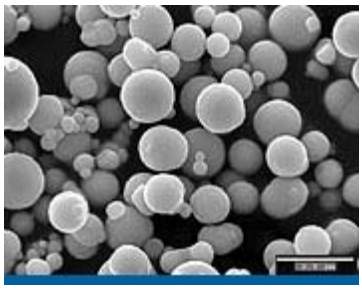

Figure 5-1. SEM image of carbonyl iron powder (image adapted from [66])

5.2 Fluid physical properties

With the composition of the MR fluid identified, what remains is to identify the physical properties of the primary components. Of particular interest are the physical properties of the carrier fluid and the MR fluid used in this study. This section discusses the physical properties of both fluids.

5.2.1 Carrier fluid properties

As mention earlier, the behavior of MR fluid is greatly influenced by the carrier fluid. In fact, at high shear rates, the carrier fluid and suspension agents dominate the behavior [8]. As such, the properties of the carrier fluid should be well understood. The specific host fluid used in MRF-132LD is a synthetic hydrocarbon base oil, called Oronite Synfluid 4 cSt PAO, supplied by the Chevron Phillips Chemical Company in Houston Texas. The physical and chemical properties are taken from the MSDS and are shown in Table 5-1. According to the MSDS, the fluid's kinematic viscosity is 16 cSt, or 0.16 cm^2/s. The relationship between kinematic viscosity, ν, and dynamic viscosity, μ, is defined as

$$\nu = \frac{\mu}{\rho} \tag{5-1}$$

where ρ is the fluid density found from the specific gravity. With a specific gravity of 0.82, the dynamic viscosity is 0.0123 Pa-s. As a point of reference, it is important to note that this viscosity was measured at a temperature of nearly 40 °C as indicated in Table 5-1.

Table 5-1. Physical and chemical properties of carrier fluid (adapted from [67])

Vapor Pressure	1.7 mmHg @ 177 °C
Vapor Density (Air = 1)	> 10
Boiling Point	414 °C
Solubility	Soluble in hydrocarbon solvents; insoluble in water
Specific Gravity	0.82 @ 15.6 °C
Kinematic Viscosity	16 cSt @ 37.8 °C
Pour Point	-73 °C

5.2.2 MRF-132LD properties

The specific type of MR fluid used in this study is Lord Corporation's MRF-132LD. This particular fluid is a hydrocarbon-based MR fluid containing 32% iron by volume. The average particle diameter for this fluid is 3 μm [7]. Basic physical properties of the

fluid are given in Table 5-2. In Table 5-2 we note the impressive range of operating temperatures. This range of operable temperatures is normally limited by the properties of the carrier fluid rather than the polarization of the iron particles [7]. Of particular interest for this research is the viscosity of the fluid. As indicated by Table 5-2, the viscosity is shear dependent. As further illustrated in Figure 5-2, MR fluids exhibit significant shear thinning for shear rates less than 150 s^{-1}. This shear thinning is largely due to the suspension agents in the fluid as well as changes in iron particle microstructure during shear. From Figure 5-2 we note that the rate of shear thinning decreases at high shear rates. The viscosity of the fluid in this regime approaches some asymptote, largely governed by the solids loading, carrier fluid viscosity, and the extent of shear thinning of the suspension agents [8]. The results shown in Figure 5-2 were taken from the Product Bulletin for MRF-132LD. It is important to note that these tests were performed at a controlled temperature of 40 °C using a "bob-and-cup" viscometer [68]. Because a "bob-and-cup" viscometer was used to make the measurements, shear rates are limited to 150 s^{-1}.

Table 5-2. Physical properties of MRF-132LD (adapted from [59])

Base Fluid	Hydrocarbon
Operating Temperature	-40 °C to 130 °C
Density	3.06 g/cm^3
Weight Percent Solids	80.74%
Coefficient of Thermal Expansion 0 to 50 °C 50 to 100 °C 100 to 150 °C	Unit Volume per °C 0.55 x 10^{-3} 0.66 x 10^{-3} 0.67 x 10^{-3}
Specific Heat @ 25 °C	0.80 J/g °C
Thermal Conductivity @ 25 °C	0.25 – 1.06 w/m °C
Flash Point	> 150 °C
Viscosity 10 s^{-1} Shear Rate 80 s^{-1} Shear Rate	 0.94 Pa-s 0.33 Pa-s

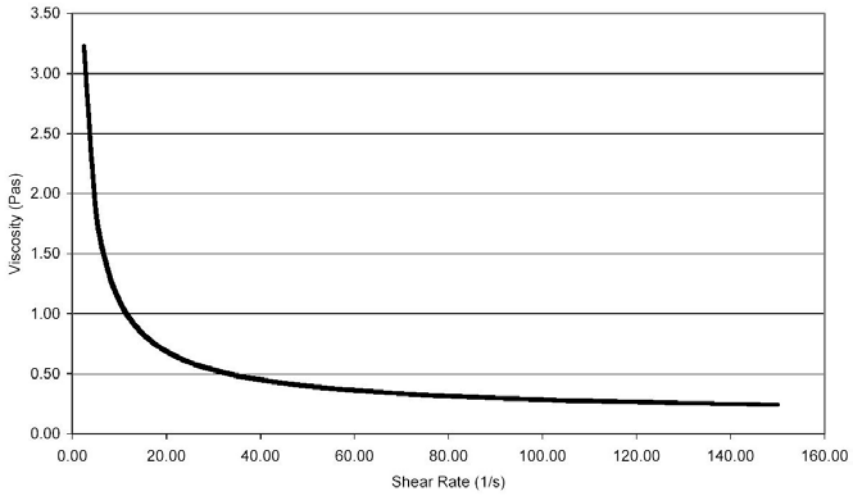

Figure 5-2. Shear thinning behavior of MRF-132LD (© 2005 Lord Corporation [59]. All rights reserved)

5.3 High shear behavior

The high shear behavior of both the carrier fluid and the MR fluid were investigated. MR fluid is often subjected to flow conditions in which the shear rate far exceeds those presented in Section 5.2.2. Furthermore, because results thus far have demonstrated MR fluid's sensitivity to shear rate, there is a need to identify the behavior of the fluid when subjected to high rates of shear. The behavior of the carrier fluid is also of interest. MR fluid behavior is greatly influenced by the host solution. In this section, the behaviors of both the carrier fluid and the MR fluid are explored using the high shear rheometer discussed in Chapter 4.

5.3.1 Calculating the shear stress

Each of the fluids is run through the high shear rheometer at various piston velocities. The force required to drive the fluid through the rheometer is measured. The shear stress is computed from the mean steady-state force. In determining the shear stress, the fluid is assumed to behave as a Newtonian fluid. Thus, the shear stress varies linearly across the thickness, h, as

$$\tau = \mu \frac{du}{dy} = \frac{dp}{dx}\left(y - \frac{h}{2}\right) \tag{5-2}$$

where the pressure gradient, dp/dx, is found from measured force acting over the area of the piston, and along the length of the flow channel. Evaluating the shear stress at the walls yields an expression for the maximum shear stress in the channel in terms of the measured force

$$\tau\big|_{y=(0,h)} = \pm \frac{\Delta P}{L}\frac{h}{2} = \pm \frac{F}{A_p L}\frac{h}{2} \tag{5-3}$$

where A_p and L are the cross-sectional area of the piston and the length of the flow channel, respectively. Shear rate is also maximum at the walls and is found in terms of the fluid velocity, u_m, as

$$\dot{\gamma} = \frac{du}{dy} = \frac{6u_m}{h} \tag{5-4}$$

The apparent viscosity of the fluid is then found from the measured shear stress and the calculated shear rate as

$$\mu = \frac{\tau}{\dot{\gamma}} \tag{5-5}$$

5.3.2 High shear behavior of carrier fluid

The high shear behavior of the carrier fluid was investigated using the rheometer discussed in Chapter 4. Fluid velocities through the flow channel ranged from 2 m/s to 28 m/s with corresponding shear rates ranging from 0.14×10^5 s^{-1} to 2.0×10^5 s^{-1}. Due to the large area ratio, piston velocities were 1000 time smaller than the fluid velocities. Figure 5-3 shows the force versus position for the host solution for each piston velocity. The rise in force observed at 5 mm is due to the o-ring settling into the o-ring groove. The force, soon after, reaches steady-state. From Figure 5-3 we observe that as the piston velocity increases, the change in force grows slightly. This is further confirmed if we consider the shear stress as a function of shear rate.

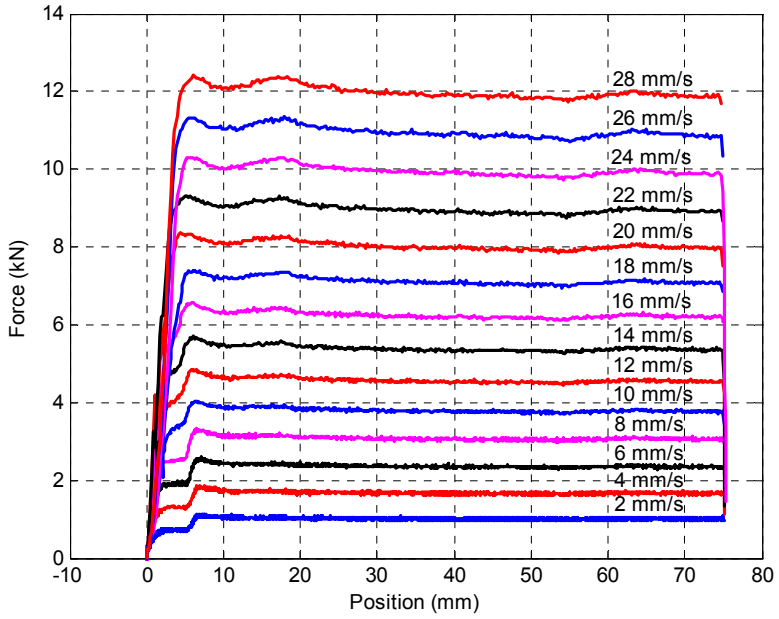

Figure 5-3. Force versus position for carrier fluid

From the mean steady-state force, the shear stress is found from equation (5-3). Figure 5-4a shows the shear stress as a function of shear rate for the carrier fluid. In Figure 5-4 (a) we note that the behavior is not quite Newtonian. A moderate shear thickening is observed for growing shear rates. This behavior is better illustrated if we consider the fluid shear viscosity as a function of shear rate, as shown in Figure 5-4b. The apparent viscosity was defined in equation (5-5) as the measured shear stress divided by the shear rate. Figure 5-4b further demonstrates the shear thickening behavior of the carrier fluid. As a point of reference, it is noted that these experiments were performed at room temperature. Furthermore, fluid initial temperature measurements had a mean value of 24.4 °C. At this temperature, experiments yielded a mean fluid viscosity of 0.03 Pa-s.

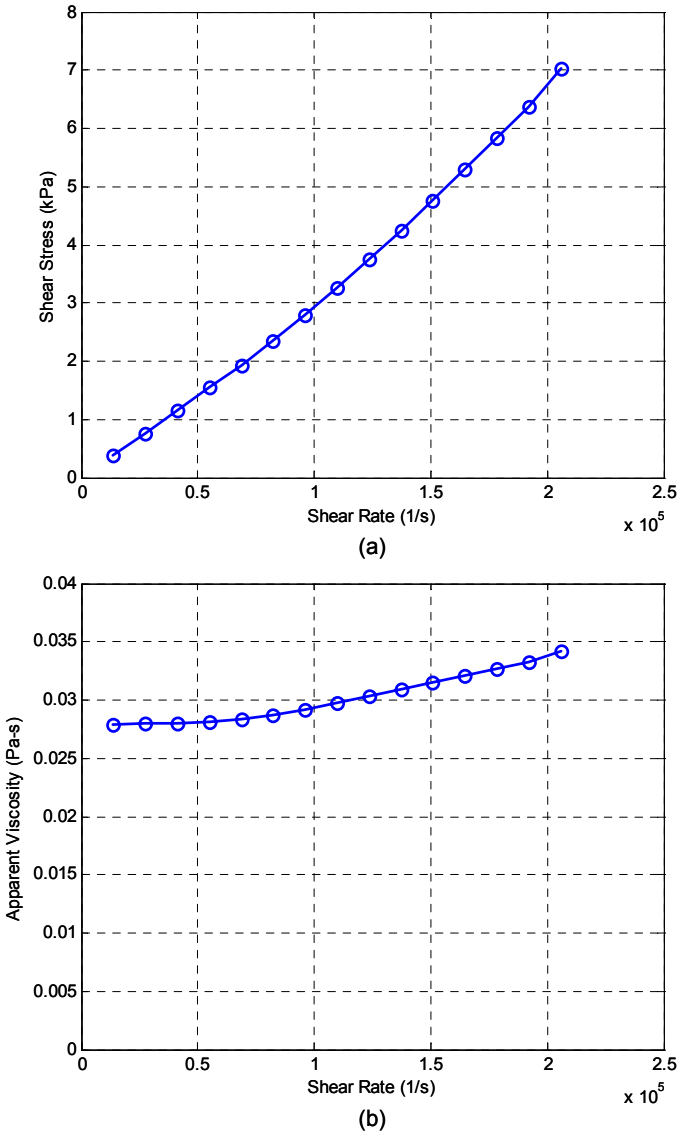

Figure 5-4. Carrier fluid high shear behavior: (a) shear stress versus shear rate; (b) apparent viscosity versus shear rate (collected at an average initial fluid temperature of 24.4 °C)

5.3.3 High shear behavior of MRF-132LD

Once the behavior of the carrier fluid was identified, the same experiments were performed with the MR fluid. In doing so, we are able to identify which behaviors from the host fluid are maintained in the MR fluid. The MR fluid was passed through the rheometer at piston velocities ranging from 2 mm/s to 36 mm/s. Figure 5-5 shows the force response of the fluid over the piston stroke. The measured force reaches steady-

state after a stroke of 40 mm. The slight roll-off in force observed at higher piston velocities may be attributed to increased fluid temperature during testing. As with the carrier fluid, the shear stress is found from the mean steady-state force.

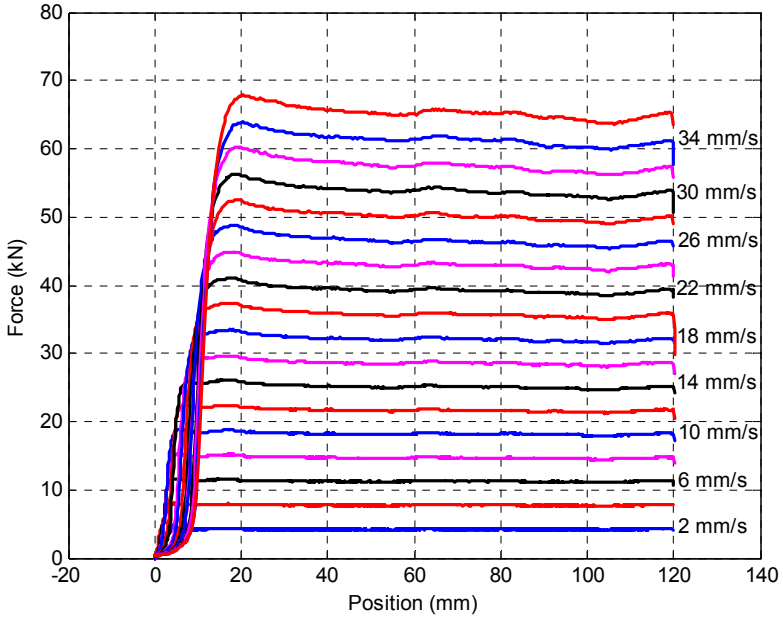

Figure 5-5. Force versus position for MR fluid

Plotting the shear stress versus shear rate, we see that the MR fluid behavior is quite Newtonian. Figure 5-6a shows the shear stress as a function of shear rate. The apparent viscosity, shown in Figure 5-6b, is found at each shear rate. While a moderate shear thinning is observed at lower shear rates, the viscosity seems to reach equilibrium at 0.14 Pa-s. However, close inspection reveals a slight increase in viscosity for higher rates of shear. This behavior is consistent with the behavior observed in the carrier fluid. While the viscosity is quite different in magnitude, the shear thickening behavior may be largely governed by the carrier fluid. Again, as a point of reference, it is noted that these experiments were performed at room temperature. On this particular occasion, the mean fluid initial temperature was 25.8 °C. At this temperature, the mean fluid viscosity is 0.142 Pa-s.

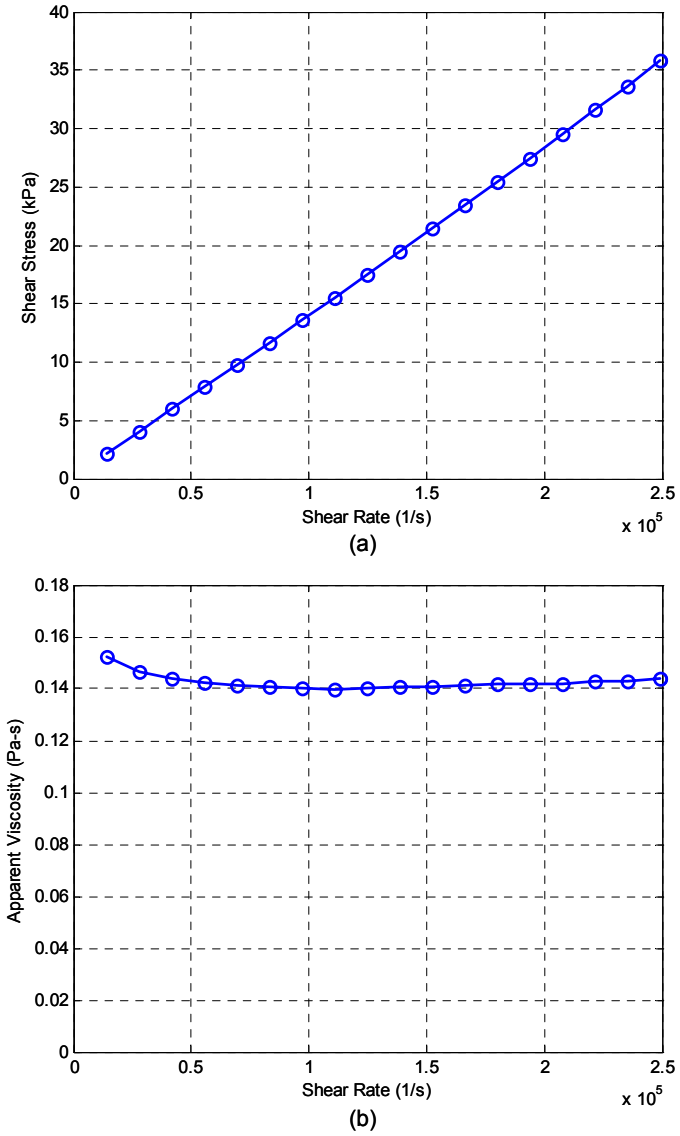

Figure 5-6. MR fluid high shear behavior: (a) shear stress versus shear rate; (b) apparent viscosity versus shear rate (collected at an average initial fluid temperature of 25.8 °C)

5.4 Reynolds number

In order to be thorough, the results presented in Section 5.3 should include a discussion of the Reynolds number. Flowing at high velocities, there may be some concern that the fluid flow is not laminar and that the methods used to determine the shear stress and viscosity are not valid. To assuage this concern, the Reynolds number was calculated for

each fluid at each velocity. In fully developed flow, the critical Reynolds number corresponding to the onset of turbulence is

$$\mathrm{Re}_c \approx 2300 \tag{5-6}$$

Fully turbulent conditions, however, are only achieved at much larger Reynolds numbers $(\mathrm{Re} \approx 10000)$ [69]. The Reynolds number is defined as

$$\mathrm{Re} = \frac{\rho u_m D_h}{\mu} \tag{5-7}$$

where ρ is the fluid density, u_m is the mean fluid velocity through the flow channel, and μ is the viscosity of the fluid. Because our cross section is non-circular, we use the hydraulic diameter, D_h, as the characteristic length. The hydraulic diameter is defined as

$$D_h = \frac{4A_c}{P_w} \tag{5-8}$$

where A_c and P_w are the flow cross-sectional area and the wetted perimeter, respectively. Using the viscosities obtained in Section 5.3, the Reynolds numbers are calculated at each velocity. Fluid densities are summarized in Table 5-3 and the Reynolds numbers for each fluid are shown in Figure 5-7. Reaching a maximum of just over 1200, the Reynolds numbers are well below the critical Reynolds number corresponding to the onset of turbulence. As such, the laminar flow assumption is valid.

Table 5-3. Summary of fluid densities

Fluid	Density (g/cm^3)
Carrier	0.8192
MR	3.060

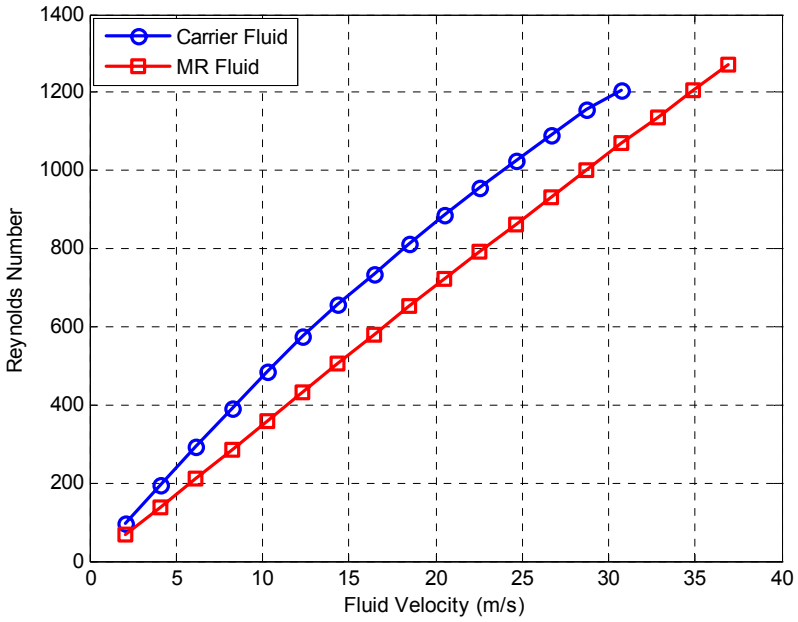

Figure 5-7. Reynolds number for carrier fluid and MR fluid

5.5 Fluid behavior models

In an effort to provide a more thorough representation of the fluid behavior, the experimental data is used to fit a model of the form

$$\tau = a + b\dot{\gamma}^n \tag{5-9}$$

to the shear stress versus shear rate relationships given in Section 5.3. Equation (5-9) is a power law function commonly used to describe non-Newtonian behavior. When $n = 1$, b is simply the normal plastic viscosity. For $n > 1$, the fluid is shear thickening, while for $n < 1$, the fluid is shear thinning. In all cases, a represents a yield stress.

The parameters in the proposed model are estimated from the experimental data. An optimization routine is used to minimize the error between the measured shear stress and the shear stress predicted by the model, according to the objective function

$$J = \sum_{k=1}^{N} \left\{ \tau_p(k) - \tau_{ex}(k) \right\}^2 \tag{5-10}$$

where τ_{ex} is the experimentally determined shear stress, τ_p is the shear stress calculated by the model, and N is the number of experimental measurements made over the range of considered velocities. Figure 5-8 shows the flow chart for the optimization routine. The experimental data is loaded and the shear stress is determined from the measured force. Initial parameters values are chosen for the proposed model. Then using the proposed model, the shear stress is calculated and compared to the experimentally obtained shear stress. The error between the predicted shear stress and the experimental shear stress is minimized using the optimization routine, "fminsearch.m." The output of routine is the value of the objective function as well as the model parameters, a, b, and n, that minimize the error.

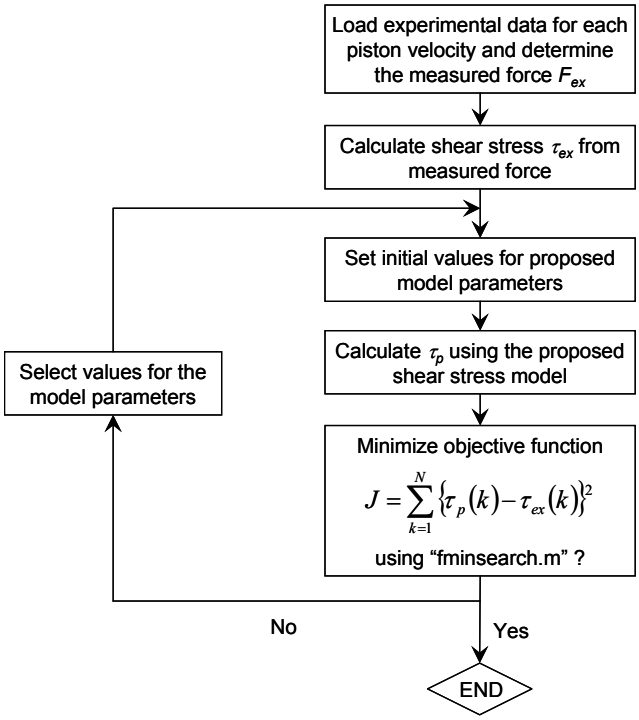

Figure 5-8. Flow chart for optimization routine

5.5.1 Proposed model for carrier fluid

The optimization routine was run using the experimental data for the carrier fluid. The initial model parameters and resulting optimized parameters are summarized in Table

5-4. As a result of the optimization routine, the model for the carrier fluid can be expressed as

$$\tau = 228.5 + 0.0014\dot{\gamma}^{1.26} \tag{5-11}$$

As indicated by the power law coefficient, *n*, the carrier fluid is shear thickening. We also note that the yield stress term, *a*, is non-zero, indicating that the carrier fluid has a yield stress of 228.5 Pa.

Table 5-4. Carrier fluid initial and final model parameters

Parameter	Initial Value	Optimized Value
a	0	228.5
b	0.02	0.0014
n	1	1.260

Figure 5-9a shows the proposed model along with the experimental data. As indicated in Figure 5-9a, the predicted shear stress and the experimentally determined shear stress are in close agreement. As a measure of the accuracy of the proposed model, the error at each shear rate is calculated and shown in Figure 5-9b. With the exception of the first data point, the predicted shear stress is within 5% of the experimental data.

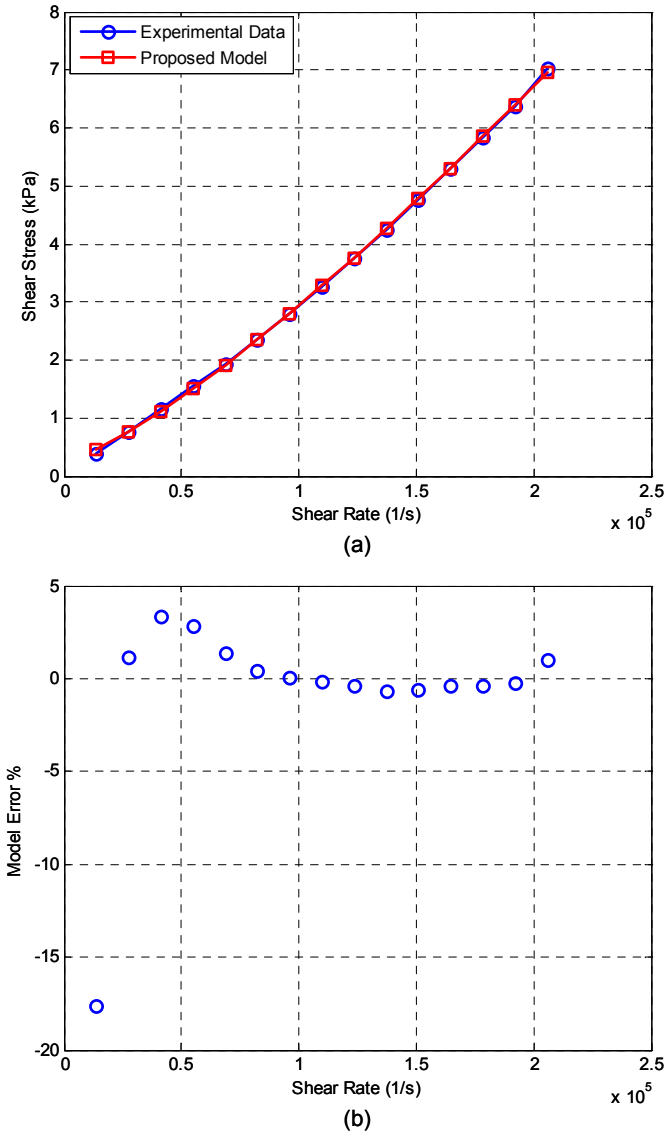

Figure 5-9. Carrier fluid model results: (a) Proposed model and experimental data; (b) model error

5.5.2 Proposed model for MR fluid

The optimization routine was run using the MR fluid data. The initial model parameters and the optimally tuned model parameters are shown in Table 5-5. The resulting model can be expressed by

$$\tau = 579.2 + 0.0727\dot{\gamma}^{1.053} \tag{5-12}$$

The model proposed in equation (5-12) indicates that MR fluid in the absence of a magnetic field is nearly Newtonian in the post-yield state. Once the yield stress of 579.2 Pa is exceeded, the fluid behavior is nearly Newtonian. With a power law coefficient of just 1.053, the fluid exhibits only moderate thickening behavior. This nearly Newtonian post-yield behavior implies that the viscosity of the fluid does indeed approach some asymptote at high shear rates. As mentioned earlier, this asymptote is largely governed by the solids loading, carrier fluid viscosity, and the extent of shear thinning of the suspension agents. The thickening observed in the carrier fluid may serve to oppose the thinning caused by the solids loading and the suspension agents.

Table 5-5. MR fluid initial and final model parameters

Parameter	Initial Value	Optimized Value
a	100	579.2
b	0.02	0.0727
n	1	1.053

The model comparison is shown in Figure 5-10a. Again, there is good agreement between the predicted shear stress and the experimental data. The error at each shear rate is calculated and shown in Figure 5-10b. For the MR fluid model, the error between the predicted shear stress and the experimental data is less than 10%, and in many cases less than 1%.

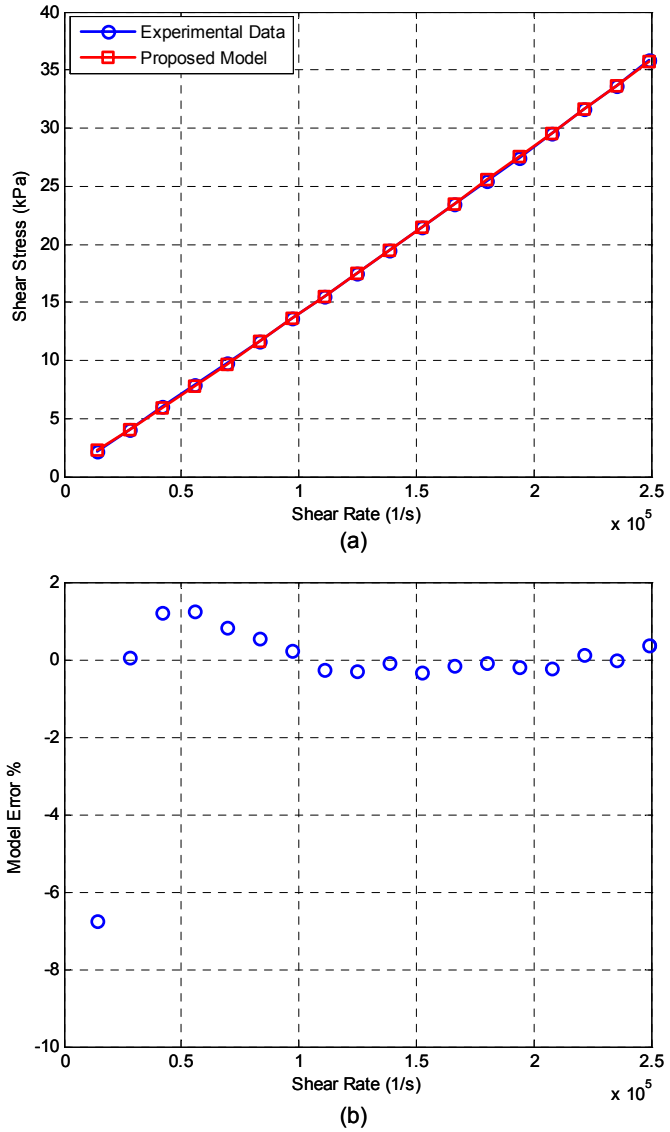

Figure 5-10. MR fluid model results: (a) Proposed model and experimental data; (b) model error

5.6 Temperature considerations

This section discusses the temperature response of the fluid during the experiments and offers some insight into the heat dissipation of the fluid. Because all tests are run in a thermally uncontrolled environment, temperature was recorded in order to provide a reference for the results. To be thorough, the results presented in Section 5.3 should be interpreted with some knowledge of the temperature of the fluid.

Tests were performed at room temperature, though slight fluctuations in room temperature were observed between experiments. In order to document the temperature response of the fluid, a thermocouple was placed at the exit of the rheometer. The temperature response of the carrier fluid is shown in Figure 5-11a. Temperature reaches steady-state after just 10 mm of stroke. For large piston velocities, i.e. 28 mm/s, a temperature rise as large as 4 °C can be observed. In Figure 5-11b we note the increase in steady-state temperature as fluid velocity increases. Furthermore, we note the gradual increase in the initial fluid temperature. This gradual increase in initial fluid temperature can be explained if we consider the rate at which mechanical energy is being dissipated. At a piston velocity of 28 mm/s the corresponding force is 12 kN. The amount of mechanical power that is being dissipated as heat at this piston velocity is nearly 340 Watts. This dissipation will tend to heat up the fluid as well as the rheometer. As such, as testing progressed from low piston velocities to high piston velocities, the initial temperature of the fluid increased slightly.

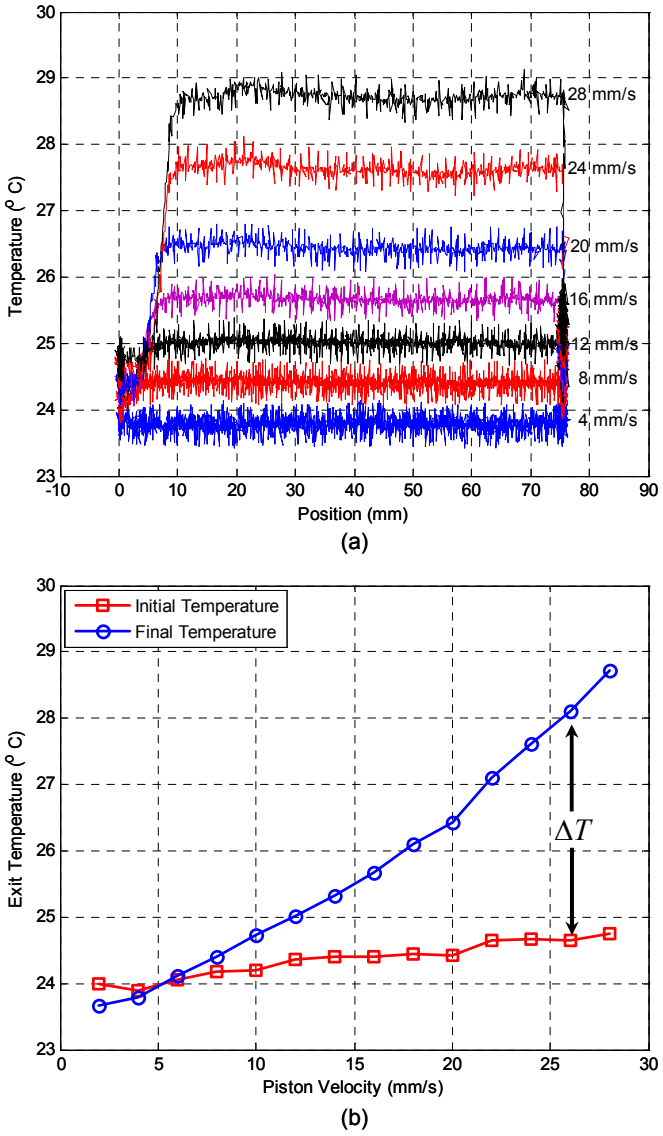

Figure 5-11. Carrier fluid temperature response: (a) fluid exit temperature over piston stroke; (b) fluid initial temperature and final temperature as a function of piston velocity

Similar behavior is observed for the MR fluid. The average initial fluid temperature was 25.8 °C. Figure 5-12a illustrates the temperature response of the MR fluid as it is driven through the rheometer. At a piston velocity of 36 mm/s, a temperature increase of nearly 12 °C is observed. In general, a significantly larger temperature rise is observed for the MR fluid when compared to the carrier fluid. This behavior can be attributed to the difference in fluid densities; the MR fluid's density is 3.06 g/cm^3, while the carrier fluid density is quite lower at 0.8192 g/cm^3. Therefore, the

shear heating observed in the MR fluid is dramatically higher. Nearly 2400 Watts of power are being dissipated at a piston velocity of 36 mm/s. This dissipation tends to heat both the fluid and the rheometer. Figure 5-12b shows the mean temperature increase for each velocity. The initial fluid temperature is also shown. A gradual increase in the initial fluid temperature is observed as the testing progressed from low velocities to high velocities. This increase in initial fluid temperature would likely be accompanied by an increase in the temperature of the steel rheometer.

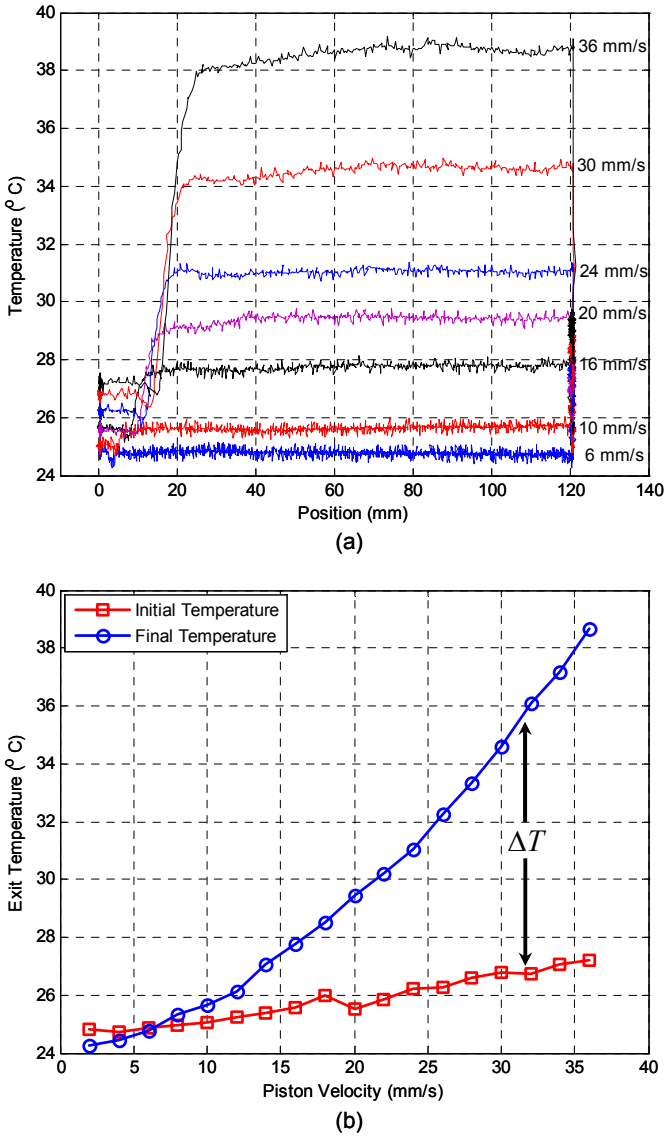

Figure 5-12. MR fluid temperature response: (a) fluid exit temperature over piston stroke; (b) fluid initial temperature and final temperature as a function of piston velocity

5.7 Summary of off-state behavior

The behavior of MR fluid in the absence of a magnetic field has been the focus of this chapter. Equally important as the on-state behavior, the off-state behavior of the fluid is responsible for much of the success attributed to the fluid. Of particular interest in this study was the high shear behavior of the fluid. Because much of the literature has suggested that the high shear behavior is largely governed by the carrier fluid, a characterization of the carrier fluid is also important. Both the carrier fluid and the MR fluid were run through the high shear rheometer. Shear rates ranged from 0.14×10^5 s^{-1} to 2.5×10^5 s^{-1}. Results for the carrier fluid indicate a considerable shear thickening with a power law coefficient of 1.26. The MR fluid exhibited nearly Newtonian post-yield behavior with a power law coefficient of just 1.053. A summary of the proposed models is given in Table 5-6. Among the range of shear rates considered, the carrier fluid and the MR fluid had mean viscosities of 0.03 Pa-s and 0.142 Pa-s, respectively.

Table 5-6. Summary of proposed models

Fluid	Proposed Model
Carrier	$\tau = 228.5 + 0.0014\dot{\gamma}^{1.26}$
MR	$\tau = 579.2 + 0.0727\dot{\gamma}^{1.053}$

6 The MR Effect at High Velocities

Perhaps the most compelling feature of MR fluids is their ability to provide high dynamic yield stresses nearly instantaneously. While the response time of the fluid has yet to be thoroughly investigated, it is known that the fluid can respond to changes in magnetic field strength in a matter of milliseconds. This fluid response can be described as a change in the rheological behavior of the fluid, i.e., the development of a yield stress. The development of a yield stress upon the application of a magnetic field is commonly referred to as the MR effect. The degree of MR effect achieved by the fluid is a function of magnetic field strength. However, because fluid response time is finite, the ability of the fluid to realize the expected MR effect may be compromised if the fluid does not spend a sufficient amount of time in the presence of the magnetic field. We define this time as the dwell time, that is, the amount of time the fluid spends in the presence of a magnetic field.

It is the intent of this chapter to investigate the MR effect under extreme flow conditions. The high velocity rheometer discussed in Chapter 4 is used to study the behavior of the MR fluid at high flow velocities with a magnetic field applied. The magnetic field is applied over a portion of the flow channel. Dwell time is calculated from the length of the MR valve and the fluid velocity through the valve. Two MR valve lengths are considered (25.4 mm and 6.35 mm). Fluid velocities through the valve range from 1 m/s to 37 m/s with corresponding dwell times ranging from 12.4 ms to 0.18 ms. The degree of response achieved by the fluid is studied by calculating the yield stress at each velocity. A significant reduction in the yield stress is observed for dwell times less than 1 ms.

The organization of the chapter begins with a discussion of the MR effect and how it is created in MR devices. A discussion of some of the design considerations for MR valves then follows. Such design considerations include the dwell time of the fluid. After defining the dwell time, the method of experimentally determining the yield stress is introduced. The results from the magnetic field testing are presented and the yield

stress dependence on dwell time is discussed. The chapter concludes with a summary of the MR effect at high flow velocities.

6.1 Creating the MR effect

The MR effect can be described as a measurable change in the rheology of the MR fluid upon the application of a magnetic field. The MR effect results from the polarization induced in the suspended particles by the application of an external magnetic field. Interaction between the polarized dipoles causes the formation of particle chains [8]. These chain-like structures resist and restrict fluid movement. Upon the application of a magnetic field, a yield stress is developed in the fluid. As shown in Figure 6-1, the yield stress increases monotonically for growing magnetic field strengths until the fluid reaches magnetic saturation.

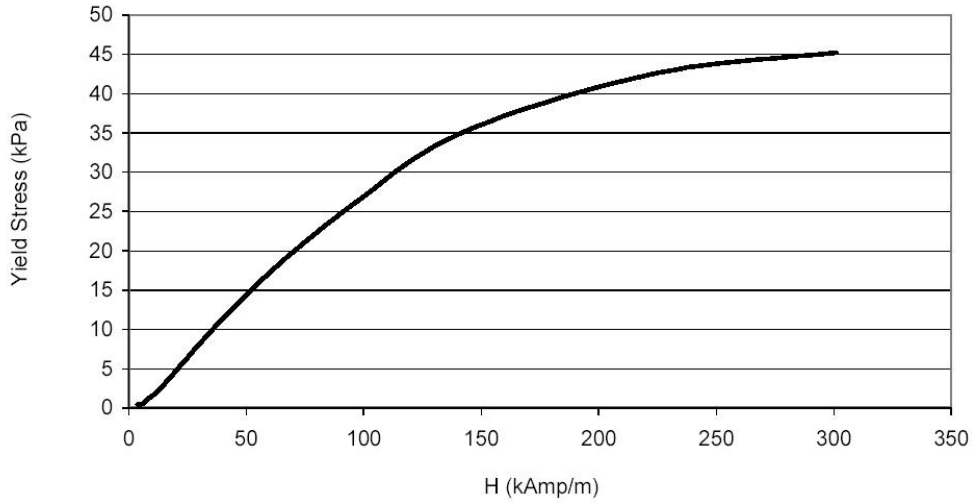

Figure 6-1. Field dependent yield stress for MRF-132LD (© 2005 Lord Corporation [59]. All rights reserved)

Means for creating this change in rheology vary according to application. If we consider, for example, MR devices which operate in valve or shear mode, the yield stress is commonly developed by generating a magnetic field perpendicular to the flow direction. Consider the MR valve shown in Figure 6-2. When designing an MR valve

the flux conduit must be designed such that it directs the focus of the magnetic field to the critical valve region [70]. The use of an electromagnet to create the magnetic field allows for variable field strength and, consequently, controllable yield stress.

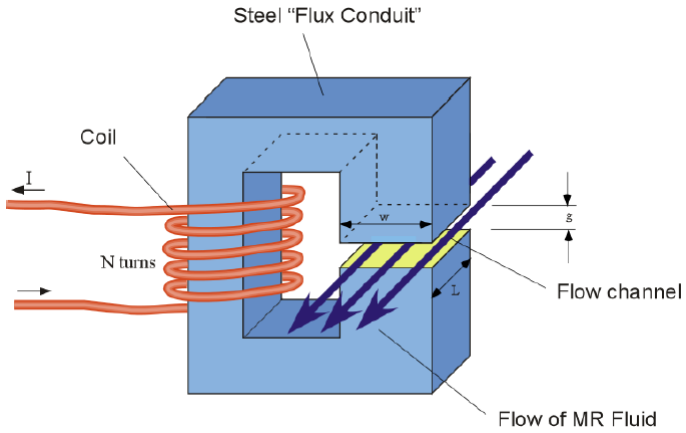

Figure 6-2. Electromagnet-controlled MR valve (© 2005 Lord Corporation [70]. All rights reserved)

In many MR fluid devices, an electromagnet is incorporated into the design to provide the desired controllability. Such is the case for an MR damper; a coil is normally incorporated into the piston as shown in Figure 6-3. A number of alternative valve configurations exist and are well documented in the literature [42, 65, 71-73]. The governing principle, however, is maintained in all embodiments; the fluid is directed through the MR valve and a magnetic field is generated, thus creating the MR effect.

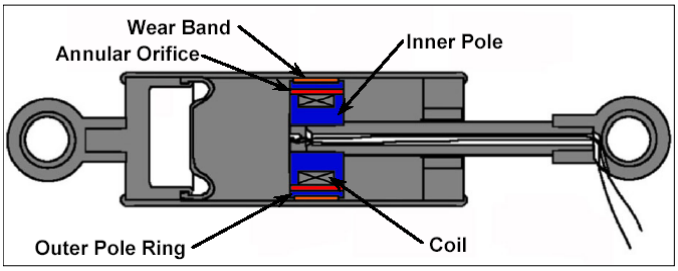

Figure 6-3. Section view of commercial MR fluid damper (image adapted from [8])

6.2 MR valve considerations

In designing an MR valve, the designer must consider many factors in order to develop an effective valve. Some considerations include: gap size, number of turns in coil, wire gauge, current limitations, coil inductance, etc. [64, 73]. Each of these design considerations contribute to the overall performance of the device. Often, this performance is measured by the control ratio or dynamic range of the device. The dynamic range is defined as the ratio of the controllable force, F_τ, to the viscous or uncontrollable force, F_μ [8, 29]. The controllable force, F_τ, is often associated with the maximum on-state force, while the viscous force, F_μ, is normally considered the off-state or minimum force. Designers tailor the design of the valve to achieve the desired dynamic range for the particular device.

Though one might suppose that maximizing the dynamic range would provide the best performance from an MR device, this is often not the case. While achieving a high on-state force is desirable, it is equally important to maintain a low off-state force. There exists a compromise between a high on-state force and a low off-state force. In many real-time control applications, the MR device may operate in the off-state as often as, or more often than, in the on-state. As the off-state force increases, the performance of the MR device in such an application may be compromised. Consider, for example, the application of an MR damper employing the popular "skyhook" or "groundhook" semi-active control policy. The benefits of such control policies can only be realized if the damper can provide sufficiently low off-state forces.

Of the contributing factors to the viscous or uncontrollable force, fluid properties certainly contribute a great deal. The viscosity of the fluid greatly influences the off-state behavior of the MR device. Lord Corporation, the leading supplier of MR fluids, has taken great care in choosing stabilizing additives that do not adversely affect the off-state viscosity of the fluid. Furthermore, the problem of in-use-thickening has been addressed [49]. What remains for the designer of the MR device is to choose the geometry of the device such that the desired dynamic range is met while still maintaining an allowable off-state force.

The means by which a designer can achieve the desired dynamic range and low off-state force are well demonstrated if we consider the design of an MR valve for an MR damper. Recall the MR damper shown in Figure 6-3. The force generated by the MR damper can be separated into two components: the viscous or off-state force, F_μ, and the field induced controllable force, F_{mr}. Using the parallel plate approximation, these forces can be approximated by [29]

$$F_\mu = \left(1 + \frac{whv_o}{2Q}\right)\frac{12\mu Q A_p L}{wh^3} \tag{6-1}$$

$$F_{mr} = c\frac{\tau_o A_p L}{h} \tag{6-2}$$

where L, w, and h are the length, width, and gap of the flow channel, μ is the off-state viscosity, Q is the flow rate, τ_o is the field dependent yield stress, v_o is the pole velocity, and A_p is the area of the piston. The coefficient c is a function of the flow velocity profile and is normally taken to be between 2 and 3 [8]. Equation (6-1) illustrates the dominant effect of the gap size on off-state force. Because the fluid gap is cubed in equation (6-1), the off-state force is highly sensitive to changes in the fluid gap size. The field dependent controllable force is less sensitive to changes in the fluid gap. Because the two forces, F_μ and F_{mr}, are not equally sensitive to changes in gap size, the gap size often becomes a key design element.

The gap size is often chosen to achieve the desired off-state force. A larger gap size will reduce the viscous or uncontrollable force of the damper. As a consequence, however, the maximum on-state or controllable force is also reduced. The designer can then turn to alternative measures for increasing the maximum controllable force. In order to compensate for the larger gap size, MR dampers often employ multi-stage MR valves. Consider the axisymmetric MR valves shown in Figure 6-4. Figure 6-4a shows a single stage MR valve, commonly found in MR dampers such as the MotionMaster™ damper [8]. A single stage MR valve contains a single coil which creates the "choking regions" responsible for the controllable force. With the addition of a second coil, a two-stage MR valve, as shown in Figure 6-4b, has twice the number of choking regions. The coils are alternately-wound such that the magnetic fields are additive and do not cancel each other

[65, 73]. With the additional choking regions, a two-stage valve can provide a greater level of on-state force. Lord Corporation's 180 kN seismic damper [65], shown in Figure 6-4c, employs a 3-stage piston to generate the desired on-state force. Multi-stage pistons allow designers to compensate for larger gap sizes with added controllability from additional activation regions. By increasing the number of activation regions, the active fluid volume increases accordingly. It has been shown that the active fluid volume contributes directly to the dynamic range of the device [8, 52, 71, 72].

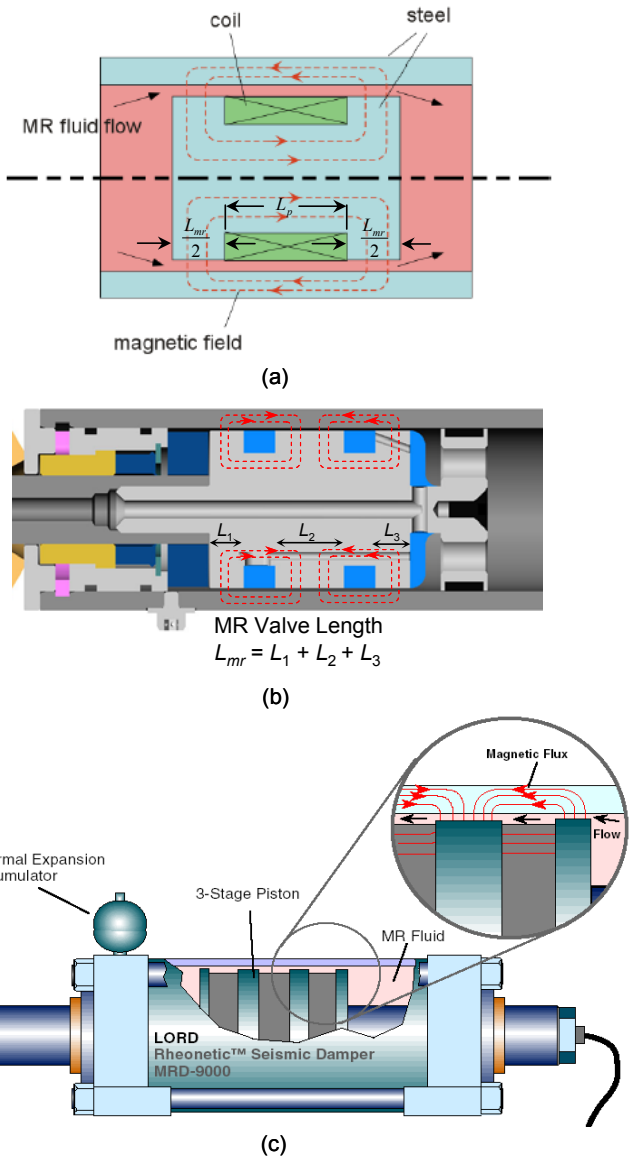

Figure 6-4. Axisymmetric MR valves: (a) single-stage piston (image adapted from [70]); (b) dual-stage piston (image adapted from [73]); (c) 3-stage piston (© 2005 Lord Corporation [4]. All rights reserved)

From the MR valve configurations shown in Figure 6-4, we can identify passive and active portions of the MR valve. As shown in Figure 6-4a, the entire valve length is not activated; the portion of the valve which contains the coil is inactive. We define the active valve length as the portion of the MR valve which acts upon the MR fluid. The active length, or magnetic pole length, of the piston shown in Figure 6-4b, for example, is 3.3 cm out of a total piston length of 4.0 cm [73]. Likewise, for the 3-stage piston in Figure 6-4c, the effective pole length is 8.4 cm, with a total piston length of 22.4 cm [29, 65]. This portion of the MR valve is responsible for the rheological change in the fluid, i.e., the MR effect. The active length of the MR valve becomes a matter of significant importance in applications in which the fluid is operating under extreme flow conditions.

6.3 Fluid dwell time

As the fluid flows through the MR valve, it is subjected to a magnetic field in the active valve regions. Over this portion of MR valve, the fluid develops its yield stress and allows for controllability in the force. As the fluid enters the active valve region, the transition from Newtonian-like flow to Bingham plastic flow occurs. Though it is known that MR fluid response to a magnetic field occurs in a matter of milliseconds [2, 3], the degree of response achieved by the fluid has yet to be addressed.

We confront this issue by first defining the fluid dwell time, also referred to as residence time as described in the work by Bullough et al. [74]. Dwell time is defined as the amount of time the fluid spends in the presence of a magnetic field. In other words, dwell time is the time it takes the fluid to flow through the MR valve. Dwell time is calculated from

$$t_{dwell} = \frac{L_{mr}}{u_m} \tag{6-3}$$

where L_{mr} is the length of the MR valve and u_m is the mean fluid velocity through the flow channel. Consider, as an example, an extreme case in which the fluid is stationary in an active region of an MR valve. In such a case, the fluid will develop its full potential, or 100% of its expected yield stress with the application of a magnetic field.

On the other hand, when the fluid is flowing through an MR valve, the time spent in the active region may influence the degree of response achieved by the fluid. The flow schematic shown in Figure 6-5 illustrates an exaggerated transition from Newtonian-like to Bingham plastic flow. In the absence of a magnetic field, the fluid exhibits Newtonian-like behavior; particle orientation is random and the velocity profile is parabolic. When the fluid reaches Section I, it is exposed to a magnetic field. The transition from Newtonian-like behavior to Bingham plastic behavior begins at Section I. When the fluid reaches Section II the particles have begun to align along the flux path. At this stage the yield stress is not yet fully developed, perhaps only reaching 70% of full potential. Only once the fluid reaches Section III has the yield stress reached 100% of the expected value. In the schematic, the dwell time exceeds the response time and the fluid can achieve its full potential. However, as the fluid velocity increases, the dwell time decreases. Should this dwell time decrease below the time required to achieve the full yield stress, the fluid may only achieve a portion of the expected yield stress. For example, if the active valve length were only half of that shown in Figure 6-5, the fluid would reach Section II and exit the valve only achieving 70% of full potential.

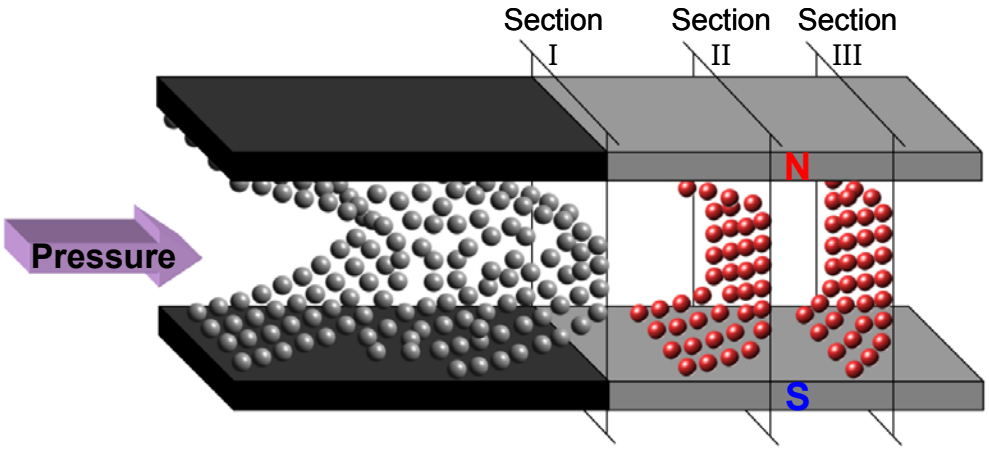

Figure 6-5. MR valve flow schematic illustrating fluid response to a magnetic field

The behavior depicted in Figure 6-5 was experimentally investigated using the slit-flow rheometer. Two active valve lengths were considered (25.4 mm and 6.35 mm).

Fluid velocities ranged from 1 m/s to 37 m/s with corresponding dwell times ranging from 12.4 ms to 0.18 ms. Figure 6-6 shows the dwell time as a function of fluid velocity for each valve length. With the 25.4 mm valve length, dwell times were between 12.4 ms and 0.69 ms, while for the 6.35 mm valve length, dwell times dropped to between 6.4 ms and 0.18 ms. For the 6.35 mm valve length, the piston velocities were chosen such that there was a large concentration of dwell times close to 1 ms. This was done in order to highlight the response of the fluid at dwell times close to 1 ms. The yield stress was found from the measured force for each fluid velocity and evaluated as a function of the dwell time.

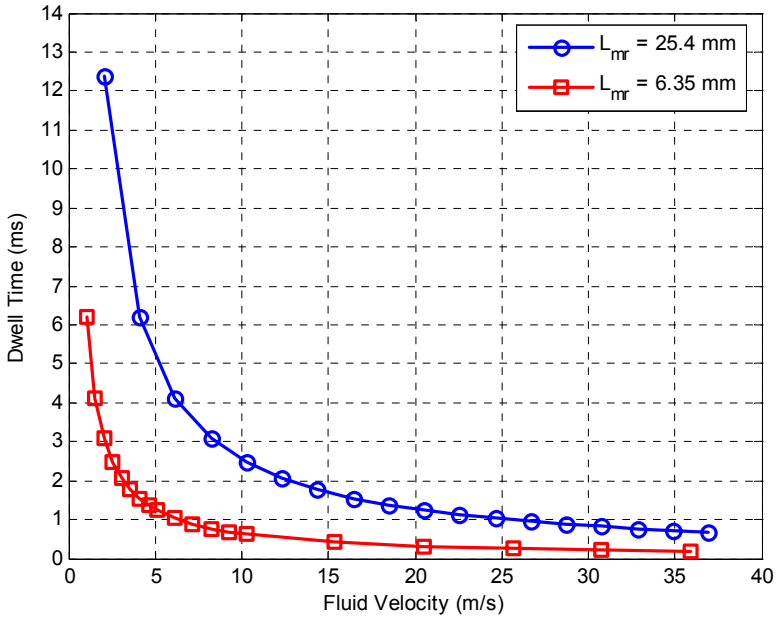

Figure 6-6. Dwell time of fluid through active valve length

6.4 Experimental determination of the yield stress

Recall from the description of the rheometer in Chapter 4 that the flow channel was given as 101.6 mm with the MR valve incorporated into the last 25.4 mm of the channel. Figure 6-7 shows the flow channel with the 25.4 mm MR valve. The magnetic field was applied to the active MR valve portion only. When testing with the 6.35 mm MR valve,

it was important to maintain total flow channel length. To this end, a 19.04 mm stainless steel blank was used to make up the additional length.

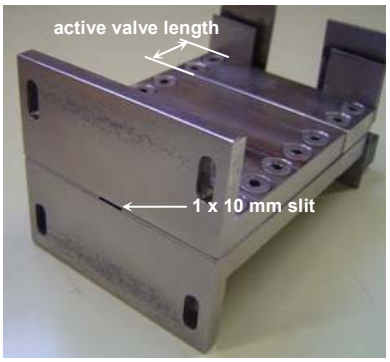

Figure 6-7. Flow channel showing MR active valve portion

In order to determine the yield stress from the measured force, we must first identify the factors contributing to the measured force. The dominant forces are created in the flow channel. As such, we consider the Poiseuille flow shown in Figure 6-8. Two distinct regimes contribute to the pressure gradient developed in the channel. The first is between sections 1 and 2 which represents the Newtonian-like behavior of the MR fluid in the absence of a magnetic field. Between sections 2 and 3 is where the fluid is being energized by a magnetic field. In this regime three regions can be identified by the Bingham plastic behavior of the fluid. In regions I and II, where the shear rate is large, the fluid exhibits Newtonian-like behavior. In region III, however, the fluid is moving as a solid or plug through the channel. In this region, the yield stress has not been exceeded and thus the fluid is not being sheared. Recall that τ_o is the yield stress which must be exceeded in order to initiate flow.

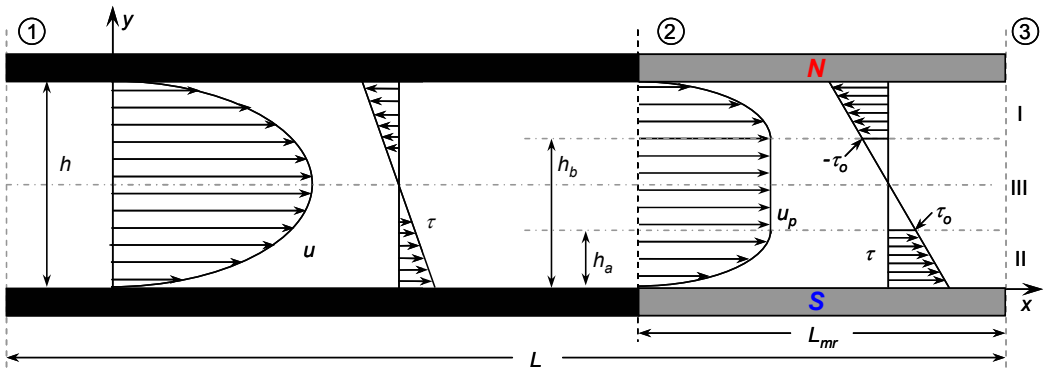

Figure 6-8. Flow transition through fixed parallel plates

From the pressure gradient derivation developed in Chapter 3, the pressure in the flow channel can be written as the sum of the pressure developed in the Newtonian regime and pressure developed in the non-Newtonian regime, i.e. the MR valve. The force generated in the flow channel is simply the combined pressure of the Newtonian regime, P_μ, and the Bingham regime, P_{mr}, acting over the area of the piston, A_p.

$$F = A_p\left(\Delta P_\mu + \Delta P_{mr}\right) \tag{6-4}$$

where

$$\Delta P_\mu = \frac{12u_m\mu}{h^2}\left(L - L_{mr}\right) \tag{6-5}$$

and

$$\Delta P_{mr} = \frac{12\mathcal{P}u_m\mu}{h^2}L_{mr} \tag{6-6}$$

In equation (6-5) and equation (6-6), u_m is the mean fluid velocity through the channel, μ is the fluid viscosity, and h is the gap size. L and L_{mr} are the lengths of the flow channel and the length of the MR valve, respectively. $\mathcal{P}$ is the non-dimensional pressure drop introduced in Chapter 3. Because force is a measured quantity, we can solve equation (6-4) for the pressure developed in the MR valve

$$\Delta P_{mr} = \frac{F}{A_p} - \Delta P_\mu \tag{6-6}$$

Substituting equation (6-5) and equation (6-6) into equation (6-7), we have an expression for the non-dimensional pressure gradient in terms of the measured force

$$\mathcal{P} = \frac{F}{A_p}\frac{h^2}{12u_m\mu L_{mr}} - \frac{L - L_{mr}}{L_{mr}} \tag{6-8}$$

Recall the cubic equation presented in Chapter 3, repeated here for convenience,

$$\mathcal{P}^3 - (1 + 3\mathcal{T})\mathcal{P}^2 + 4\mathcal{T}^3 = 0 \tag{6-9}$$

where $\mathcal{P}$ and $\mathcal{T}$ are given by

$$\mathcal{P} = -\frac{dp}{dx}\frac{h^2}{12u_m\mu} \tag{6-10}$$

$$\mathcal{T} = \frac{\tau_o h}{12u_m\mu} \tag{6-11}$$

In equation (6-10), dp/dx is the pressure gradient developed along the MR valve length, and τ_o in equation (6-11) is the yield stress. Because $\mathcal{P}$ is known from equation (6-8), the equation of interest becomes the cubic in $\mathcal{T}$

$$\mathcal{T}^3 - \frac{3}{4}\mathcal{P}^2\mathcal{T} + \frac{1}{4}\left(\mathcal{P}^3 - \mathcal{P}^2\right) = 0 \tag{6-12}$$

Rewriting equation (6-9) in this form, we can solve for the roots of $\mathcal{T}$ in terms of $\mathcal{P}$, where $\mathcal{P}$ is found from the measured force. The desired root is given by [56]

$$\mathcal{T}(\mathcal{P}) = \mathcal{P}\cos\left(\frac{1}{3}\operatorname{acos}\left(\frac{1-\mathcal{P}}{\mathcal{P}}\right) + \frac{4\pi}{3}\right) \tag{6-13}$$

The yield stress is then found from equation (6-11) as

$$\tau_o = \frac{12u_m\mu}{h}\mathcal{T} \tag{6-14}$$

It should be noted that the viscosity used in the calculation of the yield stress was determined from the off-state viscosity discussed in Chapter 5. The shear-thinning behavior has been accounted for in the yield stress calculations. Furthermore, by using

the viscosity obtained in experiments, any variation in temperature that may have existed between experiments was accounted for.

6.5 Magnetic field testing

The yield stress was found for a number of magnetic field strengths and two active MR valve lengths. The 25.4 mm valve length was activated with field strengths of 100 kA/m and 200 kA/m at 18 piston velocities ranging from 2 mm/s to 36 mm/s. Piston velocities increased at an increment of 2 mm/s. Experiments with the 6.35 mm valve length were performed at three magnetic field strengths (100 kA/m, 150 kA/m, and 200 kA/m). Piston velocities for the 6.35 mm valve ranged from 1 mm/s to 35 mm/s. At this valve length, 10 piston velocities were tested between 1 mm/s and 5 mm/s, and another 5 velocities between 6 mm/s and 10 mm/s. This was done in order to highlight the response of the fluid at dwell times close to 1 ms. Above piston velocities of 10 mm/s, the velocity increment increased to 5 mm/s.

Figure 6-9 shows the force versus position for several piston velocities at magnetic field strengths of 100 kA/m and 200 kA/m for both valve lengths. In Figure 6-9 we note a marked increase in force for the 25.4 mm valve length as the magnetic field increases from 100 kA/m, Figure 6-9a, to 200 kA/m, Figure 6-9b. The same cannot be said for the 6.35 mm valve. For large piston velocities the increase in magnetic field from 100 kA/m, Figure 6-9c, to 200 kA/m, Figure 6-9d, results in only a marginal increase in force. At low piston velocities, however, there is a noticeable increase in force for the 6.35 mm valve. We also note, in comparing the forces for each valve length, that for similar velocities the force achieved with the 6.35 mm active valve length is significantly less than the force achieved with the 25.4 mm valve length. This is expected since the active valve length for the 6.35 mm valve is $1/4^{th}$ of the 25.4 mm valve. As such, the yield stress is being developed over a shorter portion of the flow channel. These results are better illustrated if we consider the force, or pressure, as a function of fluid velocity.

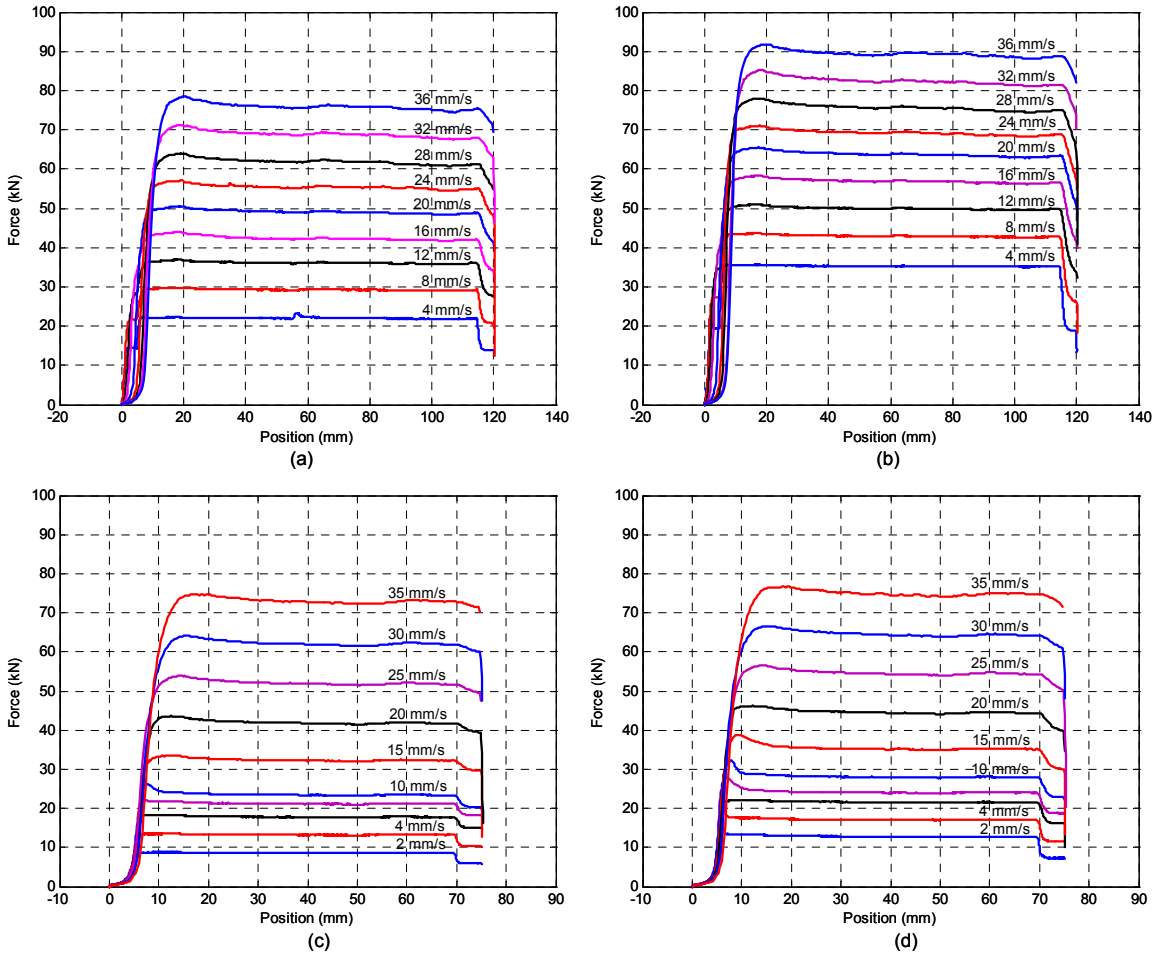

Figure 6-9. Force versus position: (a) 25.4 mm valve at 100 kA/m; (b) 25.4 mm valve at 200 kA/m; (c) 6.35 mm valve at 100 kA/m; (d) 6.35 mm valve at 200 kA/m

The mean value of the force was found once the force had reached steady-state. From the mean steady-state force, the pressure drop in the flow channel is found from equation (6-4). Figure 6-10 shows the pressure for each field strength and each valve length as a function of fluid velocity. The zero-field pressure is also included. For the 25.4 mm valve length, Figure 6-10a, there is a substantial increase in the pressure developed in the channel as the magnetic field increases from 100 kA/m to 200 kA/m. Furthermore, the separation between curves is maintained as fluid velocity increases. This is not the case for the 6.35 mm valve as shown in Figure 6-10b. The change in pressure measured for the 6.35 mm valve as magnetic field increases from 100 kA/m to 200 kA/m is marginal when compared to the 25.4 mm valve. This result, however, is

expected due to the dramatic reduction in the active valve length. The significance of the result shown in Figure 6-10b is the behavior observed as the fluid velocity increases. For low fluid velocities the pressure differential between field strengths is maintained. However, as the fluid velocity continues to grow the pressure differential decreases; pressures for the 100 kA/m, 150 kA/m, and 200 kA/m tests appear to converge towards the zero-field case. This implies that, with the 6.35 mm active valve length, the yield stress being developed in the fluid is not being maintained as fluid velocity increases.

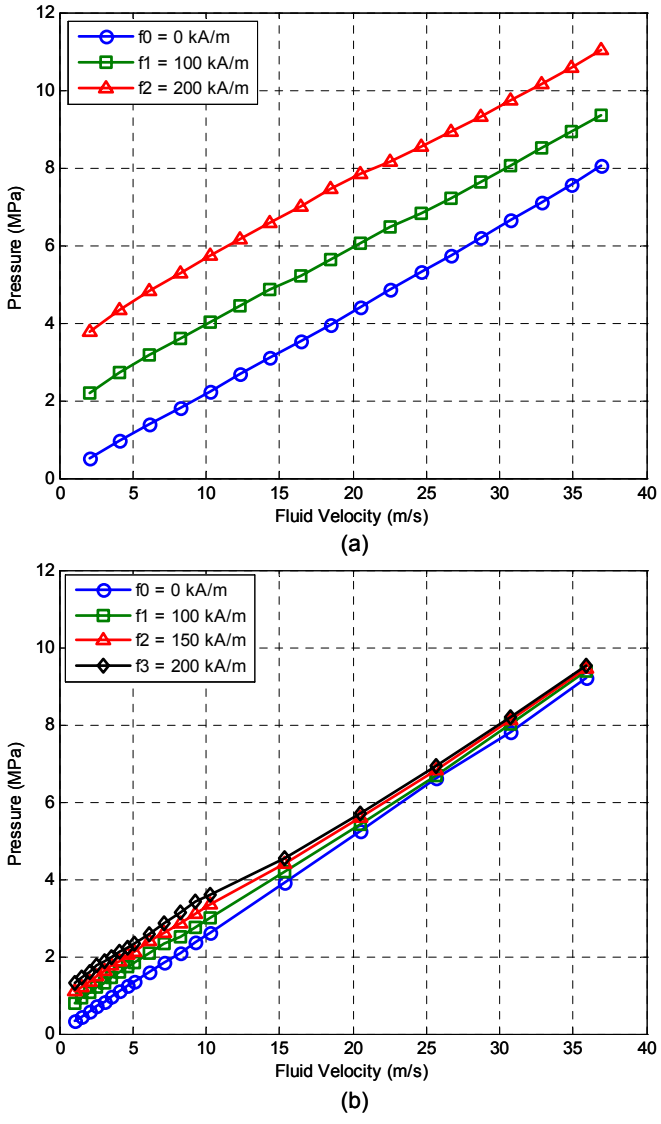

Figure 6-10. Pressure in flow channel as a function of fluid velocity: (a) 25.4 mm valve; (b) 6.35 mm valve

We next consider the yield stress being developed at each velocity for each active valve length. From the total pressure shown in Figure 6-10, the non-dimensional pressure, $\mathcal{P}$, developed in the MR valve can be extracted from equation (6-8). The non-dimensional yield stress, $\mathcal{T}$, is then found from equation (6-13). With the non-dimensional yield stress known, the yield stress is found from equation (6-14). Figure 6-11 shows the experimentally determined yield stress for both MR valve lengths at each magnetic field strength. For the 25.4 mm MR valve, Figure 6-11a, a slight reduction in yield stress is observed as fluid velocity increases. Figure 6-11b shows the results for the 6.35 mm valve. With this valve configuration, a significant reduction in yield stress is observed as fluid velocity increases. The results in Figure 6-11b indicate that the yield stress at low velocities is nearly maintained. However, as the fluid velocity continues to increase, the yield stress falls off rather sharply. We also note that the differential between the yield stresses developed at low velocities for each magnetic field strength are significantly larger than those observed at high velocities. In other words, at high velocities, there is little change in the yield stress for varying magnetic field strengths. Though these results indicate some dependence on fluid velocity, the reduction in yield stress observed with both MR valves is more closely related to dwell time rather than fluid velocity.

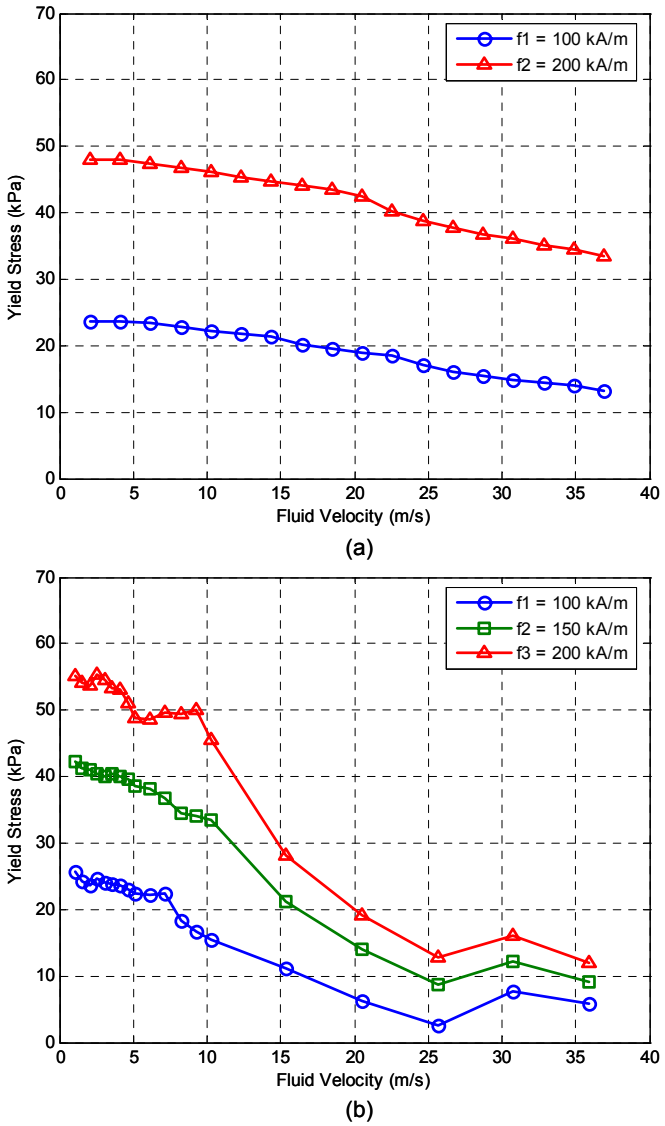

Figure 6-11. Yield stress as a function of fluid velocity: (a) 25.4 mm MR valve; (b) 6.35 mm MR valve

6.6 Yield stress dependence on dwell time

Recall that the dwell time is the amount of time the fluid spends in the presence of a magnetic field. Dwell time is calculated by dividing the length of the MR valve by the fluid velocity in the flow channel. Dwell times for the 25.4 mm valve ranged from 12.4 ms to 0.68 ms, while for the 6.35 mm valve, dwell times ranged from 6.2 ms to 0.18 ms. Figure 6-12 shows the relationship between the yield stress developed in the MR valve and the dwell time. For the 25.4 mm valve length, Figure 6-12a, the yield stress remains

relatively constant for dwell times greater than 2 ms. As the dwell time approaches 1 ms, however, we observe a roll-off in the yield stress. Similar results are observed for the 6.35 mm valve length, Figure 6-12b. For dwell times greater than 1 ms, the yield stress is relatively constant. Much like the 25.4 mm case, however, as the dwell time falls below 1 ms, the apparent yield stress drops considerably. The results for the 6.35 mm valve length clearly indicate that if the dwell time drops below 1 ms the fluid is unable to achieve full potential. Figure 6-12b indicates that with a dwell time of 0.5 ms the yield stress developed in the gap is significantly less than the expected yield stress for a given magnetic field strength.

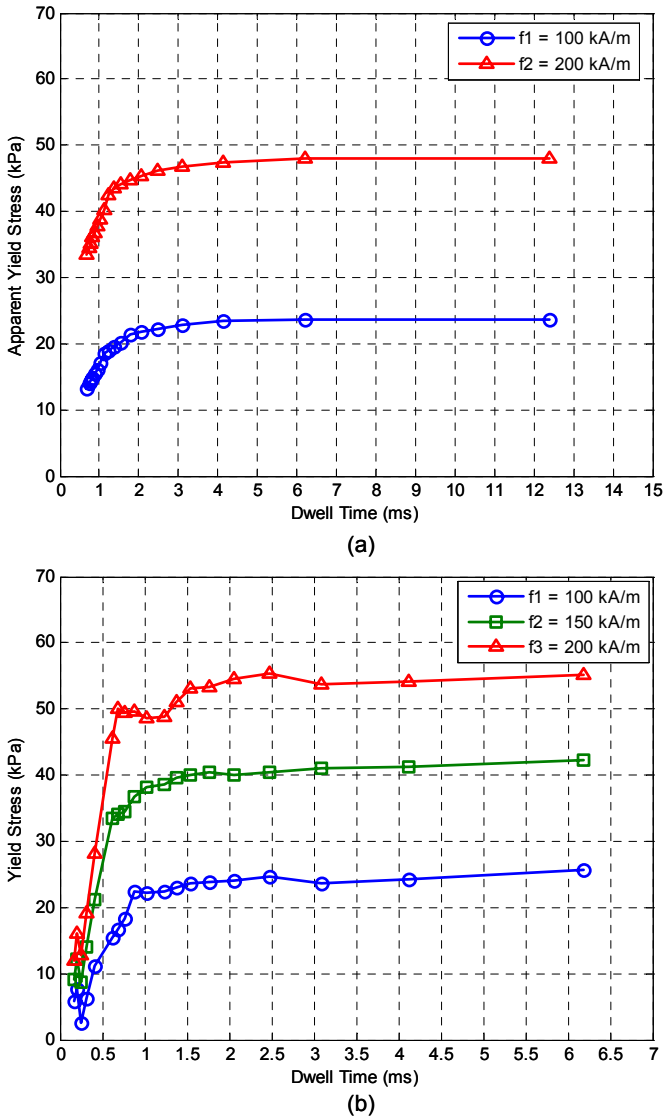

Figure 6-12. Yield stress as a function of dwell time: (a) 25.4 mm MR valve; (b) 6.35 mm MR valve

As a measure of the degree of response achieved by the fluid, we normalize the yield stress with respect to the maximum yield stress observed for each field strength as

$$\Psi = \frac{\tau_o}{\max(\tau_o)} \tag{6-15}$$

Figure 6-13 shows the normalized yield stress as a function of dwell time. In this representation, we observe that for the 25.4 mm MR valve, Figure 6-13a, the fluid is still able to achieve greater than 50% of the maximum yield stress for dwell times as low as 0.68 ms. As the dwell time decreases further below 1 ms, however, as in the 6.35 mm valve length, Figure 6-13b shows that the yield stress is reduced to as little as 10% of the maximum value.

The results in Figure 6-13 also indicate that a higher magnetic field can "delay" the reduction of the yield stress. Figure 6-13a shows that the yield stress for the 100 kA/m magnetic field strength begins to falls sooner than the 200 kA/m field strength. The normalized yield stress is consistently higher for the 200 kA/m field strength than for the 100 kA/m field strength. If we consider, for example, the value of the normalized yield stress at 0.68 ms, we see that the 200 kA/m field strength is achieving 70% of the maximum value while the 100 kA/m field strength has already fallen to 55%. The same can be said for the 6.35 mm valve length. From Figure 6-13b, we see that the normalized yield stress for the 100 kA/m field strength drops sooner and more dramatically than the other two magnetic field strengths.

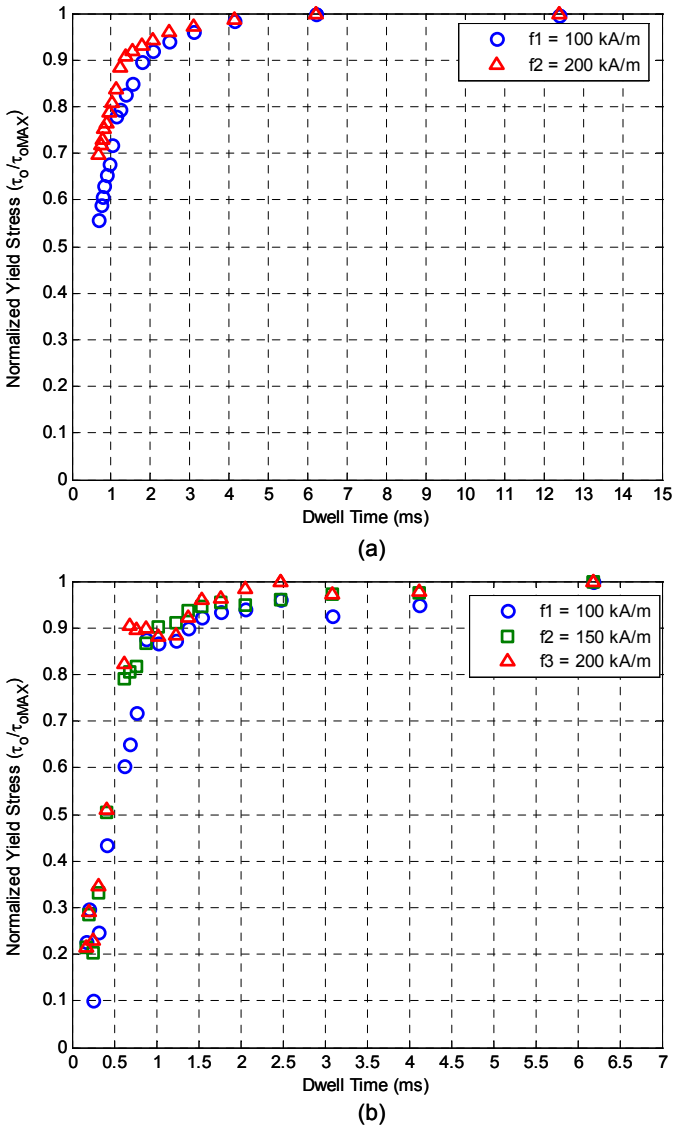

Figure 6-13. Normalized yield stress as a function of dwell time: (a) 25.4 mm MR valve; (b) 6.35 mm MR valve

6.7 Modeling the MR effect at high velocities

As a characterization of the MR effect at high velocities, a model based on the experimental results is proposed. Thus far, the results indicate that the normalized yield stress is predominantly a function of dwell time. However, as observed in Figure 6-13, the normalized yield stress is also a function of the magnetic field strength. Consider Figure 6-14, in which we further generalize the yield stress results, and present the

normalized yield stress as a function of just the magnetic field strength and the dwell time. Figure 6-14 combines the results presented in Figure 6-13 and makes a distinction only with regard to magnetic field strength, and not valve length. In this form, the results further demonstrate the effect of field strength on fluid response. For the 200 kA/m field strength, the reduction in yield stress is delayed. This indicates that a larger magnetic field strength can delay the reduction in yield stress for falling dwell times. The implication here is that the fluid response time is a function of magnetic field strength.

Though the form of the proposed model has not yet been introduced, from the experimental data shown in Figure 6-14, the proposed model can be assumed to be a function of both dwell time and magnetic field strength. The predicted value of the normalize yield stress, Ψ_p, can be expressed in general form as

$$\Psi_p = \Psi_p\left(t_{dwell}, H\right) \tag{6-16}$$

where t_{dwell} is the dwell time and H is the magnetic field strength. In what follows, the model in equation (6-16) will be developed explicitly as a function of the dwell time. However, because the current study does not include sufficient data for the magnetic field strength, the proposed model can not be expressed in general form as a function of the field strength. For this reason, two independent models are proposed, one for each magnetic field strength.

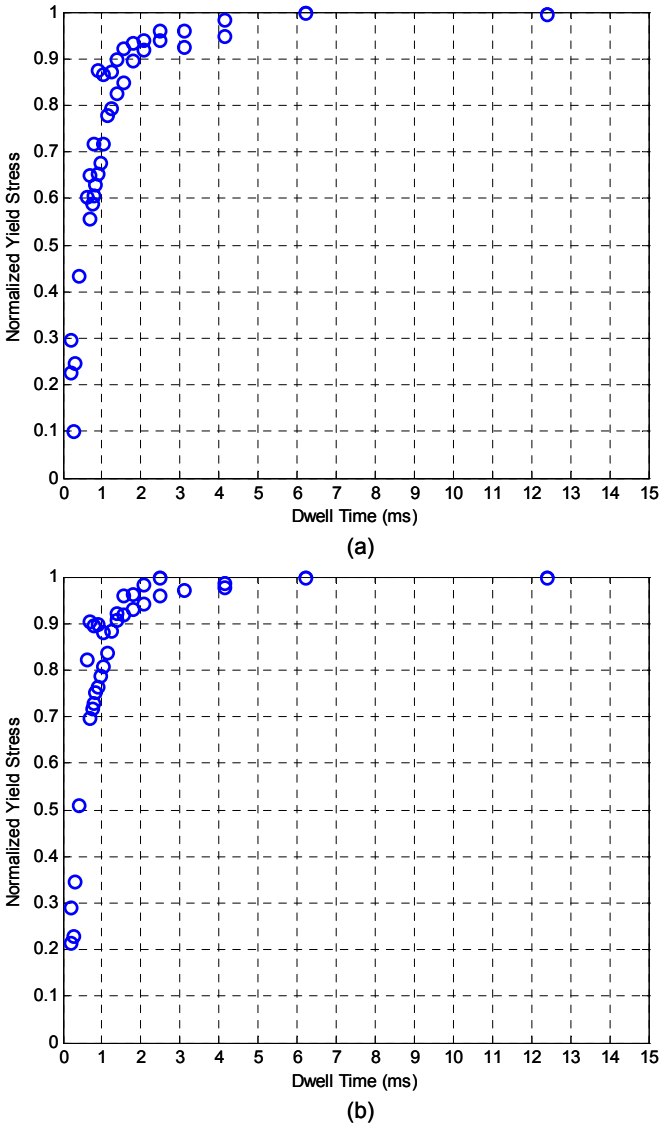

Figure 6-14. Normalized yield stress as a function of dwell time: (a) 100 kA/m; (b) 200 kA/m

A number of shape functions were considered to describe the behavior in Figure 6-14. The parameters in each of the considered models are estimated from the experimental data. As in Chapter 5, an optimization routine is used to minimize the error between the measured data and values predicted by the models, according to the objective function

$$J = \sum_{k=1}^{N} \left\{ \Psi_p(k) - \Psi_{ex}(k) \right\}^2 \tag{6-17}$$

where Ψ_{ex} is the normalized yield stress obtained from experimental data, and Ψ_p is the normalized yield stress predicted by the model.

The quality of each model was evaluated with regard to the magnitude of the minimized objective function. Table 6-1 summarizes some of the considered models along with their tuned parameters for each magnetic field strength. As a measure of the quality of the model, the value of the objective function is also shown.

Table 6-1. Summary of proposed MR effect models

Proposed Model		Model Parameters						*J*	
		c_1		c_2		c_3		100 kA/m	200 kA/m
		100 kA/m	200 kA/m	100 kA/m	200 kA/m	100 kA/m	200 kA/m		
M1	$\Psi_p = \tanh(c_1 \cdot t_{dwell})$	0.9987	1.3238	-	-	-	-	0.1297	0.1257
M2	$\Psi_p = 1 - e^{-c_1 \cdot t_{dwell}}$	1.3598	1.8476	-	-	-	-	0.1305	0.1299
M3	$\Psi_p = (1 - e^{-c_1 \cdot t_{dwell}}) \cdot \tanh(c_2 \cdot t_{dwell})$	1.3921	1.9562	4.4965	4.2562	-	-	0.1249	0.1057
M4	$\Psi_p = (1 - c_1 \cdot e^{-t_{dwell}}) \cdot \tanh(c_2 \cdot t_{dwell})$	0.4970	0.2942	1.6482	1.8875	-	-	0.1162	0.1052
M5	$\Psi_p = (1 - c_1 \cdot e^{-c_2 \cdot t_{dwell}}) \cdot \tanh(c_3 \cdot t_{dwell})$	0.0984	0.7121	0.3085	1.6270	1.1468	2.8114	0.1139	0.1012

From Table 6-1, we see that model M5 has the smallest combined objective function value. This implies that model M5 provides the best fit to the experimental data. Figure 6-15 shows the comparison between model M5 and the experimental data for each field strength. The resulting models for each field strength can be expressed as

$$\Psi_p(t_{dwell},100) = (1 - 0.0984 \cdot e^{-0.3085 \cdot t_{dwell}}) \cdot \tanh(1.1468 \cdot t_{dwell}) \tag{6-18}$$

$$\Psi_p(t_{dwell},200) = (1 - 0.7121 \cdot e^{-1.6270 \cdot t_{dwell}}) \cdot \tanh(2.8114 \cdot t_{dwell}) \tag{6-19}$$

The dependence on the field strength in the proposed models is embedded in the model parameters, c_1, c_2, and c_3. In order to express the proposed model in general form as a function of H and t_{dwell}, as given in equation (6-16), results must be generated for several more magnetic field strengths. This, however, is beyond the scope of the current study.

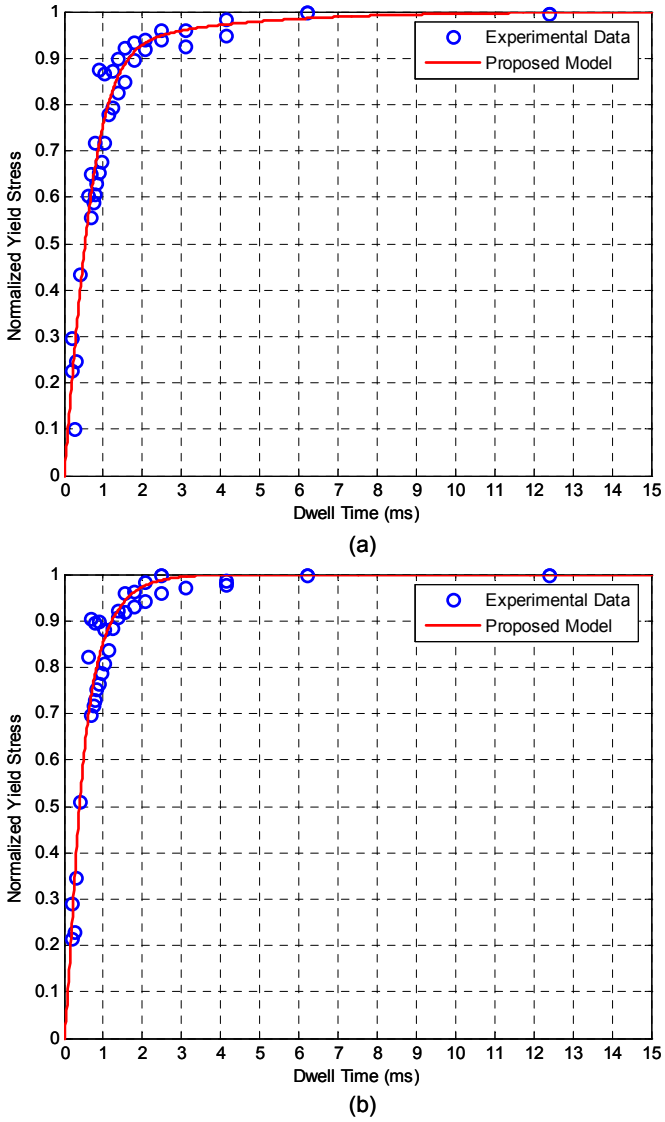

Figure 6-15. Proposed MR effect model comparison: (a) 100 kA/m; (b) 200 kA/m

6.8 MR fluid response time

Though it is known that the response time of MR fluid is less than 1 ms, the degree of response has yet to be addressed. With a model for the normalized yield stress, we can quantify the response time of the fluid with respect to the dwell time. We first define the response time as the time required for the fluid to achieve 63.2% of the expected value of the yield stress. Then, we identify the relationship between dwell time and response time. This relationship is well illustrated if we consider an example. Assume the

response time of the fluid is 0.5 ms. Then, if the dwell time is greater than the response time, the fluid will achieve greater than 63.2% of the expected yield stress. Otherwise, the fluid will achieve less than 63.2% of the expected yield stress. From the models for the normalized yield stress, we can identify the dwell time that corresponds to a normalized yield stress of 0.632. This dwell time is the response time of the fluid.

The response time of the fluid for each magnetic field strength is identified in Figure 6-16. With this scale, it is clear that magnetic field strength has a significant effect on the normalized yield stress. The response times are identified graphically in Figure 6-16 and summarized for each magnetic field strength in Table 6-2. As illustrated in Figure 6-16, the response time decreases as magnetic field increases. This behavior may be attributed to particle interaction within the fluid. A study by Ginder [75] suggests that the pair-formation time is a function of field strength. Pair-formation is the alignment of adjacent particles along magnetic flux paths. As the field is increased, the pair-formation time decreases. The relationship suggested by Ginder is supported by the results shown in Figure 6-16.

Table 6-2. Summary of response time results

Magnetic Field Strength (kA/m)	Response Time (ms)
100	0.7325
200	0.5303

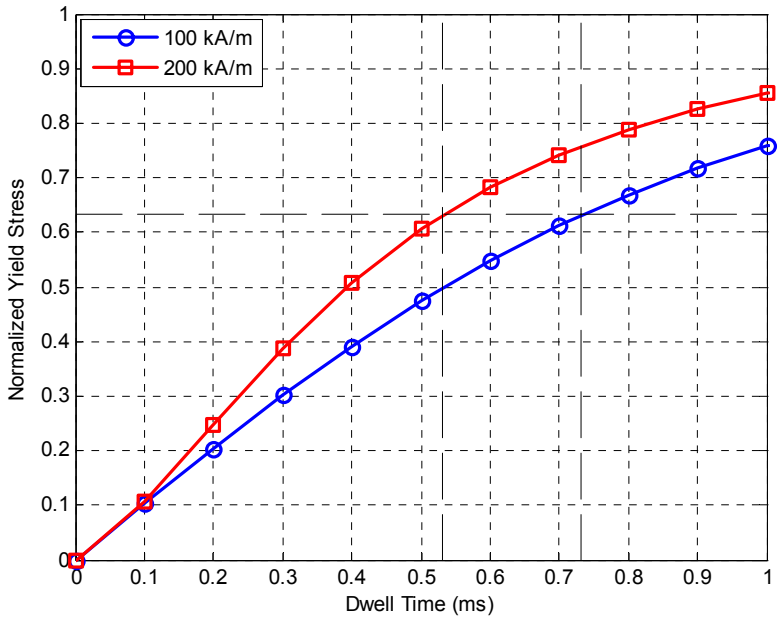

Figure 6-16. Identifying the response time of MR fluid at 100 kA/m and 200 kA/m

6.9 Summary of MR effect at high velocities

The high velocity behavior of MR fluid subjected to a magnetic field was evaluated. Two active valve lengths were considered. Fluid dwell time was found for each valve length and fluid velocity. Experimental results indicate a strong correlation between dwell time and the yield stress developed in the MR valve. For the 6.35 mm valve length the controllability of the valve was dramatically reduced as velocity increased. This implies that smaller valve lengths can lead to severely reduced controllable forces or dynamic ranges in applications in which the fluid is subjected to adverse flow conditions. The implication here towards applications such as impact or shock loading cannot be understated. Active valve lengths should be sufficiently large to ensure that the dynamic range of the device remains constant throughout the range of expected fluid velocities, or more precisely, fluid dwell times. For the two magnetic field strengths considered, 100 kA/m and 200 kA/m, fluid response times were identified as 0.7325 ms and 0.5303 ms, respectively.

Furthermore, from the normalized yield stress analysis, a model was proposed which captures the dependence of yield stress on dwell time. Existing models for MR fluid yield stress are functions of magnetic field strength exclusively. Based on the results presented in this chapter, a modification of the form

$$\tau_o = \Psi_p\left(t_{dwell}, H\right) \cdot \left\{C \cdot 271700 \cdot \Phi^{1.5239} \cdot \tanh\left(6.33 \cdot H\right)\right\} \tag{6-20}$$

is suggested to account for the yield stress dependence on fluid dwell time.

7 Conclusions

This chapter summarizes the work conducted in this study. The primary results are highlighted and suggestions are made for the extension of this work to future studies.

7.1 Research summary

This research studied the high shear and high velocity behavior of MR fluid. Since their introduction, MR fluids and MR fluid devices have provided solutions to many engineering challenges. The great success of MR fluids continues to motivate current and future applications. However, while the behavior of the fluid may be well known under certain operating conditions, current and future applications expose the fluid to, as yet, uncharacterized flow conditions. Such conditions include high shear and high velocity flow. This study identified the behavior of the fluid operating in these adverse flow conditions. Both the off-state and the on-state behavior were evaluated.

The off-state behavior of the fluid was evaluated at shear rates ranging from 0.14×10^5 s^{-1} to 2.5×10^5 s^{-1}. Because MR fluid behavior at high shear is largely governed by the carrier fluid, the carrier fluid was also evaluated at high rates of shear. From the measured force, the shear stress was found and the relationship between shear stress and shear rate was presented for each fluid. Models for the high shear behavior of both the MR fluid and the carrier fluid are developed from the experimental data. Results indicate that MR fluid in the off-state exhibits nearly Newtonian post-yield behavior. A slight thickening is observed for growing shear rates. This slight thickening may be largely due to the carrier fluid behavior. At high shear, the carrier fluid exhibits considerable shear thickening. This thickening may be the cause of the thickening observed in the MR fluid behavior at high shear.

The goal of the on-state investigation was to characterize the MR effect at high flow velocities. Fluid velocities ranged from 1 m/s to 37 m/s. Two active valve lengths were considered, 25.4 mm and 6.35 mm. The term “dwell time” was introduced and defined as the time the fluid spends in the presence of a magnetic field. For the range of velocities considered and the two active valve lengths, corresponding fluid dwell times

ranged from 12 ms to 0.18 ms. Results indicate that fluid dwell time can greatly influence the yield stress developed in the fluid. For dwell times less than 1 ms, the yield stress may only achieve a fraction of the expected value. Furthermore, experimental results imply that the normalized yield stress is a function of both dwell time and magnetic field strength. A model which can describe the yield stress dependence on dwell time and field strength is proposed. The model is well supported by the experimental data.

In conclusion, this study evaluated the high shear and high velocity behavior of MR fluid, both in the off-state and in the on-state. A nearly Newtonian post-yield behavior was identified for the MR fluid in the off-state. Results for the on-state testing indicated a need to consider fluid dwell times in high velocity applications. Active valve lengths should be sufficiently large to ensure that the dynamic range of the device remains constant throughout the range of expected fluid velocities, or more precisely, fluid dwell times.

7.2 Recommendations for future research

Throughout the course of this research, several topics, beyond the scope of the current study, were encountered. In what follows, a brief discussion of such topics is provided.

7.2.1 Non-steady conditions

The current study was conducted under steady-state conditions. In practice, however, fluid flow within a particular device is seldom steady-state. On the contrary, the flow is predominantly transient with many changes in flow direction and flow velocity. As a first step, the current study serves to identify behavior under adverse steady-state conditions. A logical extension would be to include adverse, non-steady conditions. Of course, in developing models for the non-steady flow, the degree of difficulty associated with the solution of the Navier-Stokes equations increases quite considerably. However, various approximations or estimations can be made to simplify the problem. A number of such approximations have been proposed in the literature [51, 56].

Of particular interest when considering non-steady conditions is the formation of the plug within the flow channel. Under non-steady conditions the plug width would

change as a function of time. As an example, we consider a case in which the fluid is accelerating at a constant rate through parallel plates. As the fluid accelerates through the MR valve, exposed to a constant magnetic field strength, the plug width, δ, would decrease for growing velocities, as shown in Figure 7-1. This reduction in plug width would presumably be accompanied by a reduction in shear stress. The rate at which the plug deforms may also be of interest.

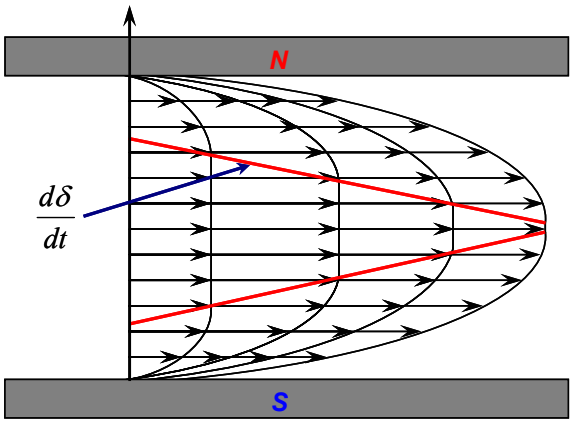

Figure 7-1. Plug decomposition under non-steady flow

The plug formation rate may be studied under a number of conditions. Another form of non-steady flow that may be considered can be caused by fluctuations in the magnetic field strength. The behavior illustrated in Figure 7-1 could also be the result of altering the magnetic field strength. A simple example serves to illustrate the idea proposed here. Consider a case in which the fluid is flowing at a constant velocity and the magnetic field strength is increasing linearly. The plug formation rate would certainly be a function of the rate at which the magnetic field is being increased. The effect of the plug formation rate may be an interesting study.

This concept of plug formation rate or plug decomposition rate can be investigated under a number of conditions. Two such conditions were proposed above. The plug formation rate may have significant effects on device performance and may be considered as an area for future research.

7.2.2 Evaluating different MR fluid compositions

The MR fluid used in this study was MRF-132LD. This particular fluid had an iron content of 32% by volume. Future studies might consider the effect of iron content to identify the effect of iron content on the behavior of the fluid at high velocities and high shear rates; higher iron content may lead to faster response times. A number of fluids are commercially available from Lord Corporation with varying fluid compositions. For high velocity applications, future work might identify which existing fluid is best suited for such applications. Furthermore, a thorough study might identify which fluid properties are responsible for the improved performance at high velocity and high shear. This information may prove valuable in the development of future fluids specifically engineered for high velocity and high shear applications.

7.2.3 Other recommendations

Throughout the course of the current study, several other thoughts and ideas were come upon. These may be developed into avenues for future research and are summarized as follows:

- Identify the dependence on normalized yield stress on magnetic field strength – Future work may include a number of additional experiments performed at various magnetic field strengths. With sufficient data to represent the magnetic field dependence, it will be possible to further develop the proposed model for the normalized yield stress such that it can be expressed explicitly as a function of both dwell time and magnetic field strength.
- Identify a model for the response time of MR fluid as a function of magnetic field strength
- Investigate the dependence of particle size *and* shape on the high velocity and high shear behavior of MR fluid
- Study the effect of the off-state behavior on the high velocity on-state behavior – How does the off-state viscosity effect the on-state behavior of the fluid at high velocity and high shear?

References

1. Rabinow, J., "The magnetic fluid clutch," *AIEE Trans. 67*, p. 1308, 1948.
2. Weiss, K. D., Duclos, T. G., Carlson, J. D., Chrzan, M. J., Margida, A. J., "High strength magneto – and electro – rheological fluids," *Society of Automotive Engineers*, 932451, 1993.
3. Carlson, J. D., Weiss, K. D., "A growing attraction to magnetic fluids," *Machine Design*, Vol. 66, No. 15, p. 61-64, 1994.
4. Lord Corporation, www.lord.com
5. Carlson, J. D., "Multi-degree of freedom magnetorheological devices and system for using same," U.S. Patent 5,492,312 1996.
6. Hong, S. R., Choi, S. B., Jung, W. J., Jeong, W. B., "Vibration isolation of Structural Systems Using Squeeze Mode ER Mounts," *Journal of Intelligent Material Systems and Structures*, Vol. 13, No. 7, p. 421-424, 2002.
7. Carlson, J. D., and Jolly, M. R., "MR fluid, foam and elastomer devices," *Mechatronics*, 10, p. 555-569, 2000.
8. Jolly, M. R., Bender, J. W., and Carlson, J. D., "Properties and applications of commercial magnetorheological fluids," *Journal of Intelligent Material Systems and Structures*, Vol. 10, No. 1, p. 5, 1999.
9. Koo, J. H., "Using magnetorheological dampers in semiactive tuned vibration absorbers to control structural vibrations," Ph.D. Dissertation, Virginia Polytechnic Institute and State University, Blacksburg, VA, 2003.
10. Crosby, M. J., Karnopp, D. C., "The Active Damper," *The Shock and Vibration Bulletin 43*, Naval Research Laboratory, Washington, DC, 1973.
11. Karnopp, D. C., Crosby, M. J., "System for controlling the transmission of energy between spaced members," U.S. Patent 3,807,678 1974.
12. Lee, H. S., and Choi, S. B., "Control and response characteristics of a magnetorheological fluid damper for passenger vehicles," *Journal of Intelligent Material Systems and Structures*, Vol. 11, No. 1, p. 80-87, 2000.
13. Simon, D. E., "An investigation of the effectiveness of skyhook supsensions for controlling roll dynamics of sport utility vehicles using magnetorheological dampers," Ph.D. Dissertation, Virginia Polytechnic Institute and State University, Blacksburg, VA, 2001.
14. Song, X., Ahmadian, M., Southward, S. C., "An Adaptive Semiactive Control Algorithm for Vehicle Suspension Systems," *Proceedings of IMECE*, Washington, D.C., November 16 - 21, 2003.
15. Pund, D., Markus, F., Robinson, A., Webster, L., "The New Cars: Charting the Changes for 2002," *Car & Driver*, Vol. 47, No. 4, p. 62, Oct. 2001.

16. Gehm, R., "Delphi Improves Cadillac's Ride," *Automotive Engineering International*, Vol. 109, No. 10, pp. 32-33, Oct. 2001.
17. Halverson, H., "Magnetic Ride - Star Wars Meets the 50th Car," www.corvetteactioncenter.com, 2003.
18. Lord Rheonetic Magnetically Responsive Technology, MR Damper, RD-1005-3 Product Bulletin, 2003.
19. Carlson, J. D., Catanzarite, D. M., St. Clair, K. A., "Commercial Magneto-Rheological Fluid Devices," *Proceedings 5th International Conference on ER Fluids*, MR Suspensions and Associated Technology, W. Bullough, Ed., World Scientific, Singapore, 1996.
20. Wu, X., and Griffin, M. J., "A Semi-Active Control Policy to Reduce the Occurrence and Severity of End-Stop Impacts in a Suspension Seat with and Electrorheological Fluid Damper," *Journal of Sound and Vibration*, Vol. 203, No. 5, p. 781-793, 1997.
21. Choi, S. B., Nam, M. H., Lee, B. K., "Vibration Control of MR Seat Damper for Commercial Vehicles," *Journal of Intelligent Materials System and Structures*, Vol. 11, No. 12, p. 936-944, 2000.
22. McManus, S. J., St. Clair, K. A., Boileau, P. E., Boutin, J., "Evaluation of Vibration and Shock Attenuation Performance of a suspension Seat with a Semi-Active Magnetorheological Fluid Damper," *Journal of Sound and Vibration*, Vol. 253, No. 1, p. 313-327, 2002.
23. Choi, Y. T., and Wereley, N. M., "Mitigation of Biodynamic Response to Vibratory and Blast-Induced Shock Loads Using Magnetorheological Seat Suspensions," *Proceedings of IMECE*, 43313, Washington, D.C., November, 16-21, 2003.
24. Lord Corporation, "Sears Seating Taps LORD Corporation to Provide Motion Master Seat Suspension Technology for Ag, Off-Highway Vehicles," *Press Release*, September, 2003.
25. Lord Corporation, "School Transportation Officials in Six States Adopt LORD Corporation's Driver Seat System for Bus Safety," *Press Release*, August, 2001.
26. Dyke, S. J., Spencer Jr., B. F., Sain, M. K., Carlson, J. D., "Modeling and Control of Magnetorheological Dampers for Seismic Response Reduction," *Smart Materials and Structures*, Vol. 5, No. 5, p. 565-575, 1996.
27. Dyke, S. J., Spencer Jr., B. F., Sain, M. K., Carlson, J. D., "An Experimental Study of MR Dampers for Seismic Protection," *Smart Materials and Structures*, Vol. 7, No. 5, p. 693-703, 1998.
28. Carlson, J. D., Spencer Jr., B. F., "Magnetorheological Fluid Dampers for Seismic Control," *Proceedings of DETC*, VIB4124, Sacramento, CA, 1997.
29. Yang, G., Spencer Jr., B. F., Carlson, J. D., Sain, M. K., "Large-scale MR Fluid Dampers: Modeling and Dynamic Performance Considerations," *Engineering Structures*, 24, p. 309-323, 2002.

30. Ni, J. M., Ni, Y. Q., Chen, Z. Q., and Spencer Jr., B. F., "Implementation of MR Dampers to Dongting Lake Bridge for Cable Vibration Mitigation," *Proceedings of the 3rd World Conference on Structural Control*, Como, Italy, Vol. 3, p. 777-786, 2002.

31. Ni, Y. Q., Chen, Z. Q., Ko, J. M., and Zheng, G., "Optimal Voltage/Current Input to ER/MR Dampers for Multi-switch Control of Stay Cable Vibration," *Proceedings of the 3rd World Conference on Structural Control*, Como, Italy, Vol. 3, p. 767-775, 2002.

32. Lord Corporation, "LORD Corporation Supplies 320 MR Fluid Dampers for Cable-Stayed Bridge Retrofit to Control Wind Vibration," *Press Release*, March, 2002.

33. Carlson, J. D., "Low-Cost MR Fluid Sponge Devices," *Journal of Intelligent Material Systems and Structures*, Vol. 10, p.589-594, August, 1999.

34. Biedermann Motech GmbH, www.biedermann.com

35. Carlson, J. D., Matthis, W., Toscano, J. R., "Smart Prosthetics Based on Magnetorheological Fluids," *Proceedings of SPIE*, Vol. 4332, p. 308-316, 2001.

36. Lord Rheonetic Magnetically Responsive Technology, MR Brake MRB-2107-3, *Product Bulletin*, 2003.

37. QED Technologies, www.qedmrf.com

38. Kordonski, W. I., and Golini, D., "Fundamentals of Magnetorheological Fluid Utilization in High Precision Finishing," *Journal of Intelligent Material Systems and Structures*, Vol. 10, p. 683-689, September, 1999.

39. Menapace, J. A., Dixit, S. N., Genin, F. Y., Brocious, W. F., "Magnetorheological Finishing for Imprinting Continuous Phase Plate Structure onto Optical Surfaces," UCRL-CONF-153850, Boulder Damage Sysmposium XXXV, Boulder, CO, September 21-24, 2003.

40. Ahmadian, M., Poynor, J. C., Gooch, J. M., "Application of Magneto Rheological Dampers for Controlling Shock Loading," *Proceedings of ASME Dynamic Systems and Control*, DSC-Vol. 67, p. 731-735, 1999.

41. Messina, N., "Multi-Role Armament & Ammunition System ATD-GDAS Program Scope and Approach," *Proceedings of 36th Annual Gun & Ammunition Symposium & Exhibition*, www.dtic.mil/ndia, presentation, April 9-12, 2004.

42. Chen, P. C., Wereley, N., "Magnetorheological Damper and Energy Dissipation Method," U.S. Patent 6,694,856 B1 2004.

43. Facey, W. B., Rosenfeld, N. C., Choi, Y. T., Wereley, N. M., "Design and Testing of a Compact Magnetorheological Damper for High Impulsive Loads," *Proceedings of the 9th International Conference on Electrorheological Fluids and Magnetorheological Suspensions*, Beijing, China, August 29 – September 3, 2004.

44. El Wahed, A. K., Sproston, J. L., Schleyer, G. K., "Electrorheological and Magnetorheological Fluids in Blast Resistant Design Applications," *Materials and Design*, 23, p. 391-404, 2002.

45. El Wahed, A. K., Sproston, J. L., Schleyer, G. K., "A Comparison Between Electrorheological and Magnetorheological Fluids Subjected to Impulsive Loads," *Proceedings of the 7th International Conference on Electrorheological Fluids and Magnetorheological Suspensions*, Honolulu, Hawaii, p. 401-410, 1998.

46. Norris, J. A., "Behavior of Magnetorheological Fluids Subject to Impact and Shock Loading," M.S. Thesis, Virginia Polytechnic Institute and State University, Blacksburg, VA, 2003.

47. Browne, A. L., McCleary, J. D., Namuduri, C. S., Webb, S. R., "Impact Performance of Magnetorheological Fluids," *Proceedings of IMECE*, 60542, Anaheim, CA, November, 13-20, 2004.

48. Choi, Y. T., Wereley, N. M., "Vibration Control of a Landing Gear System Featuring Electrorheological/Magnetorheological Fluids," *Journal of Aircraft*, Vol. 40, No. 3, p. 432-439, 2003.

49. Carlson, J. D., "What Makes a Good MR Fluid?," *Journal of Intelligent Material Systems and Structures*, Vol. 13, No. 7, p. 431-435, 2002.

50. Lord Corporation, "Army Looks at Improving Vehicles' Performance with MR Fluid Technology from LORD Corporation," *Press Release*, July, 2004.

51. Phillips, R. W., "Engineering Applications of Fluids with a Variable Yield Stress," Ph.D. Dissertation, University of California, Berkeley, CA, 1969.

52. Yang, G., "Large-Scale Magnetorheological Fluid Damper for Vibration Mitigation: Modeling, Testing and Control," Ph.D. Dissertation, University of Notre Dame, Notre Dame, IN, 2001.

53. Kamath, G. M., Hurt, M. K., Wereley, N. M., "Analysis and Testing of Bingham Plastic Behavior in Semi-Active Electrorheological Fluid Dampers," *Smart Materials and Structures*, Vol. 5, p. 576-590, 1996.

54. Wereley, N. M., Pang, L., "Nondimensional Analysis of Semi-Active Electrorheological and Magnetorheological Dampers Using Approximate Parallel Plate Models," *Smart Materials and Structures*, Vol. 7, p. 732-743, 1998.

55. Constantinescu, V. N., Laminar Viscous Flow, Springer, New York, 1995.

56. Gavin, H. P., "Electrorheological Dampers for Structural Vibration Suppression," Ph.D. Dissertation, University of Michigan, Ann Arbor, MI, 1994.

57. Beyer, W. H., CRC Handbook of Mathematical Sciences, 6th Edition, CRC Press, Boca Raton, FL, 1987.

58. Jolly, M. R., Carlson, J. D., Munoz, B. C., "A Model of the Behavior of Magnetorheological Materials," *Smart Materials and Structures*, Vol. 5, p. 607-614, 1996.

59. Lord Rheonetic Magnetically Responsive Technology, Hydrocarbon-Based MR Fluid MRF-132LD, *Product Bulletin*, 2002.

60. Carlson, J. D., "MR Technology Workshop – Chapter 6," Lord Corporation, Cary, NC, p. 6/9-6/10, 2004.

61. 1989 ASHRAE Handbook – Fundamentals.

62. Baird, D. G., and Collias, D. I., Polymer Processing Principles and Design, Wiley Interscience, New York, NY, 1998.

63. Van Wazer, J. R., Lyons, J. W., Kim, K. Y., Colwell, R. E., Viscosity and Flow Measurement A Laboratory Handbook of Rheology, Wiley Interscience, New York, NY, 1963.

64. Lord Materials Division, "Magnetic Circuit Design," Engineering Note, 1999.

65. Carlson, J. D., "Magnetorheological Fluid Seismic Damper," U.S. Patent, 6,296,088 B1 2001.

66. BASF, The Chemical Company, www.BASF.de.

67. Material Safety Data Sheet (MSDS #3332), Synfluid ® 4 cSt PAO, Chevron Phillips Chemical Company LP, The Woodlands, TX, Rev. 19, Rev. Date 10/07/2004.

68. Carlson, J. D., Private communication, 2004.

69. Incropera, F. P., DeWitt, D. P., Introduction to Heat Transfer, John Wiley & Sons, New York, 1990.

70. Lord Materials Division, "MR Valve Configurations," Engineering Note, 2001.

71. Carlson, J. D., Chrzan, M. J., "Magnetorheological Fluid Dampers," U.S. Patent, 5,277,281 1994.

72. Carlson, J. D., Chrzan, M. J., James, F. O., "Magnetorheological Fluid Devices," U.S. Patent, 5,398,917 1995.

73. Poynor, J. C., "Innovative Designs for Magnetorheological Dampers," M.S. Thesis, Virginia Polytechnic Institute and State University, Blacksburg, VA, 2001.

74. Bullough, W. A., Peel, D. J., Spronston, J. L., Stanway, R., Rodgers, D. L., "An ER Long-Stroke Damper for Vehicle Suspension Applications," FED-Vol. 205/AMD-Vol. 190, p. 41, *Proceedings of IMECE*, Chicago, Illinois, November 6-11, 1994.

75. Ginder, J. M., "Rheology Controlled by Magnetic Fields," *Encyclopedia of Applied Physics*, Vol. 16, p. 487-503, 1996.

Vita

Fernando D. Goncalves was born on August 28th, 1977 in Floral Park, New York. He grew up in nearby Farmingville, New York, where his parents still live today. Fernando graduated in 1995 from Sachem High School in Lake Ronkonkoma, New York. From there, he went on to pursue a degree in Engineering from Roger Williams University in Bristol, Rhode Island. In 1999, he earned his Bachelor's degree in Engineering, graduating Cum Laude and first in the School of Engineering. After graduating, Fernando headed south to pursue a M.S. degree in Mechanical Engineering from Virginia Tech in Blacksburg, Virginia. Studying in the Advanced Vehicle Dynamics Laboratory, Fernando's M.S. work focused on semi-active vehicle suspensions. Earning his M.S. degree in August of 2001, Fernando remained at Virginia Tech to begin Ph.D. studies. His Ph.D. work focused on the high velocity flow of magnetorheological fluids. Fernando earned his Ph.D. in May 2005 and has accepted a position at Lord Corporation in Cary, North Carolina. Fernando will be married in September 2005 to his fiancée Courtney Mulligan.